Final Technical Report

Diode Laser Sensors for Arc-Jet Characterization

NASA-Ames University Consortium Grant NCC 2-5522

Prepared for NASA Ames Research Center

For the Period
September 1, 2002 to August 31, 2005

September 2005

Professor Ronald K. Hanson, PI
High Temperature Gasdynamics Laboratory
Department of Mechanical Engineering
Stanford University
Stanford, CA 94305-3032

hanson@me.stanford.edu

Mechanical Engineering Department
Stanford University
Stanford, California 94305

Executive Summary

The development and application of tunable diode laser (TDL) absorption sensors to monitor the health and operating conditions in the large-scale 60 MW arc-heated-plasma wind-tunnel at NASA Ames Research Center is reported. The interactive heating facility (IHF) produces re-entry flow conditions by expanding the gas heated in a constricted plasma arc-heater to flow at high velocity over a model located in a test cabin. This facility provides the conditions needed to test thermal protective systems for spacecraft re-entering the earth's atmosphere. TDL sensors are developed to monitor gas flows in both the high-temperature constricted flow and the supersonic expansion flow into test cabin. These sensors utilize wavelength-tuned diode lasers to measure absorption transitions of atomic oxygen near 777.2 nm, atomic nitrogen near 856.8 nm, and atomic copper near 793.3 nm. The oxygen and nitrogen sensors measure the population density in exited electronic states of these atoms. The measurements combined with the assumption of local thermal and chemical equilibrium yield gas temperature (typically near 7,000K). The nitrogen and oxygen population temperatures are redundant, and their close agreement provides an important test of the local thermal equilibrium assumption. These temperature sensors provide time-resolved monitors of the operating conditions of the arc-heater and can be used to verify and control the test conditions. An additional TDL sensor was developed to monitor the copper concentration in the arc-heater flow yielding values as high as 13 ppm. Measurements of copper in the flow can identify flow conditions with unacceptably rapid electrode erosion, and hence this sensor provides valuable information needed to schedule maintenance to avoid costly arc-heater failure. TDL sensors were also developed for measurements in the test cabin, where absorption measurements of the populations of argon and molecular nitrogen in excited metastable electronic states established that the number density of these excited species is much lower than estimated using frozen-chemistry approximations. This key finding suggests that in the post-expansion region there is not a significant energy sequestration in electronically excited species. Finally, TDL measurements of atomic potassium seeded into the test cabin flow were used to directly measure the static temperature of the test gas.

The results of this study illustrate the high potential of time-resolved TDL measurements for routine and economical sensing of arc-heater health (gas temperature and electrode erosion) as well as the time-resolved test-cabin-flow conditions in front of the model.

Contents

Introduction and Motivation

New thermal protection system (TPS) materials for NASA missions are developed on the basis of testing in the large-scale, high-enthalpy, arcjet test facilities at NASA-Ames Research Center. Hypersonic speeds of reentry vehicles and systems produce a hot, reactive gas layer between the bow shock and the vehicle surface. A vehicle moving at 10 km/sec in the cold air of the mesosphere (~270K, ~0.1kPa) produces shock temperatures near 7000K with surface heating rates of hundreds of watts per square centimeter. Arcjet facilities provide a long-duration (tens of minutes) source of high-enthalpy hypersonic air flow for ground test of these materials. The NASA-Ames Research Center has three arcjet facilities devoted to testing TPS.[1] Understanding the performance is crucial to the determination of TPS safety margins needed for reliable flight vehicles.

Currently, arc-jet test conditions are defined using either the expected heat-flux level or the anticipated surface temperature for a particular material in its envisioned application. While this is sufficient to evaluate relative performance levels, it is not sufficient for establishing absolute capability for materials or for integrated TPS. This lack of traceability of the TPS test environment to the actual vehicle performance environment significantly increases the required safety margin in TPS tests and thus performance uncertainty. Evaluation of absolute aero-thermal performance requires understanding the energy partition of the gas stream from the arc-jet facility and the temporal fluctuations of this energy partition. Although arc-jets have been used for the past 40 years to simulate aero-thermal test environments, the non-equilibrium nature of the gas stream has proven difficult to characterize. Although a wide variety of experiments have led to considerable progress in unraveling the composition of the gas stream, there remains significant uncertainty especially for the highest enthalpy tests. This uncertainty arises from the unknown composition of the gas stream as it freezes during the non-equilibrium expansion of the arc-heated gas. Gas (typically air/argon mixtures at NASA Ames) is heated in an electric arc and expanded in a high-compression ratio supersonic nozzle into an evacuated test chamber. A significant fraction of the gas is dissociated to atoms in the arc heater and their recombination to molecules is arrested in the nozzle, effectively "freezing" the gas composition. This can trap a significant number of species in meta-stable excited electronic states.

An arcjet uses a high power electrical discharge to heat a stream of air (with added argon for electrode cooling), and this gas mixture is accelerated to hypersonic velocities in an adiabatic expansion. A schematic of the NASA-Ames arcjet flow facility is shown in Fig. 1.[2] A high-current arc heats the input high-pressure gas stream to temperatures in excess of 6000 K. The equilibrium dissociation fraction of both oxygen and nitrogen is substantial. This hot, high-enthalpy gas is accelerated via adiabatic expansion and directed over a stationary model, simulating the high speed passage of a space vehicle through an atmosphere.[3]

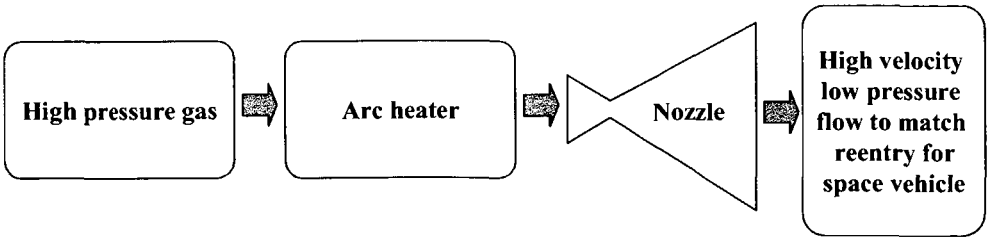

Figure 1. Block diagram of the arcjet wind tunnel facility.

The choice of arc-heater test conditions to simulate specific flight environments requires knowledge of the thermodynamic state of the gas prior to expansion. Because of the extreme conditions inside the arc-heater section, options for measurements of the test gases are limited, and optical spectroscopy-based measurements of air-derived species present a diagnostic opportunity. In addition, component materials in the arc-heater and nozzle may erode and contribute non-air species to the flowfield. One consequence of this erosion is periodic (and costly) failure of arcjet components, and measuring eroded materials may provide a useful indicator of component health and maintenance requirements.

In this project, we design and demonstrate tunable-diode-laser (TDL) absorption sensors for time-resolved monitoring of gas temperature in the arc-heater, copper produced by erosion in the arc-heater, and static temperature of the test gas in front of the model in the test cabin. TDLs provide convenient optical sources for absorption measurements [4], and recent development of fiber optics technology makes measurements within the electrically isolated arc-heater feasible. TDL sensors of dissociated air species can be used to monitor the high temperatures expected in the arc-heater. In our laboratory at Stanford University, Baer et al. [5,6] used TDL sensors to measure temperature and number density of argon in high-temperature RF-plasma discharges. Baer et al. [7] also used a TDL sensor near 777.2 nm to monitor atomic oxygen and infer gas temperature in air RF-plasmas. Here we use TDLs near 777.2 and 844.6 nm to monitor atomic oxygen and near 856.8 and 824.2 nm to monitor atomic nitrogen, in the plenum immediately downstream of the high temperature dc-arc discharge. An additional TDL sensor was also developed to monitor atomic copper near 793.3 nm in the flowfield. Measurements of copper in the flow can identify flow conditions with unacceptably rapid electrode erosion, and this sensor provides information needed to schedule maintenance to avoid costly arc-heater failure. The copper sensor identified plasma operating conditions where atomic copper concentrations as high as 13 ppm were observed. These results demonstrate that TDLs diagnostics have the potential to provide routine *in situ* monitoring of the gas conditions in the arc-heater.

TDL sensors were also developed for measurements in the test cabin. Those absorption measurements yielded values for the population in metastable electronic states of argon and molecular nitrogen, providing evidence that the number density of these excited species is much lower than estimated using a frozen-chemistry approximation. This suggests that in the post-expansion region there is not a significant energy sequestration in electronically excited species. In addition, TDL measurements of atomic

potassium seeded into the test cabin flow were used to directly measure the static temperature of the test gas.

The IHF arc-jet driven wind tunnel is a large-scale engineering facility. The physical size of the device and the magnitude of the electrical power dissipated in the arc-heater provide significant engineering challenges to the implementation of *in situ* gas sensing. Fiber optics was used successfully to transport the laser light to and from the arc-heater, while providing the required electrical isolation. We regard the associated optical engineering of the two TDL sensor systems to be an important part of the overall effort.

Detailed Research Results

Details of the research performed to develop and test TDL sensors in the IHF 60 MW plasma-driven wind tunnel at NASA Ames Research center are provided in the PhD thesis of Suhong Kim and published by the American Institute of Aeronautics and Astronautics. This thesis: "Development of Tunable Diode Laser Absorption Sensors For A Large-Scale Arc-Heated-Plasma Wind Tunnel" is available on the web at (http://navier.stanford.edu/thermosciences/TSD-155.pdf) and included here as Appendix I. The paper AIAA 0225-0900, "Gas Temperature in the Arc-heater of a Large Scale Arcjet Facility using Tunable Diode Laser Absorption," is available from the AIAA and is included as Appendix II. Therefore these details will not be repeated here.

Publications

Suhong Kim, "Development of Tunable Diode Laser Absorption Sensors For A Large-Scale Arc-Heated-Plasma Wind Tunnel" Stanford University PhD Thesis, (http://navier.stanford.edu/thermosciences/TSD-155.pdf) (Appendix I)

Suhong Kim, Jay B. Jeffries, Ronald K. Hanson, George A. Raiche, "Gas Temperature in the Arc-heater of a Large Scale Arcjet Facility using Tunable Diode Laser Absorption," *43rd Aerospace Sciences Meeting*, AIAA. 2005-900, 2005. (Appendix II)

References

1. R.K. Smith, D.A. Wagner, and J. Cunningham, "A Survey of Current and Future Plasma Arc-Heated for Aerospace and Commercial Applications," American Institute of Aeronautics and Astronautics, AIAA-1998-0146, (1998).
2. A. Balter-Peterson, F. Nichols, B. Mifsud, and W. Love, "Arcjet Testing in the NASA Ames Research Center Thermophysics Facilities," American Institute of Aeronautics and Astronautics, AIAA-1992-1071, (1992).
3. C.S. Park, D.G. Fletcher, and J.M. Donahue, "Spatially Resolved Shock Layer Emission Measurements and Analysis in an Arcjet Facility," American Institute of Aeronautics and Astronautics, AIAA-1999-1046, (1999).
4. M.G. Allen, "Diode Laser Absorption Sensors for Gas-Dynamic and Combustion Flows," Measurement Science and Technology, 9, 545-562 (1998).
5. D.S. Baer, H.A. Chung, and R.K. Hanson, "Tunable Diode Laser Diagnostics for Atmospheric Pressure Plasmas," J. Quantitative Spectros. Radiat. Trans. 47, 455-475 (1992).

6. D.S Baer and R.K. Hanson, "Fluorescence Diagnostics for Atmospheric-Pressure Plasmas using Tunable Diode Lasers," J. Opt. Soc. Am. B, 9, 1968-1978 (1992).
7. D.S. Baer, H.A. Chung, and R.K. Hanson, "Semiconductor Laser Absorption Diagnostics of Atomic Oxygen in an Atmospheric-Pressure Plasma," J. Quant. Spectrosc. Radiat. Trans., 50, 621-633 (1993).

DEVELOPMENT OF TUNABLE DIODE LASER ABSORPTION SENSORS FOR A LARGE-SCALE ARC-HEATED-PLASMA WIND TUNNEL

A DISSERTATION
SUBMITTED TO THE DEPARTMENT OF MECHANICAL ENGINEERING
AND THE COMMITTEE ON GRADUATE STUDIES
OF STANFORD UNIVERSITY
IN PARTIAL FULFILLMENT OF THE REQUIREMENTS
FOR THE DEGREE OF
DOCTOR OF PHILOSOPHY

Suhong Kim
June 2 2004

I certify that I have read this dissertation and that, in my opinion, it is fully adequate in scope and quality as a dissertation for the degree of Doctor of Philosophy.

Ronald K.Hanson
(Principal Advisor)

I certify that I have read this dissertation and that, in my opinion, it is fully adequate in scope and quality as a dissertation for the degree of Doctor of Philosophy.

Jay B.Jeffries

I certify that I have read this dissertation and that, in my opinion, it is fully adequate in scope and quality as a dissertation for the degree of Doctor of Philosophy.

Mark A.Cappelli

Approved for the University Committee on Graduate Studies.

Abstract

Arc heated wind tunnels are the most reliable high temperature facilities to test thermal protection systems and heat shields. At NASA Ames Research Center, a 60 MW rated interactive heating facility (IHF) with a constricted arc heater and a expansion test cabin has been used to develop thermal protection systems for space vehicles. The work presented here involves the development and application of tunable diode laser absorption sensors to a large-scale arc-heated-plasma wind tunnel. Two different flow regions are studied: the arc-heater and the test cabin. For the heater, vertical cavity surface emitting lasers (VCSELs) are tuned across individual transitions of atomic oxygen near 777.2 nm and atomic nitrogen near 856.8 nm enabling measurement of atomic concentration and temperature. Due to hyperfine structure and Zeeman splitting, it is not feasible to infer the translational temperature in the heater from the Doppler-broadened linewidth. The population of an excited state and the assumption of local thermal equilibrium are used to determine the population temperature. Simultaneously the copper concentration is monitored with a transition near 793.3 nm, and therefore the rate of electrode erosion is inferred. In the heater, the gas temperature was measured to be near 7,000 K. For high flow conditions, the measured copper concentration ranged up to 13 ppm. In the test cabin, metastable states of argon and atomic oxygen are monitored with VCSELs near 772.4 and 777.2 nm, and the upper limit of these metastable states is determined. Also a translational temperature of 900 K is extracted from the lineshape analysis of a transition near 769.9 nm of atomic potassium seeded upstream. The number density of metastable states is much lower than estimated using a frozen chemistry approximation. This suggests that in the post-expansion region, most atomic species are in the ground state.

Acknowledgements

The work reported here was generously supported by NASA Ames Research Center. George Raiche of NASA guided, encouraged, and supported my research in all aspects. Dave Driver of NASA shared his experience in the arcjet facilities and gave advice on my experimental setup. Joe Olejniczak of NASA kindly discussed and helped me to understand the arcjet flow conditions with his numerical simulations. Also, Jay Grinstead gave critical advice regarding my experimental setup.

Special thanks are due to the NASA Ames Arcjet Team: Vince Meglio, Daniel Theroux, Frank Hui, Cesar Acosta, Scott Eddlemon, and Imelda Terraces-Salinas. They operate the Interactive Heating Facility and control the test procedure. Without their help, this work would not have been possible.

Contents

List of Tables

List of Figures

Chapter 1

Introduction

Thermal protection materials are required to prevent damage to space vehicles during high speed reentry into the earth's atmosphere. Arcjet facilities provide a source of hypersonic air flow for ground test of these materials. This thesis describes the development of tunable diode laser absorption diagnostics to monitor arcjet operations.

Since the late 1950s, thermal protection materials have been developed for the heat shields of reentry vehicles and launch systems. The hypersonic speeds of these vehicles produce a bow shock and a plasma layer between a shock and the vehicle. Collision of a vehicle moving at 10 km/sec with cold air in the mesosphere (roughly 270 K, 0.1 kPa) produces a plasma layer with temperature near 7,000 K.

Different vehicle trajectories and different gas compositions subject the vehicle to different flow environments. For example, as shown in Fig.1.1, the space shuttle trajectory is different from that of ballistic missiles, and therefore has a different maximum loading condition. Also a vehicle entering another planet experiences an atmosphere with quite different temperature, pressure, and potential chemical reactions. Special facilities are required to simulate the hypersonic, low temperature, and low pressure air flow to which space shuttles or long-range ballistic missiles are exposed. Currently only electric arc-heated wind tunnels can provide the high enthalpy flow to simulate the extreme conditions of the reentry of hypersonic vehicles. Hence, ground-based test facilities employing arc-heaters have been developed to test thermal protection materials.

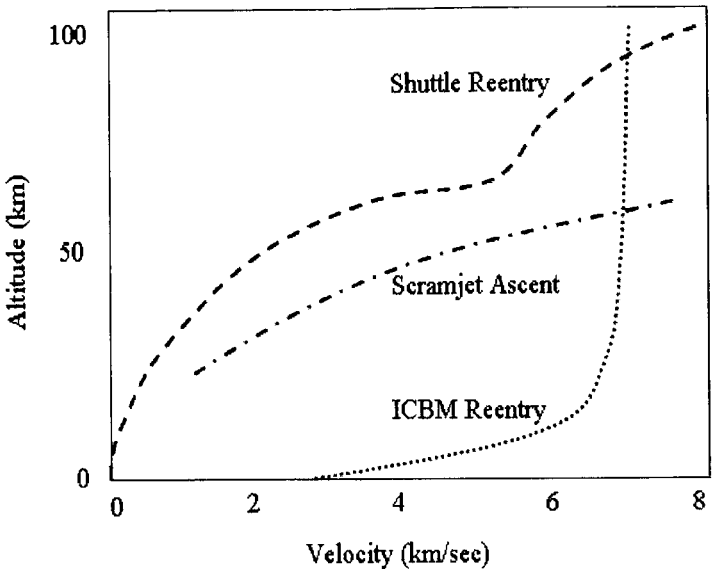

Figure 1.1: Altitude-velocity map of a space shuttle, a scramjet, and a ballistic missile

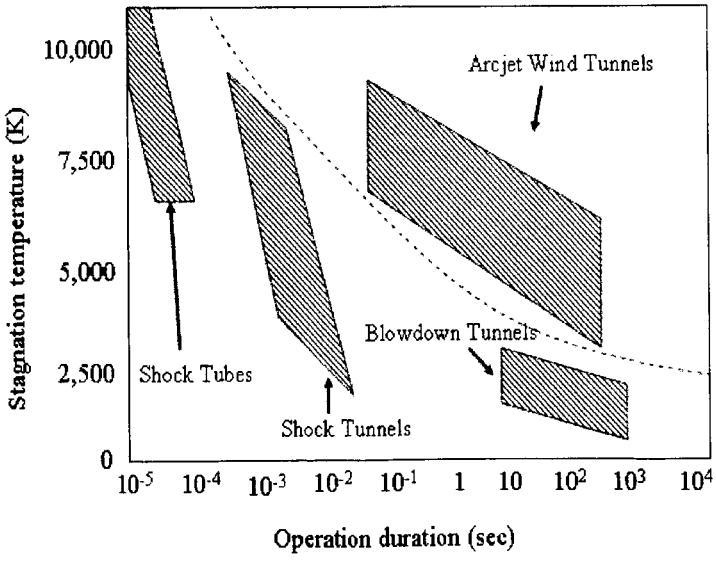

Figure 1.2: Operation range of high-temperature facilities

NASA Ames Research Center has been active in simulating the high-velocity portion of the shuttle trajectory. There is an extensive arcjet testing complex at NASA Ames with three active test facilities. All produce the high enthalpy flow necessary for thermal protection material testing with different power ratings or flow conditions. Samples of the material are immersed in the high enthalpy flow and heated with a high heat flux to simulate the local flight environment. The space shuttle is exposed to the maximum load of temperature up to 7,000 K (behind the bow shock). At such high temperatures, air is excited, dissociated, and ionized. To match this condition, plasma flows of typically 10 km/s at 1,000 K and 6.1 kPa, are generated in an arcjet wind tunnel at NASA Ames Research Center.

1.1 Arcjet wind tunnels

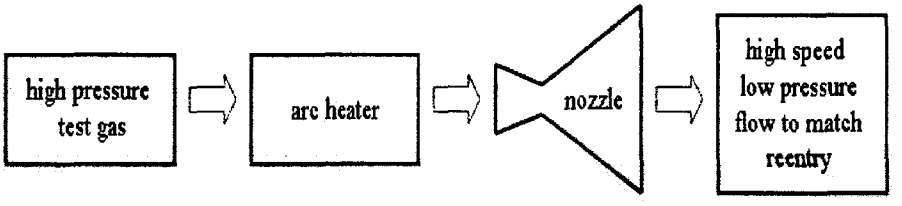

Figure 1.3: Schematics of arc heated wind tunnel with key components

The flow chart in Fig.1.3 depicts the basic operation of the arcjet wind tunnels. The high-pressure test gas is heated by an arc heater. Electric power heats the test gas to obtain the designed enthalpy for the simulation. The pressure is a few atmospheres and the temperature is several thousand degrees in the heater. The converging-diverging nozzle expands high-pressure, high-temperature gas into a low-pressure, low-temperature, hypersonic flow. In the test cabin, the test material is exposed to the hypersonic flow.

The pressure and temperature conditions in the heater walls need to be monitored. Pressure transducers on the heater wall can follow the static pressure of the flow, because the pressure difference across the boundary layer is negligible. However, the

temperature is quite different across the thermal boundary layer, and no continuous diagnostics for the gas temperature have been available. Here, new diagnostics are reported to provide real-time measurements using tunable diode lasers to perform atomic absorption spectroscopy. The amount of absorption of an atomic species provides a concentration which can be related to the temperature with an equilibrium assumption and a measured pressure. Independently using the absorption lineshape, a temperature related to thermal motion can also be extracted.

The flow conditions in the test cabin can also be monitored; however, currently, only calorimeters are used. Here tunable diode laser absorption spectroscopy is demonstrated to provide a continuous monitor of gas temperature and state-specific number density of metastable states in the test cabin.

The following sections describe the arcjet facility in detail and the specific plasma diagnostics performed at the NASA Ames Research Center.

1.2 Arcjet facilities for thermal protection system

There are multiple types of plasma-arc-heated test facilities including multi-segment, Huels or vortex-stabilized, magnetically-stabilized, induction-coupled, and magneto-plasma-dynamic heaters. The review of Smith et al [1] concludes that among various plasma generators, multi-segment heaters are the best choice for thermal protection system acceptance and certification tests, and this is type of facility used at NASA Ames.

Segmented heaters can be operated over a broad range of conditions: e.g., enthalpy between 10 - 45 MJ/kg, with a range of pressure between 1 and 100 bar. Test streams are very stable and test conditions are repeatable. The contamination level is relatively low, although induction-coupled and magneto-plasma-dynamic devices can be cleaner.

The multi-segment arc heater was first developed at the NASA Ames Research Center. This type of arc heater has been utilized for acceptance and certification testing for all US manned space vehicles including the Space Shuttle Orbiter, Apollo,

and Gemini. These facilities are also heavily used to develop thermal protection systems for spacecraft capsules for several planetary entry and return missions including Galileo, Viking and Mars unmanned spacecrafts.

High-power arcjet wind tunnels have a relatively large uncertainty in flow properties: e.g., the free stream conditions and enthalpy of the flow, as well as uncertainty in the procedures to determine flow variables at the surface of the test model. The ground-test facility generating conditions are also different from the aviation conditions. The vehicle moves at hypersonic speed, through static, cold, and low-pressure air (N_2 and O_2). Ideally, the ground test facilities would provide hypersonic, cold, and low-pressure air to the static model; however, currently there are no such ideal test facilities. Instead most advanced arcjet facilities, using multi-segmented arc heaters, provide a hotter, non-equilibrium, and less-uniform mixture of N, O, N_2, O_2, NO, e, etc. Only the heat flux to the model, and the impact pressure are matched to those expected during the flight. Because of the uncertainty between the actual flight conditions and arcjet flow properties, heat shields are designed with a large safety margin, which adds extra weight and reduces vehicle performance [2].

Understanding the arcjet flow stream via non-intrusive diagnostics is vital to reduce this margin for the development of new thermal protection materials. Measurements of flow conditions can verify how close the test conditions are to the expected conditions of a spacecraft reentry. Therefore development and understanding of real-time diagnostics are key to future improvements in spacecraft performance.

1.3 NASA Ames Arcjet Complex: IHF

The 60 MW Interactive Heating Facility (IHF) gives the most flexible performance among all Ames arcjet facilities; the various configurations were reviewed by Balter-Peterson [3]. This facility can provide a fully immersed stagnation point environment with a conical nozzle or a panel test environment with a semi-elliptic nozzle. Its capability to simulate shuttle entry conditions make the testing of scaled thermal protection system components a major task of the IHF.

Arcjet facilities are complex and the IHF has many major subsystems including a multi-segment arc heater, test cabin, power supplies, cooling water system, high-pressure air system, steam vacuum system, and data acquisition system. A photograph of the Ames arcjet complex is given in Fig.1.4. The reader is referred to Balter-Peterson's paper [3] for additional details of arcjet support systems.

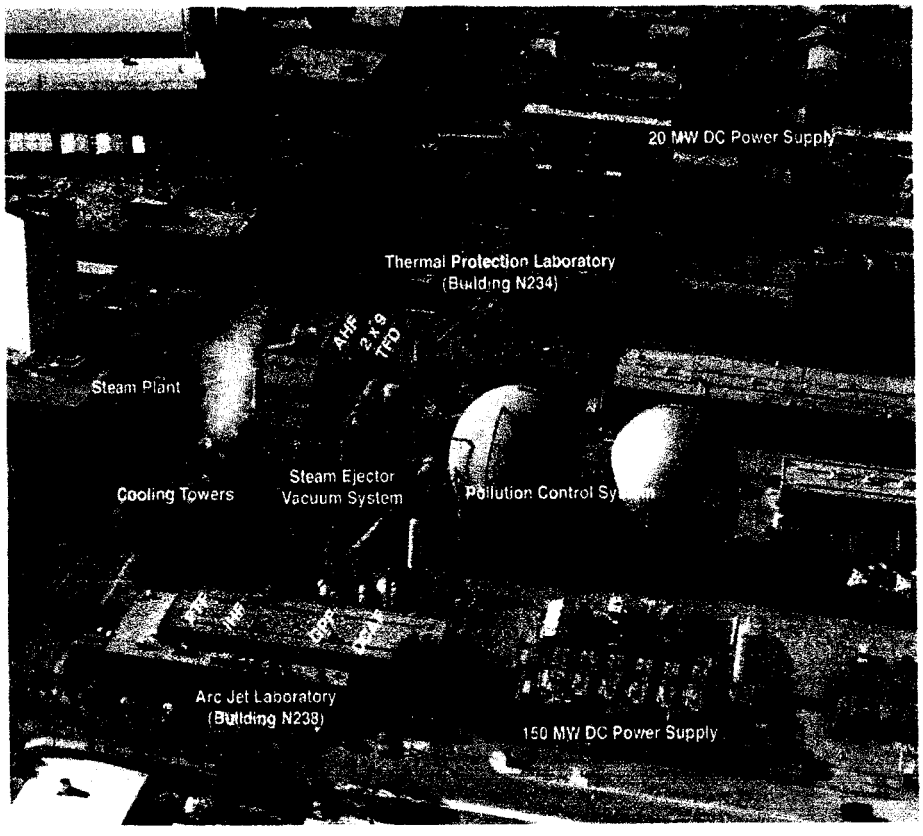

Figure 1.4: Picture of NASA Ames Arcjet facilities

In this thesis, the arc heater and the test cabin are the most important components, and their schematics are shown in Fig.1.5.

Multi-segment arc heater

The multi-segment arc heaters or constricted arc heaters consist of two electrode packages, which contain- multiple stacked disks, each disk being an individual electrode.

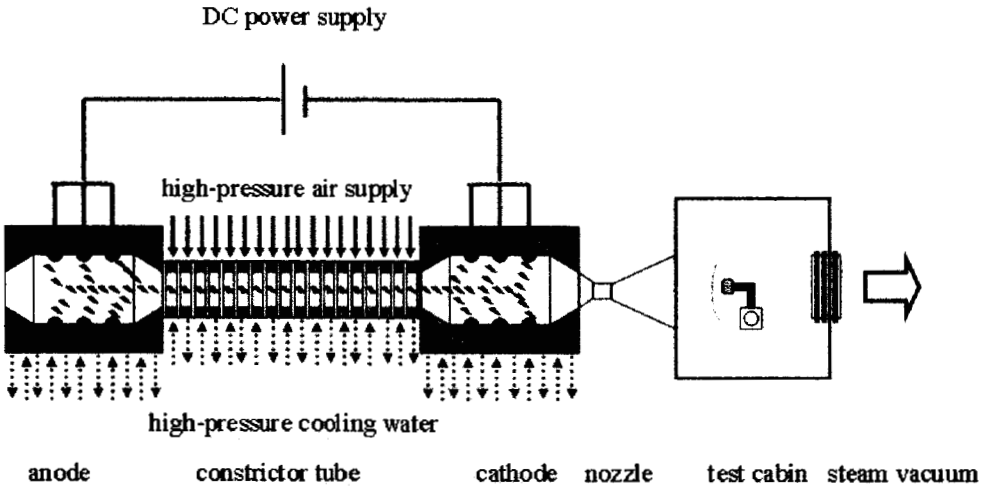

Figure 1.5: Schematics of the IHF heater and the test cabin

The anode is located upstream, the cathode is located downstream, and the ring segments with test gas inlet are fixed between two electrodes. Each active electrode in a electrode package is isolated from the others and has an individual ballast load. Since each electrode has a specific current rating, electrodes are added to a stack until the number of electrode disks is sufficient to handle the total current desired. The current is evenly distributed among the electrodes, and the arc attachment in a multi-segment arc heater produces a smaller thermal load on the electrode surface than other types of heaters such as Huels arc heaters. And in order to reduce electrode erosion, a magnetic field is induced by the current in the heater and used to spin the arc attachment on the electrode. This uniform energy load over electrodes and induced magnetic field reduces the electrode material contamination of the constricted arc heater flow. The arc length is fixed by the length of the constrictor column. The 60 MW IHF constrictor tube has a bore diameter of 7.62 cm (3″), and the slightly expanded water-cooled electrodes are 11.4 cm (4.5″) in diameter.

Test gas

The test gas is a mixture of air and argon with the air between 75 and 90 % of total mass flow. To assure easy start of arc and sufficient ionization in the vicinity of the electrodes, argon gas is used to sheath each electrode disk. Argon also helps to inhibit the formation of oxides on the electrode surface.

Nozzles

There are two types of nozzles used in IHF: asymmetric semi-elliptic nozzles and axisymmetric conical nozzles. With semi-elliptic nozzles, wedge type articles are tested, and with conical nozzles, stagnation point type articles are tested. Developed for space shuttle heat shield tile research, the asymmetric semi-elliptic nozzles are used to test large flat surfaces in high temperature boundary layer flows. The semi-elliptic nozzle is 81.3 cm (32″) wide and the ratio of nozzle width to height is 4:1. The semi-elliptic nozzles have a 6 degree expansion angle, but have an asymmetric cross section that is one half of an ellipse, with the lower surface of the nozzle serving as the major axis of the elliptical section.

A variety of axisymmetric conical nozzles in the test facilities are used in the arcjet complex. Only one throat of 6.03 cm (2.375″) is used but several exit diameters can be installed: 15.2, 39.0, 53.3, 76.2, and 104.1 cm (6, 16, 21, 30, and 41″). Due to flexible area ratios, and easy design and manufacturing, conically shaped nozzles are more widely used.

Arcjet Support Systems

The arcjet facility requires power supplies, a deionized cooling water system, a high pressure air system, and a steam vacuum system. A 20 MW DC power supply, and a 120 MW DC power supply maintain up to 7,500 A at 2,500 V and 16,200 A at 5,500 V respectively. Deionized water is used for cooling of the arc heaters, model supporters, nozzles, etc. The high pressure air system has a compressor and storage systems with a distribution network to provide primary test gas to the heater. The steam vacuum system exhausts a high mass (0.23 kg/sec or 0.5 lb/sec) flow with a

pressure near 7.9×10^{-7} atm or 0.6 mTorr during arcjet operation.

DC electric discharge and gas conditions

The gas is heated by the DC-arc in the constrictor tube before it is expanded into the test cabin. A high DC voltage between two electrodes is applied, and in the constrictor tube between the electrodes, the conductivity of the test gas and small amount of argon makes the electric field roughly 20 V/cm - 30 V/cm. Electrons and ions are accelerated in the applied electric field, and collisions with heavy neutral particles decelerate electrons and ions, heating the gas. At high pressures, there are sufficient collisions for the electrons, ions, and neutral particles to reach equilibrium. In the arcjet heater, the temperature range is 6,000 K - 8,000 K, and the pressure range is 2 atm - 8 atm during normal operation.

Test cabin flow conditions

High pressure fluid in the arc heater expands through converging-diverging nozzle. As the hot gas expands through the converging-diverging nozzle to the test cabin, the flow accelerates to 5 - 10 km/s, the pressure drops to 0.001 atm - 0.01 atm, and the translational temperature drops to a value in the range 500 K - 1,500 K. The test cabin condition is matched to the conditions expected for reentry. Typically, the IHF runs with a mach number between 5 and 7.5, its total enthalpy approaching 46.4 MJ/kg (20,000 Btu/lbm).

1.4 Overview of arcjet plasma diagnostics

Test articles, constructed to represent local spacecraft structures, are tested in the hypersonic arcjet flow to understand the capability of the materials and structures to withstand the anticipated local flight environment. The correlation between test condition and the flight condition is determined by comparing the predicted local flight environment to the arcjet flow environment. Understanding this arcjet environment requires complex analytical and experimental procedures, and is based on

numerical simulation. The accuracy of the simulations depends on the ability to measure the flow properties to test the simulation results. However, because of harsh, non-equilibrium, non-uniform, and fluctuating conditions, flow characterization has been a challenging task. The main diagnostics routinely used include measurements of heat flux, pressure, surface temperature. However, recently there has been increased interest in understanding the composition of the flow and its interaction with thermal protection materials. This has led to a few studies which implement modern spectroscopic and laser diagnostic techniques in the arcjet facilities, and has lead to the work in this thesis to develop diode laser based sensors for routine monitoring of the arcjet.

1.4.1 Diode laser based plasma diagnostics

Diode laser based trace gas sensors have been applied to harsh environments [4, 5]. Tunable diode laser absorption spectroscopy(TDLAS) has a great potential for plasma diagnostics because diode laser based sensors are compact, rugged, non-intrusive, sensitive, and quantitative.

The High Temperature Gasdynamics Laboratory (HTGL) has lead development of plasma diagnostics with semiconductor lasers since the early 1990's and different types of plasmas were studied with TDLAS and LIF. Baer [6, 8, 7] studied air plasmas with NIR diode lasers. He measured the temperature and the number density of Ar using tunable diode laser absorption spectroscopy at 811.5 nm in an rf plasma torch. Using laser-induced fluorescence at 810.4 nm, he also measured the population temperature and electron number density. Chang [9] measured the concentration and the temperature of atomic oxygen at 777.4 nm with tunable diode laser absorption spectroscopy. Cedolin [10] studied xenon Hall-thruster. He measured the concentration, the temperature, and the velocity of the excited state xenon and a metastable state with a semiconductor laser at 824 nm and 828 nm.

Industrial plasma-etching reactors have also been studied with tunable diode laser absorption spectroscopy. Sun [11] measured etching gas and etch product for endpoint detection [12] in the early 1990's. Haverlag [13] measured sputtering gas temperature,

and at Stanford, etching gases, HBr [14], HCl [15], and HF [16], were measured with a wavelength modulation technique.

Matsui [17, 18, 19] in Japan studied translational temperature in arc-heater plumes using diode laser absorption spectroscopy. A few ArI lines (840.46 nm, 842.40 nm, 852.10 nm, and 240.81 nm) and one OI line (777.89 nm) were studied. He found that the translational temperature increases with laser intensity even though inhomogeneous broadening theory predicts no change in Doppler width. Also he found that translational temperatures in the plume may differ between different species, which is one of the typical phenomena of a non-equilibrium flow. For example, the translational temperature of oxygen atoms can be higher than that of argon atoms by 25 to 63 %. Moreover both temperatures are far different from CFD analysis, which underpredicts the temperature by a wide margin .

1.4.2 Plasma diagnostics in the NASA Ames arcjet facilities

Scott [20] surveyed measurements of flow properties in the arcjet facilities before 1993, and these measurements are summarized in Table 1.1. Many of the diagnostics in the early work are intrusive. Probes for stagnation point pressure, heat flux, and electron temperature are inserted in the flow before the test model is inserted into the hypersonic flow. Some probe diagnostics are not time resolved, and cannot detect any changes during the material test. Non-intrusive optical diagnostics also have been successfully applied. Optical emission spectroscopy (OES) with an equilibrium assumption gives rotational, vibrational, electronic temperatures in the test cabin. OES is simple and can measure multiple species. However, in many cases, the spectral width is instrument limited, and scanning the wide spectral range takes a significant amount of time, and does not provide the needed time resolution. Laser-induced fluorescence (LIF), especially two photon LIF has been used for spatially resolved concentration, temperature, and even velocity in the test cabin. However, due to complex experimental procedures, two-photon LIF will not become a routine sensor to monitor the arcjet [21, 22].

In this thesis, diode laser absorption sensors are described to monitor N, O, Cu,

Ar, and K.

Copper concentration

The plasma is contaminated by copper vapor evaporating from the water-cooled copper electrodes and the constrictor tube, and the copper concentration is an important parameter for arcjet operation. First, extensive copper vapor might change electric conductivity of the plasma in the heater. Second, the rate of electrode erosion determines maintenance schedule. And third, if the copper concentration is high enough, the models of flow condition on the test object could be in significant error.

Previously, the copper contamination was measured by: weighing electrode assemblies, emission spectroscopy, and intrusive measurement devices. However, each of these methods provided contradictory and non-reproducible results. There is currently no commonly established and accepted standard for determination of copper contamination in the flow stream. Previous research suggests that when the local heat transfer rate is less than 40 MW/m^2, neither the constrictor nor electrode wall erode. If the electric discharge fluctuates, however, the instantaneous heat transfer rate can be much higher and erosion may occur. At high pressure ($\sim$ 100 atm) and with low L/D (length/diameter $\sim$ 20), the average copper erosion reported up to 200 ppm by mass and 110 ppm by mole [23] into the total mass flow. The most common method to measure copper concentration is to weigh the electrode assemblies, but this only gives averaged data, and must be done after dissembling the entire arcjet heater package. Another method is to compare copper optical emission intensities at 324 or 327 nm with other air emission lines. This actinometric method can be inaccurate for quantitative copper concentration. In the test cabin, the flow is not equilibrium, and the electronic temperatures of each species can be different, which further confuses the prediction of copper emission data. In addition OES requires a absolute intensity calibration to obtain quantitative data, and in the IHF heater the calibration process may be quite difficult and changes with time. For example, a sapphire window can become dirty, and the emission signal may decrease every run, even though the condition remain constant.

In this thesis copper is monitored by a diode laser absorption sensor in the heater.

Table 1.1: Various Arcjet flow parameters and diagnostics techniques

Parameters	Measurement technique
Stagnation point pressure	Pitot probe with pressure transducer
Heat flux	Gardon gauge Slug calorimeter
Enthalpy	Energy balance Sonic throat technique Heat flux and stagnation pressure
Species concentration	Mass spectrometer probe
Excitation temperature of atoms	Emission spectroscopy
Rotational temperature of molecules	Emission spectroscope Laser-induced fluorescence Electron beam fluorescence
Vibrational temperature of molecules	Emission spectroscopy Absorption spectroscopy Laser-induced fluorescence Electron beam fluorescence
Static temperature of electrons	Emission spectroscopy Continuum spectroscopy Doppler profiler Thomson scattering Electrostatic probes
Static temperature of gas Velocity	Laser-induced fluorescence Electrostatic probes Doppler laser Thomson scattering Doppler laser-induced fluorescence
Electron density	Electrostatic probes Continuum intensity Stark line broadening
Contamination	Weighing electrode assemblies Spectroscopy Intrusive measurement devices

The measurements reported here illustrate the potential for reliable, non-intrusive, real-time diagnostics to monitor plasma properties such as composition, temperature, and contamination levels using tunable diode laser absorption spectroscopy(TDLAS) as a sensor strategy.

Atomic nitrogen and oxygen concentration

With simple optical emission spectroscopy, multiple species can be monitored by scanning over relatively large spectral range. However, the atomic spectral width is usually narrower than the instrumental width. To achieve narrow instrumental width, a Fabry-Perot transmission filter can be used, but this requires extra data acquisition time. The run time of the IHF is as short as 20 sec at 150 MW, and traditional OES is limited. Especially in the test cabin, atomic species in excited states cascade down to the lower states depleting excited states. OES gives information of the excited states but cannot provide information on the metastable states or the ground state. Because only a small fraction of the atomic species are in the excited states after expansion, emission is weak in the free stream.

To access ground state atomic species in the test cabin, two-photon-excitation laser-induced fluorescence has been employed. The transitions from the ground state of atomic nitrogen and atomic oxygen are in the vacuum ultraviolet (VUV) range. Two-photon-excitation is used to excite the ground state atoms to the excited states using an ultra violet (UV) source which emits at half of the transition frequency.

Atomic nitrogen and oxygen are the main species in the air plasma. Diode laser absorption sensors are used to monitor excited electronic states of atomic oxygen and nitrogen. These absorption measurements provide real-time quantitative data without calibration. Single-photon absorption by the ground electronic state for the atomic species in the plasma is in the UV and the VUV, where diode lasers are not available. The ground states for most atomic species of air plasmas are not accessible due to limitations in available wavelength. The atomic species in metastable states or in excited states are accessible with near-infrared lasers. In the arc heater, reliable absorption measurements of atomic oxygen and atomic nitrogen are conducted to provide the concentrations of the excited state and the population temperature.

Argon concentration

To operate arcjet facilities, argon is added to the plasma in the NASA Ames facilties. Argon gas is only 1 % in ambient air; however to maintain the conductivity of the plasma, to sheath electrodes, and to inhibit oxide formation, 5 to 25 % of the flow is composed of argon. Generally OES is most often chosen to monitor argon. However, during the material tests, fast diagnostics are required to yield data during a short start-up period of 10 to 20 sec. Also, OES cannot measure metastable states or the ground state. The concentration of metastable states can indicate how much energy is stored in the electric energy states, which may impact estimates of the total enthalphy of the flow. Previous research to measure the total enthalpy of the flow by NASA Ames assumed that all atomic species were in the ground state. However, because of the extra argon added to the NASA Ames arcjet, there is a concern that the total enthalpy of the flow in the test cabin might be altered by a large concentration of argon in metastable state excited states.

Absorption measurements of two argon transitions from different metastable states are used here to monitor the start-up period and to set an upper limit on the number density of the metastable states in the test cabin. Two transitions in NIR are scanned with a single diode laser. The ratio of two transitions provides the excitation temperature, and the integrated absorbance provides the population of metastable states.

1.4.3 Previous plasma diagnostics at NASA Ames

Spectroscopy-based plasma diagnostics have previously been reported for the NASA Ames facilities. There are two arcjets: the aerodynamic heating facility (AHF) and the interactive heating facility (IHF). Both have the same configuration but operate with different conditions: the AHF is operated with up to 20 MW and the IHF with up to 60 MW.

Significant effort has been made to measure the properties of the flow with laser-induced fluorescence (LIF) and optical emission spectroscopy (OES) in the AHF [24, 25, 21, 22]. Two-photon LIF of atomic nitrogen has provided spatially resolved

ground-state nitrogen concentration, the translational temperature, and the velocity of the free stream flow in the test cabin. LIF measurements are spatially resolved, relatively fast, but require calibration with a reference cell measurements. The large laser systems and sensitive optics alignment require significant effort and large capital cost, and thus the two-photon LIF measurements are not suitable for a routine sensor. OES measurements have also been made in the shock layer to determine the population and the energy distribution of excited states using a fiber optic coupled spectrometer covering wide spectral range from 400 nm to 900 nm with a resolution of 5 nm.

In the IHF, only non-optical diagnostics have been previously applied. High-pressure water-cooled dwell probes, called Gardon gages, have been used to measure heat flux and pressure, and the enthalpy is then calculated [26]. Surface heat flux, and stagnation pressure are matched to those expected during the flight. Calorimeters are fundamental tools to measure properties in the test cabin to correlate ground test results with flight test predictions, and provide empirical data for validation of aerothermal codes. However the Gardon calorimeter has a large uncertainty: the heat flux measurements and previous slug calorimeter measurements have a discrepancy of 25 %, and relative measurements during the same test differed as much as by 15 %.

1.5 Motivation

Diode laser based absorption sensors are developed here to demonstrate the potential for routine sensing in the arcjet facilities. Most simulation codes assume that the heater flow is in equilibrium and deduce temperature from energy balance. Presented here are the first time-resolved measurements of the heater temperature.

Diode laser absorption sensors can provide a rapid temperature data rate for the entire process enabling fluctuations of the heater to be monitored. Temperatures can be deduced from different species and from different physical principles, and these measurements validate the equilibrium assumption in the arc heater. These measurements can be used to understand changes in the plasma as the gas flow and

electric current are changed. Finally these measurements lead to real-time heater diagnostics, which can be calibrated to establish a proper maintenance schedule.

Copper is the dominant contamination in the arcjet facilities, and results from electrode and constrictor ring erosion. The contamination to the test flow could be significant and modification of simulation codes might be needed to include this effect. The measurements here show the copper content is small and not a significant contribution to the flow enthalpy. The electrode erosion determines maintenance schedule, and the copper sensor provides a useful estimation of the electrode erosion.

Observation of transient start-up conditions was made in the test cabin. These observations place an upper bound on the metastable energy content in the test cabin flow.

Chapter 2

Theory

In this chapter, the basic theory of diode laser operation is briefly summarized. Absorption lineshape theory is important to design and interpret the measurements reported here. Various broadening and splitting mechanisms are discussed. Finally the properties of a plasma in local thermal equilibrium are summarized.

2.1 Fundamentals of diode lasers

Since their invention a few decades ago, diode lasers are now used in quantity for several very practical applications, for example, compact disk (CD) players, digital versatile disk (DVD) players, and telecommunication network systems. Spectroscopic measurements using wavelength-tuned diode laser sensors have become a very important research tool for a wide variety of harsh environments. Diode lasers are compact, rugged, easy to use, and relatively cheap. Fiber-coupled lasers are especially easy to align for field measurements. The narrow spectral width and fast tunability make diode lasers attractive as a wavelength-tuned optical absorption gas sensor. In this thesis, diode lasers will be wavelength-tuned to match several atomic absorption lines in the plasma heater and test cabin plume. From the amount of absorption and the spectral shape, the gas temperature will be extracted.

2.1.1 p-n junction

Light generation inside the p-n junction from energy loss by the conduction band of the semiconductor material is the fundamental principle of semiconductor lasers. A clear and simple theoretical description can be found in Davis [27], and more rigorous explanations can be found in Bhattacharya [29]. For direct band gap semiconductors, the momentum or wave vector of electron does not change significantly, and much more efficient than indirect band gap semiconductors in recombination. Thus, direct band gap semiconductors, such as GaAs, are used most often. The energy spacing, between the lowest unfilled states in the conduction band and the highest occupied states in the valence band, is called the band gap, E_g. The band gap of the active region determines the wavelength generated; $\lambda = hc/E_g$, where h is Plank's constant and c is the speed of light.

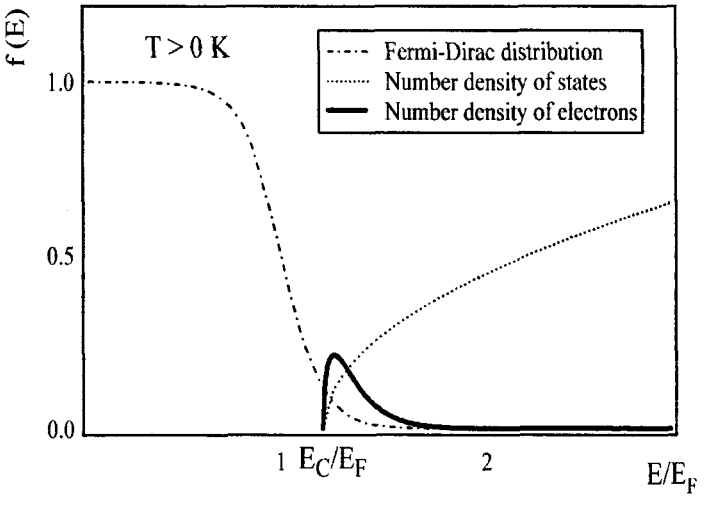

Figure 2.1: Fermi-Dirac distribution, the number density of state and the number density of electrons in conduction band

Electrons are distributed according to Fermi-Dirac statistics, as follows.

$$f(E) = \frac{1}{1 + exp^{(E-E_F)/kT}} \tag{2.1}$$

where E_F is called the Fermi level, which is the chemical potential of electrons in the semiconductor. The Fermi-Dirac distribution is shown in Fig.2.1. The electron concentration in a small energy grid dE is obtained by multiplying the number of states by the probability for an electron to occupy that state.

Simple statistical mechanics shows that the number of states in the conduction band per unit volume with energy within dE is

$$\rho(E)dE = \frac{1}{2\pi^2}\left(\frac{2m_c^*}{\hbar^2}\right)^{3/2}\sqrt{E - E_c}dE \tag{2.2}$$

where m_e^* is the equivalent electron mass in the semiconductor and E_c is the lowest energy of conduction band. The number of electrons with energy within dE is then,

$$dn = f(E)\rho(E)dE \tag{2.3}$$

This can be illustrated graphically as in Fig.2.1.

For semiconductors, at a temperature $T > 0$ K, a significant fraction of electrons are in the conduction band, and similarly holes are present in the valence band. When doped with donors, the semiconductor is called n-type, and when doped with acceptors, then it's called p-type. Doping shifts the Fermi level to the conduction band for n-type and to the valence band for p-type.

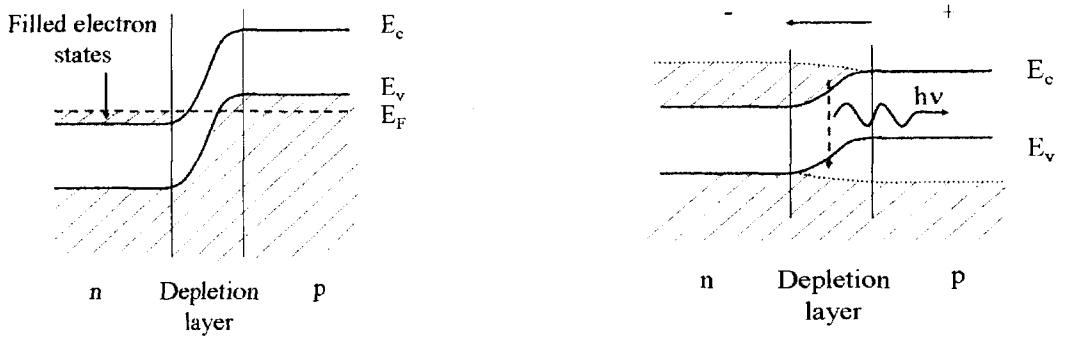

(a) (b)

Figure 2.2: pn-junction for (a) unbiased (b) biased

For a forward biased p-n junction, excess carriers are recombined in the depletion

layer, and a conduction band electron falls into an empty valence band. The excess energy is emitted as light. This spontaneous emission is the basis for light emitting p-n diodes. At a high bias current, there can be a large enough fraction of electrons in the conduction band and holes in the valence band, to produce a population inversion. Fig.2.2 shows schematically how forward baising can generate a population inversion. This population inversion is required for laser operation, as it provides gain on the stimulated emission, and therefore generates coherent light. When gain from population inversion from stimulated emission exceeds cavity loss, lasing is observed. The injection current needed to initiate lasing is called the threshold current.

2.1.2 Lasers and double heterojunction

Lasers have three components: gain medium, optical cavity, and pumping mechanism. Semiconductor lasers use injection current to provide pumping, and a narrow doped semiconductor layer as the gain medium. Simple semiconductor lasers use both end facets as cavity mirrors, while others such as DFB lasers use multiple layers of dielectric coating as cavity mirrors.

Lasers are complex structures. For example, to increase recombination soon after crossing the junction, double heterojunction structures were developed. A heterojunction is a junction of different materials with similar lattice constants. Three different crystals, such as N-GaAlAs, p-GaAs, P-GaAlAs, are assembled [30]. The p-type to P-type heterojunction still operates like traditional diode junction, and of course N-type to p-type does too. With sufficient forward biasing, p-GaAs behaves as a active layer, and population inversion in the active layer can be achieved. Schematically this is shown in Fig.2.2.

Double heterojunction structures are also index-guided. The active layer has a higher index of refraction than the confining layers, providing excellent transverse mode control.

Currently several different diode laser architectures are employed as gas sensors. Cheap but difficult to use Fabry-Perot lasers have been replaced with distributed feedback (DFB) lasers and vertical cavity surface emitting lasers (VCSELs), which

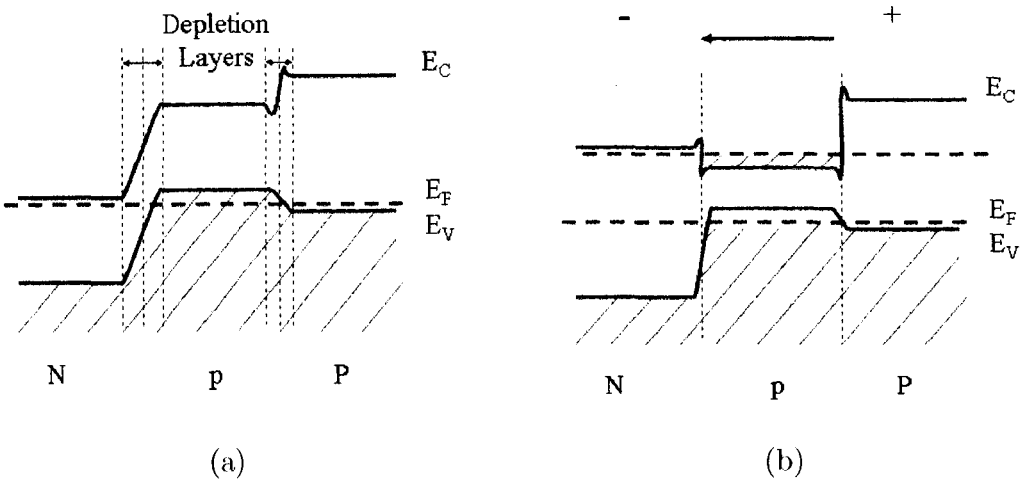

Figure 2.3: Double Heterojunction (a) Unbiased (b) Forward-bias and population inversion

provide single-mode operation with a high sideband suppression ratio. VCSELs are especially attractive light sources, for their wide wavelength tuning and low power consumption. Other types of laser architecture such as quantum cascade lasers or external cavity lasers have been also used in many field and lab experiments. However, they are not employed in experiments performed here and will not be discussed further.

2.1.3 FP lasers

Fabry-Perot (FP) lasers are the cheapest and simplest type of diode lasers. FP lasers have two cleaved edges, and these surfaces act as cavity mirrors. Between the mirrors, there is a long stripe gain medium with perpendicular current pumping. There is no mode-selecting mechanism except the index-guided structure, therefore FP lasers tend to operate on multiple cavity modes simultaneously. Due to index-guided structure, one or two transverse modes can dominate at currents well above threshold current. Usually the operating temperature and current are selected carefully to promote one dominate mode. In our spectroscopic application, we limit our uses of FP lasers to devices which can be operated single-mode.

FP lasers have a few disadvantages: the spectral width (FWHM) of single mode lasers is around 40 MHz, which is a few times larger than common DFB lasers [31]. Also FP lasers are very sensitive to back-reflections; such back-reflections from any surface re-entering the laser cavity causes unstable laser output. Thus, an optical isolater is necessary when using a FP laser. Another serious problem with FP lasers is hopping between cavity modes when the FP lasers are injection current tuned in wavelength. When injection current increases, the output wavelength decreases linearly until at a specific current the output wavelength jumps between cavity modes. Because the mode spacing is 0.7 nm - 2 nm, modehops limit wavelength tuning, and thus FP lasers should be employed carefully.

2.1.4 DFB and DBR lasers

Distributed feedback (DFB) lasers and distributed Bragg grating (DBR) lasers provide stable, single spectral operation. With a mode selecting structure, more than 50 dB sidemode suppression ratios are easily achieved. Commercial DFB lasers have the spectral width (FWHM) of 10 MHz, and specially designed lasers can have less than 1 kHz [32] with frequency locking.

DFB lasers and DBR lasers replace the cleaved face architecture with wavelength selective architecture. For example, DFB lasers have periodic structures called Bragg reflectors built over a substantial length of gain region near the active layer. On the other hand, DBR lasers use Bragg reflectors at both ends of gain region. Light that satisfies the Bragg condition is reflected efficiently, and this Bragg condition selects lasing wavelength.

However, DFB or DBR lasers are not always the best choice for absorption spectroscopy sensors. For atomic spectroscopy, saturation can be a serious problem, and saturation intensity is proportional to laser linewidth. Therefore the narrow spectral width of DFB lasers can have a very small saturation intensity. This can broaden the absorption via power broadening or decrease the signal to background ratio. And in high-pressure and high-temperature environments, it can be useful to scan the wavelength over a wider range ($\sim 5\ cm^{-1}$) to cover wide absorption features. For these

wavelength agile applications, VCSELs are preferred over DFB lasers.

2.1.5 VCSELs

Nearly 92 % of all diode lasers are edge emitting. Edge emitting lasers use end facets or Bragg reflectors as cavity mirrors, and light propagation direction is perpendicular to the direction of current. However some lasers are built as surface emitters, and vertical cavity surface emitting lasers (VCSELs) are one type of surface emitting semiconductor lasers. VCSELs have multiple dielectric coatings on top and bottom, and light propagates the same direction as current. These dielectric reflectors enable VCSEL architecture. With a stack of quarter waveplates, called a Bragg reflector, reflected light from one waveplate boundary is constructively interfered with reflected light from another boundary, quarter wave Bragg reflectors are depicted in Fig.2.4.

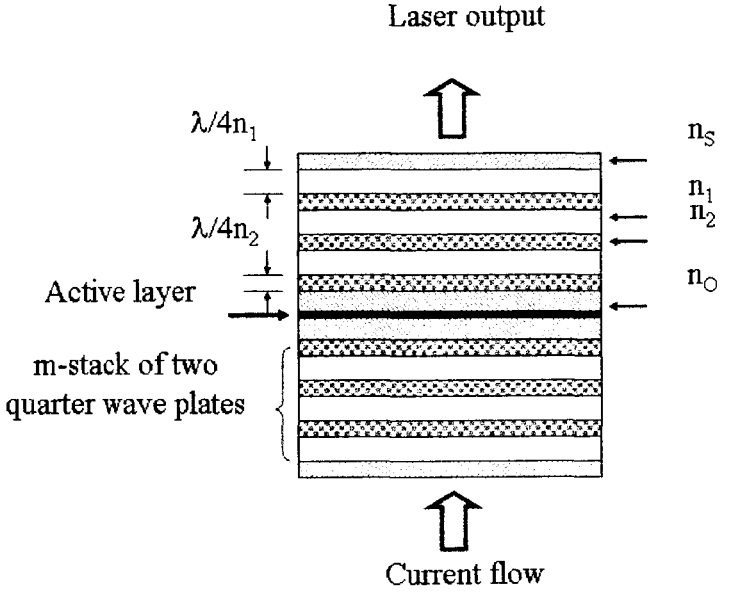

Figure 2.4: Schematic of VCSEL: gain(active) region in the center, cavity mirrors of quarter wave plate, and pumping of injection current

The reflectivity R at the resonant wavelength of a stack with m non-absorbing dielectric pairs assuming transverse electromagnetic mode (TEM) is given below by

solving Maxwell's equation.

$$\sqrt{R} = \frac{1 - \frac{n_s}{n_o}\left(\frac{n_1}{n_2}\right)^{2m}}{1 + \frac{n_s}{n_o}\left(\frac{n_1}{n_2}\right)^{2m}} \tag{2.4}$$

By selecting $n_1 < n_2$ and m ~20, reflectivity can be larger than 99 %.

VCSELs have several advantages over edge emitting lasers: 1) Due to their much smaller size (edge emitting diodes are typically 100 to 200 μm long, 4 μm wide, and 0.5 μm high. VCSELs are 5.5 μm high and 1 to 5 μm diameter), a very large number of VCSELs can be fabricated on a given area. 2) VCSELs have large cavity mode spacing due to smaller dimension . Therefore single mode operation is more easily achieved. 3) Due to the small size and cylindrical shape of emitting surface, VCSELs have a circular beam profile unlike the elliptical beam from edge emitting lasers. A circular beam has higher coupling efficiency into an optical fiber than an elliptic beam from an edge emitting diode, and this makes VCSELs attractive for sensors and telecommunications. 4) Many VCSELs and electronic circuits can be manufactured on a same wafer. This may make optical computing and optical interconnect applications possible. 5) The active layer is small and therefore it has small threshold current, or low power consumption. 6) VCSELs can have very wide tuning range without longitudinal modehop due to large cavity mode spacing and small thermal mass of the active volume. Thus VCSELs are attractive for wide tuning measurements such as high-pressure or high-temperature gas flows [33]. In the plasma sensors demonstrated in this thesis, VCSELs were the laser source of choice when available.

2.2 Lineshape and broadening

The intensity of light decreases exponentially as the beam propagates through an absorbing medium, known as Beer-Lambert's law [34].

$$\frac{I(\nu)}{I_0} = exp(-SnL\phi_\nu) \tag{2.5}$$

where $I(\nu)$ is the transmitted intensity at frequency ν, I_0 is the incident intensity, S is the linestrength of the transition proportional to Einstein B coefficient, and ϕ is

the lineshape function. A lineshape function is normalized so that the integral of a lineshape function is unity: $\int \phi_\nu d\nu = 1$

Proper modeling of lineshapes is crucial for quantitative data analysis. General formulations of lineshape functions can be made by three approaches: 1) classical methods based on an oscillator model with the impact approximation, 2) the quasi-classical approximation with the density matrix method, and 3) quantum mechanical methods by solving Schrodinger's equation considering the relative motion of atoms and perturbing particles. These are concisely explained by Sobelman [35] and more extensively studied by Griem [36]. For general lineshapes, no analytical formulae are available without approximations, and only numerical simulation is possible. Unperturbed Hamiltonian and additional potentials due to perturbing gases, such as neutral gases, electrons, and ions, are used to calculate density matrices, and general lineshapes considering collisions are constructed from the density matrix. The Doppler effect can be included with frequency shift due to velocity and averaging over velocity with a Maxwellian weighting. However, general lineshape theory is beyond the scope of this short summary, and for the practical applications here only a few dominant broadening mechanisms and corresponding lineshapes are needed.

There are two types of broadening: homogeneous which influences the entire distribution of absorbers, and inhomogeneous which influences each subset of the absorber distribution differently. These different physical mechanisms have different influence over the absorber distribution, and therefore result in different lineshapes. Some of the most common broadening mechanisms are discussed here: natural broadening, Doppler broadening, Stark broadening, van der Waals broadening, resonance broadening, and power broadening.

2.2.1 Natural broadening

Natural line broadening is a fundamental broadening related with the radiative decay rates of states involved in a transition. One form of the Heisenberg uncertainty principle is $\Delta t \Delta\omega \approx 1$. A finite lifetime, which is the inverse of the radiative decay rate, then is related to a finite uncertainty of the transition frequency. This was

classically described by Demtroder [37] and key results are summarized here. A effective damping constant is defined as

$$\gamma_{nm} = \sum_{m'} A_{m'n} + \sum_{n'} A_{n'm} \tag{2.6}$$

in situations where spontaneous decays to various levels m' and n' are possible from upper (m) and lower (n) levels of the transition. The lineshape is a Lorentzian profile with a full width half maximum (FWHM) of γ as Eq.(2.7)

$$I(\omega - \omega_o) = I_o \phi_L(\omega - \omega_o) \tag{2.7}$$

and

$$\phi_L(\omega - \omega_o) = \frac{1}{2\pi} \frac{\gamma}{(\omega - \omega_o)^2 + (\gamma/2)^2} \tag{2.8}$$

The transitions considered here have a lower state that is either a long lifetime metastable state or the ground state, and an upper state with a lifetime of order 10 ns. The corresponding natural width is of order 16 MHz for such transitions. Other mechanisms, such as Doppler, Stark, van der Waals, or resonance broadening, result in significantly broader lineshapes, and are thus more dominant than natural broadening with the work discussed here.

2.2.2 Doppler broadening

In equilibrium, the velocity distribution of a gas follows Maxwell-Boltzmann statistics. The velocity distribution is Gaussian and the corresponding normalized lineshape is Gaussian as in Eq.(2.9)

$$\phi_D(\nu) = \frac{2}{\Delta\nu_D} \left(\frac{ln2}{\pi}\right)^{1/2} exp\left[-4ln2\left(\frac{\nu - \nu_o}{\Delta\nu_D}\right)^2\right] \tag{2.9}$$

$$\Delta\nu_D = \nu_o \left(\frac{8kTln2}{mc^2}\right)^{1/2} \tag{2.10}$$

where $\Delta\nu_D$ is Doppler width (FWHM), and ν_o is the center frequency.

In a plasma, especially at low-pressure, Doppler broadening is one of the most dominant broadening mechanisms. However, at high-pressure or a high electron density plasma, other mechanisms must be considered.

2.2.3 Van der Waals broadening

Van der Waals broadening is a common broadening mechanism for collisions between neutral gases (often called pressure broadening). The van der Waals potential is generally modeled as a Leonard-Jones $a/R^{12} - b/R^6$ potential, and for long range interaction, only $-b/R^6$ is important. Breene [38] approximated the broadening width (FWHM) and shift due to van der Waals effect as:

$$w = 2.68 N_g b^{2/5} \overline{v}^{3/5} \tag{2.11}$$

$$d = 0.97 N_g b^{2/5} \overline{v}^{3/5} \tag{2.12}$$

The half width half maximum (HWHM) w and line shift d were also estimated by Griem[40].

$$w/2 \approx 2\pi N_g v \rho_0^2 = 2\pi N_g \overline{v} \left(\frac{9\pi\hbar^5 (\overline{R^2})}{16 m_e^3 E_p^7} \right)^{2/5} \tag{2.13}$$

$$d \approx -1/3w \tag{2.14}$$

and

$$R^2 = \frac{1}{2} \frac{E_L}{E_\infty - E_a} \left[5 \frac{E_H}{E_\infty - E_a} + 1 - 3 l_a (l_a + 1) \right] \tag{2.15}$$

where N_g is the number density of the perturbing gas, v is the velocity of the radiator, m_e is the mass of the electron, E_p is the excitation energy of the perturber, E_H is the ionization energy of hydrogen,A_∞ is the neutral radiator's ionization energy, E_a is the energy of the upper level of the transition, and l_a is the orbital angular momentum quantum number of this level. Comparison of Eq.(2.12) and Eq.(2.14) allows the coefficient for Leonard-Jones potential to be estimated. In high-temperature plasma spectroscopy, van der Waals broadening is three orders smaller than Doppler or Stark broadening, and is usually neglected.

2.2.4 Resonance broadening

Another collision broadening mechanism is possible when the collision partner is identical to the target species. This becomes important for absorption or emission, when the initial state of the radiator has a direct transition to the ground state. In contrast to other types of collision broadening, resonance broadening is independent of velocity, and the lineshape remains nearly Lorentzian. Linewidth (FWHM) due to resonance broadening was approximated as [39]:

$$w \approx 3\pi \left(\frac{g_g}{g_i}\right)^{1/2} \frac{e^2 f_{gi}}{4\pi\epsilon_1 m_e \omega_{ig}} N_g \tag{2.16}$$

where N_g is the number density of the ground state, g_g and g_i are the degeneracy of ground and initial state of radiator respectively, f_{gi} is the oscillator strength of a transition between ground state and initial state of radiator, and ω_{ig} is the corresponding frequency. The oscillator strength for the transition from metastable states to the ground state is small and resonance broadening can be ignored.

2.2.5 Stark broadening

Electrons and ions co-exist with neutral atoms in partially ionized gases. Collisions with electrons are a more important broadening mechanism than collisions with neutral species in partially ionized plasmas. The potential between neutral radiators and charged particles is modeled as c_4/R^4. The Coulomb potential between charged particles is c_1/R, and the corresponding interaction is described by the linear and quadratic terms from the Stark effect. The linear Stark effect causes only broadening however, the quadratic Stark effect causes broadening, shift and asymmetry in lineshape. A more rigorous approach can be made with calculations of electron impact and local ion microfields. Readers may refer to Griem [40] for details. However Seaton's [41] empirical formulae for N and O can be used within a factor of 2.

The Stark broadening width (FWHM) due to collisions with electrons can be estimated as [41]:

$$w = 3.41 \left(R_i + R_f\right)^{1.21} \left(T/10^4\right)^{0.22} \tag{2.17}$$

where R_i and R_f are the quantities using f values.

Another approximation from the quasi-classical calculation by Sobelman [35] gives line shape broadening (HWHM) and shift:

$$w = n_e \overline{v}^{1/3} \left(\frac{\pi}{2}\right)^{5/3} \Gamma\left(\frac{1}{3}\right) C_4^{2/3} J'(\beta) \tag{2.18}$$

$$d = \frac{1}{3} n_e \overline{v}^{1/3} \left(\frac{\pi}{2}\right)^{5/3} \Gamma\left(\frac{1}{3}\right) C_4^{2/3} J''(\beta) \tag{2.19}$$

where n_e is the electron number density, $\overline{v}$ is the electron velocity, J is the zeroth order Bessel's function, and C_1 and β are defined as

$$C_4 = \frac{2e^2 a_0^3}{\hbar} f \left(\frac{Ry}{\triangle E}\right)^2 \tag{2.20}$$

$$\beta = \left(f \frac{Ry}{\triangle E}\right)^{1/2} \frac{\triangle E}{m\overline{v}^2} \tag{2.21}$$

where a_0 the radius of the radiator, Ry is energy difference for Rydberg line, $\triangle E$ is the energy difference between upper and lower state, and f is the oscillator strength.

However, Stark broadening for most atomic species may not simply estimated from Eq.(2.17) or Eq.(2.18). Instead usually each spectral line is individually numerically calculated [39, 40].

By extracting homogeneous broadening width from a spectral lineshape, Stark broadening can be used to extract electron density if other parameters, such as electron temperature and neutral pressure, are measured independently.

2.2.6 Transit-time broadening with a Gaussian beam

A Gaussian beam profile is usually accepted for a singlemode laser beam operating in fundamental mode. A fast moving gas traversing the beam perpendicular to the direction of beam propagation, has a limited transit-time to interact with the beam; this is another line broadening mechanism. Shimoda [42] showed that the broadened

lineshape is Gaussian with FWHM w

$$w = 1\sqrt{2ln2}\,(v/D) \tag{2.22}$$

where v is the velocity of the gas, and D is the beam diameter. In free space diode laser absorption experiments, usually beam diameter is order of 1 mm. In the test cabin of the IHF, the transit-time broadening is maximum. With the gas velocity of 10 km/sec, transit-time broadening is only 90 MHz, which is far less than other broadening mechanisms and can be neglected here.

2.2.7 Voigt lineshape

If broadening mechanisms are independent, different line profiles must be convoluted to get a correct lineshape. For example, if the Gaussian Doppler broadening and Lorentzian collision broadening are both important, then the convolution of two lineshapes produces a Voigt profile.

$$\phi_{Voigt}(\nu) = \int_{-\infty}^{\infty} \phi_{Gaussian}(\nu')\phi_{Lorentzian}(\nu - \nu')d\nu' \tag{2.23}$$

The normalized lineshape of the Voigt profile is called Voigt function, $V(a,\omega)$. Here a is the Voigt parameter defined as a ratio of a collision broadening width, $\triangle\nu_C$, to a Doppler broadening width, $\triangle\nu_D$:

$$a = \frac{\sqrt{ln2}\triangle\nu_C}{\triangle\nu_D} \tag{2.24}$$

For $a \ll 1$, the lineshape is close to Gaussian, and for $a \gg 1$, then the lineshape is close to Lorentzian. The normalized wavenumber ω is defined as:

$$\omega = \frac{2\sqrt{ln2}(\nu - \nu_0)}{\triangle\nu_D} \tag{2.25}$$

The Voigt profile can be approximated by complex functions [43] but usually it is calculated numerically [44].

2.2.8 Power broadening

At low laser intensity, the population change by the interaction with the field is negligible. Therefore, spontaneous emission or absorption is independent of the laser intensity. However at high laser intensities, the lower state of a species involved in a transition can be depleted and significant changes can be observed in absorption or spontaneous emission. The changes in signal includes broadening and peak absorbance, and are different for homogeneously and inhomogeneously broadened spectral lines.

Saturation intensity for closed two level system

As explained by Demtroder[37], the population of states for the absorption from ground state or metastable states can be approximated as a closed two level system. Two closed level system has no relaxation to other levels, as shown Fig.2.5. The rate

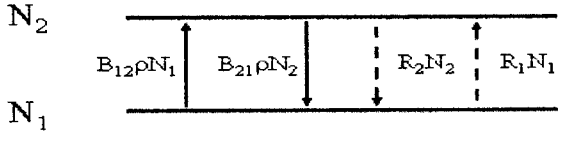

Figure 2.5: Two closed level system

equations for two states are

$$\frac{dN_1}{dt} = -\frac{dN_2}{dt} = -B_{12}\rho N_1 - R_1 N_1 + B_{21}\rho N_2 + R_2 N_2 \tag{2.26}$$

The difference of population between two states, ΔN can be expressed with spectral energy density, $\rho(\nu)$, relaxation constants, R_1 and R_2, and Einstein's B coefficients, B_{12} and B_{21}, with steady state assumption, as Eq.(2.27).

$$\Delta N \equiv N_1 - N_2 = N\frac{B_{21}\rho + R_2 - B_{12}\rho - R_1}{B_{12}\rho + B_{21}\rho + R_1 + R_2} \tag{2.27}$$

The unsaturated population difference is given as

$$\Delta N^0 \equiv N_1^0 - N_2^0 = \frac{R_2 - R_1}{R_1 + R_2} N^0 \tag{2.28}$$

If we assume spontaneous emission is the only relaxation mechanism, and collisional excitation is negligible, then $R_2 = A_{21}$ and $R_1 = 0$. Here A_{21} is Einstein's A coefficient.

Then the saturation spectral energy density is the energy density when $\Delta N = \Delta N^0/2$, and given as Eq.(2.29) with the relationship of $g_1 B_{12} = g_2 B_{21}$:

$$\rho_s = \frac{R_2}{3B_{21} - B_{12}} = \frac{A_{21}}{B_{21}(3 - g_2/g_1)} \tag{2.29}$$

With the relation between A_{21} and B_{21}

$$A_{21} = \left(\frac{8\pi h\nu^3}{c^3}\right) B_{21} \tag{2.30}$$

the saturation intensity is written as

$$I_s = \rho_s \Delta\nu_L c = \left(\frac{8\pi h\nu^3}{c^3}\right) \frac{\Delta\nu_L c}{(3 - g_2/g_1)} \tag{2.31}$$

Saturation intensity for closed two level system

For excited states, the saturation should be modeled with open two level energy model which allows for the loss from the lower level. For the simplest open two level system, the system diagram is presented in Fig.2.6.

In this model, only relaxation to the ground state is considered. The rate equations are

$$\frac{dN_1}{dt} = -B_{12}\rho N_1 + B_{21}\rho N_2 - R_1 N_1 + R_2 N_2 + R_0 N_0 \tag{2.32}$$

$$\frac{dN_2}{dt} = B_{12}\rho N_1 - B_{21}\rho N_2 - R_2 N_2 \tag{2.33}$$

where N_0 is the ground state population.

When transit time or diffusion time is much larger than excited relaxation times,

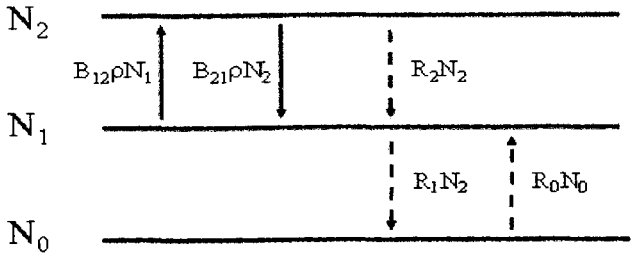

Figure 2.6: Open two-level system

which is in many cases, a steady state assumption can be applied. The number density of ground state is large enough that population change of upper state does not effect ground state population. Therefore N_0 can be considered a constant.

The population difference in steady state is given as

$$\Delta N \equiv N_1 - N_2 = \frac{N_0 R_0 (B_{21}\rho + R_2 - B_{12}\rho)}{B_{21}\rho + R_1 + R_2} \tag{2.34}$$

The unsaturated population difference is obtained by setting $\rho = 0$, and

$$\Delta N^0 = N_0 \frac{R_0}{R_1} \tag{2.35}$$

The saturation density is given similarly to Eq.(2.29),

$$\rho_s = \frac{R_2}{2B_{21} - B_{12}} = \frac{A_{21}}{B_{21}(2 - g_2/g_1)} \tag{2.36}$$

Again, with the assumption that simultaneous emission is the only relaxation process, $R_2 = A_{21}$. Similarly, the saturation intensity is written as

$$I_s = \rho_s \Delta\nu_L c = \left(\frac{8\pi h\nu^3}{c^3}\right) \frac{\Delta\nu_L c}{(2 - g_2/g_1)} \tag{2.37}$$

Saturation lineshape

When the intensity of the laser beam is comparable with saturation intensity, the lineshape of absorption or fluorescence is changed. Siegman [45], Demdroder [37], and Davis [27] all present saturated lineshapes in detail. Note that inhomogeneous and homogeneous broadening mechanisms show different lineshapes.

In the inhomogeneous case, the saturated absorption lineshape $\phi_S(\omega)$ is given:

$$\phi_S(\omega) = \frac{\phi^0(\omega)}{\sqrt{1+S_c}} \tag{2.38}$$

where $\phi^0(\omega)$ is unsaturated absorption lineshape, S_c is saturation parameter in the linecenter, defined as $S_c \equiv I_{center}/I_s$, where I_{center} is the laser intensity at the center of a transition. Therefore a Gaussian lineshape is still Gaussian, with only amplitude decrease by a factor of $\frac{1}{\sqrt{1+S_c}}$ while keeping the linewidth the same.

For the homogeneous case, the saturated lineshape is more complex. A Lorentzian lineshape remains Lorentzian, but the amplitude of absorption decreases while the linewidth increases.

$$\phi_S(\omega) = \frac{\phi_0(\omega)}{\sqrt{1+S_\omega}} \tag{2.39}$$

$$S_\omega = S_c \frac{(\gamma/2)^2}{(\omega-\omega_0)^2 + (\gamma/2)^2} \tag{2.40}$$

For a Lorentzian lineshape, the linewidth is broadened by a factor of $\sqrt{1+S_c}$ as Eq. (2.41).

$$\gamma_S = \gamma\sqrt{1+S_c} \tag{2.41}$$

When collision broadening is not negligible and the intensity of the probe laser is comparable with saturation intensity, then, the lineshape tends to broadened. However the Doppler broadened component is unchanged.

For a Voigt profile, the lineshape is a convolution of the homogeneously broadened Lorentzian function and the inhomogeneously broadened Gaussian function. As may be expected, the peak intensity decreases while the spectral width increases for a saturated Voigt profile. When broadening mechanisms are independent, only

the homogeneous component is broadened while the inhomogeneous component is unchanged. Thus the Voigt parameter a_s increases

$$a_s = a_0\sqrt{1+S_c} \tag{2.42}$$

where a^0 is the unsaturated Voigt parameter.

Therefore the saturated Voigt lineshape can be written:

$$\phi_{S,Voigt}(\nu) = \frac{\phi_{0,Voigt}(0)}{\sqrt{1+S_c}} V(a_s,\nu) \tag{2.43}$$

where $\phi_{0,Voigt}(0)$ is the unsaturated lineshape at the center.

Because of possible saturation in the heater, the laser intensities used in the experiments were attenuated below 10 % of saturation intensities for each transition, tabulated in Table 2.1. For low intensity absorption, power broadening can be neglected within the uncertainty of 5 %.

Table 2.1: Saturation intensity

	N*	N**	O**	Cu*
Wavelength, nm	824.2	856.8	777.2	793.3
Saturation intensity, $\mu W/mm^2$	450	160	210	500

* Typical singlemode FP lasers with spectral bandwidth of 50 MHz

** Typical VCSELs with spectral bandwidth of 20 MHz

The linewidth (FWHM) in the heater is tabulated in Table 2.2. In the heater, the temperature is high and the Doppler broadening is significant. However, pressure is also high, and pressure broadening must also be considered. In the test cabin, the pressure is low and the temperature is relatively high. Transitions from metastable states or ground state in the test cabin are mostly broadened by Doppler broadening. Stark broadening is negligible, due to small electron density in the partially ionized air plasma.

Table 2.2: Line width (FWHM in GHz) in the heater

	N	N	O	Cu
Wavelength (nm)	824.2	856.8	777.2	793.3
Doppler* broadening	5.62	5.40	5.57	4.05
Stark** broadening	1.31	1.32	0.96	-
Resonace broadening	0.08	0.16	≈ 0	≈ 0

* Heater temperature was assumed as 6,500 K

** Electron number density is assumed as $n_e = 1.89 \times 10^{15}\ cm^{-3}$

2.2.9 Zeeman effect

In a magnetic field, a transition can be split into multiple lines, and this phenomenon is called Zeeman splitting. The physics of Zeeman splitting can be explained by a classical description. The orbit of an electron around the nucleus is equivalent to a small electric current loop and thus produces a magnetic moment. In an applied magnetic field, the different angular momentum sub-levels, which have a different magnetic moment, are split by this field. To the first order approximation, the splitting is proportional to the strength of magnetic field.

Quantum mechanics limits the angular momentum to certain discrete directions. These magnetic sub-levels M of the angular momentum J in the direction of the field can be only an integral or half-integral multiple of $h/2\pi$. As the energy of electron in a magnetic field is discrete and because of discrete energy levels, the magnetic field can split a single transition line into multiple lines.

Because the electron splitting is usually 1000 times larger than nuclear splitting, we only consider electron splitting effect in a magnetic field.

The Zeeman effect is categorized as: normal Zeeman effect, anomalous Zeeman effect, and strong Zeeman effect. The normal Zeeman effect occurs for singlets in a weak magnetic field. The anomalous Zeeman effect is observed for all states that are not singlet in a weak magnetic field. The anomalous Zeeman effect includes a term, called Lande's g factor, which considers both angular momentum and spin momentum. In a strong magnetic field, the anomalous and normal effects combine to

become the strong Zeeman effect. Angular (L) and spin (S) electron momenta become uncoupled, and instead of total angular momentum (J), to the first approximation, two quantum numbers for angular and spin electron momentum are quantized independently. Each quantum number is then, $M_L = -L, -L+1, \cdots, L-1, L$ and $M_S = -S, -S+1, \cdots, S-1, S$. The energy level for given M_L and M_S is

$$E = E_0 + hoM_L + hoM_S \tag{2.44}$$

where E_0 is the unshifted energy level, h is Plank constant, and o is the precessional frequency called Larmor frequency. Quantum mechanics only allows the transitions with a selection rule of $\triangle M_L = 0, \pm 1$, $\triangle M_S = 0$, and $M_S = 0$ to $M_S = 0$ is not allowed.

More rigorous treatment produces an energy level with a correction term for L and S interaction. This term can increase the total number of lines, while space between transitions are still integer of ho.

In the Ames arcjet, there are both constant and rotating magnetic fields. The arc attachment to the electrodes is constantly rotated by a current induced magnetic field in the heater to stabilize the plasma and to confine the plasma near the core of the flow. Four turns of coil inside the electrodes with high current induces a strong magnetic field. Therefore the Zeeman effect must be considered in a lineshape analysis for all measurements.

2.3 Equilibrium plasmas

At the elevated temperatures in the arc heater the thermal equilibrium of air has significant dissociation of the molecular nitrogen and oxygen, and some of these neutral atoms and molecules are ionized. The charged species form a plasma, which is still electrically neutral.

Local thermodynamic equilibrium (LTE) is assumed in the analysis of the arcjet heater data. The time-scale for temporal and spatial variations due to convection or diffusion is much larger than the collisional time scale, which produces LTE. LTE

plasmas can be described by a few key properties. All equilibrium properties of gas of known composition can be determined by two independent properties: temperature and pressure or conversely temperature and volume [46]. Complex properties such as dissociation fraction, ionization fraction, and relative concentration of all species can be written in terms of these two independent parameters. The governing equations for LTE are briefly summarized.

2.3.1 Boltzmann distribution

The population distribution of a gas follows Boltzmann distribution in equilibrium:

$$\frac{n_i}{n_{total}} = \frac{g_i\, exp(-E_i/kT_{pop})}{Q_t} \tag{2.45}$$

where n_i is the number of density of state i, n_{total} is the total number density of the gas, g_i is the degeneracy of state i, E_i is the energy level of state i, k is the Boltzmann constant, T_{pop} is the population temperature, and Q_t is the total partition function. The Born-Oppenheimer approximation states the various energy modes are independent, and the total partition function becomes a multiplication of the individual partition functions.

$$Q_t = Q_{tr}Q_{int} \tag{2.46}$$

$$Q_{tr} = V\left(\frac{2\pi mkT}{h^3}\right)^{3/2} = \frac{V}{\Lambda^3} \tag{2.47}$$

where Λ is called the thermal de Broglie length.

For atoms, the partition function of internal modes is straight forward:

$$Q_{int} = Q_{el}Q_{nucl} \tag{2.48}$$

where Q_{el} accounts for the electronic excitation states, and Q_{nucl} nuclear spin states.

The partition function Q_{el} is defined as:

$$Q_{el} = \sum_{i}^{\infty} g_i\, exp(-E_i/kT) \tag{2.49}$$

Summation to ∞ diverges for electronic states mathematically, however generally the summation is carried up only to the energy level just below the ionization energy [40] and the partition function becomes finite.

2.3.2 Dissociation

The dissociation of diatomic molecules can be formulated with kinetic theory. At an elevated temperature, N_2 and O_2 are dissociated into neutral atoms. Law of mass action can be used to formulate dissociation of diatomic molecule AA:

$$AA \rightleftharpoons A + A$$

$$\frac{N^{AA}}{N^A N^A} = \frac{Q^{AA}}{Q^A Q^A} exp(E_D/kT) \tag{2.50}$$

where N^{AA} is the number of AA molecules, N^A is the number of A atoms, Q^{AA} is the partition function of AA, Q^A is the partition function of A, and E_D is the dissociation energy of AA.

For oxygen molecules, the dissociation energy is only 5.12 eV, and above 5,000 K (which is about 0.12 % of characteristic temperature of dissociation), most of the oxygen molecules are dissociated. On the other hand, due to larger dissociation energy of 9.76 eV, nitrogen molecules start dissociating around 5,000 K. Therefore, over the temperature of 5,000 K, molecular oxygen is well approximated as 100 % dissociated. However the dissociation of nitrogen molecule must be considered as a function of temperature up to 9,000 K.

2.3.3 Ionization

For simplicity, the plasma is assumed singly ionized, which is the case for the most air plasmas. Similar to the dissociation, the ionization of an atom in equilibrium is described by law of mass action, known as the Saha equation:

$$A \rightleftharpoons A^+ + e$$

$$\frac{N^A}{N^{A^+}N^e} = \frac{Q^A}{Q^{A^+}Q^e} e^{E_I/kT} \tag{2.51}$$

where N^z is the number density of neutral particles, N^e is the number density of electrons, Q's are the partition functions, and E_I is the ionization energy.

In high temperature air plasmas, five dominant neutral species are N_2, N, O_2, O, and NO. O and N have high ionization energies of 13.6 eV and 14.5 eV respectively. Also O_2 and N_2 have high ionization energies of 15.6 eV and 12.1 eV. NO has the lowest ionization energy of 9.26 eV, and the approximation that only NO is ionized in the flow, is valid for T $\leq$ 8,000 K.

2.3.4 Transport properties

Transport properties and fluxes may become important in non-uniform plasmas. Gradients in properties, such as temperature, concentration, electric potential, or velocity, drive diffusion. Transport coefficients, which are directly related with effective collisional areas, are very hard to estimate. Boulos [47], tabulated important quantities such as thermal conductivity, viscosity, electric conductivity, specific heat, enthalpy, and density. For T < 12,000K, the plasma may be considered optically thin, and the mean free path length of a photon is much smaller than the arc radius. The temperature is estimated around 7,500 K for the NASA Ames IHF generated plasmas, and they are as optically thin both in the heater and in the test cabin.

The turbulent boundary layer thickness in the heater was estimated with the properties by Boulos. The boundary layer is thin approximately 4 % of the path length and the absorption is stronger in the core of the flow. This makes the boundary layer negligible for the absorption diagnostics [49, 50, 51].

2.3.5 Equation of state

Plasmas are overall charge neutral. However within the Debye length, charge neutrality is not satisfied and long range Coulomb forces must be added to the ideal gas law. Charge unbalance causes repulsive forces, with a resulting decrease in pressure

[47], and with the Debye model, the modified equation of state for plasmas is given [48]:

$$P = nkT - \frac{kT}{24\pi\lambda_D^3} \tag{2.52}$$

with

$$\lambda_D = \left(\frac{\epsilon_0 kT}{e^2 \Sigma_i Z_i^2 n_i}\right)^{1/2} \tag{2.53}$$

where ϵ_0 is the vacuum permittivity, n_i is the number density of ions, and Z_i is the number of ionic charges of species i.

For the NASA arcjet heater, $n_e \sim n_i \sim 10^{18}\ cm{-}3$, and the plasma is only weakly ionized. For the singly ionized plasma, $n \sim 10^{24} \gg \frac{1}{24\pi\lambda_D{}^3} \sim 10^{19}$, and thus $P \approx nkT$.

2.3.6 Composition of the arcjet plasma

Air is a mixture, and coupled equations of each species of law of mass action for dissociation and law of mass action for ionization must be solved to get the composition at a specific condition. For calculations, modified version of the Chemkin code was used [53, 54]. Laux [55] extended the thermodynamic database for the Chemkin database from 5,000 K up to 10,000 K by fitting the thermodynamic functions of Liu [53, 54]. This software solves for species of N_2, N, O_2, O, NO,N_2^+, N^+, O_2^+, O^+, NO^+, and e.

Fig.2.7 shows that over the temperature range of 4,000 to 10,000 K, with the pressure range of 2 to 8 atm, the most dominant species are N_2, N, and O. The mole fraction of O is nearly constant, because the dissociation energy of O_2 is only 5.12 eV and most O_2 is dissociated above 5,000 K. N_2 is dissociated at higher temperature. The dissociation energy of N_2 is 9.76 eV: from 5,000 K, it starts dissociating, and at 9,000 K most of the molecular nitrogen is dissociated. NO also has a relatively low dissociation energy of 6.49 eV, and easily dissociated. The ionization energy of NO is only 9.26 eV (N_2 at 15.58 eV and O_2 at 12.07 eV), and a small amount of NO can contribute significantly to the electron density.

It's also important to estimate the degree of ionization of an atomic species to estimate total species concentration in a plasma. For nitrogen, argon, and oxygen, the ionization energies are 14.5, 13.6, and 15.7 eV respectively. In the temperature

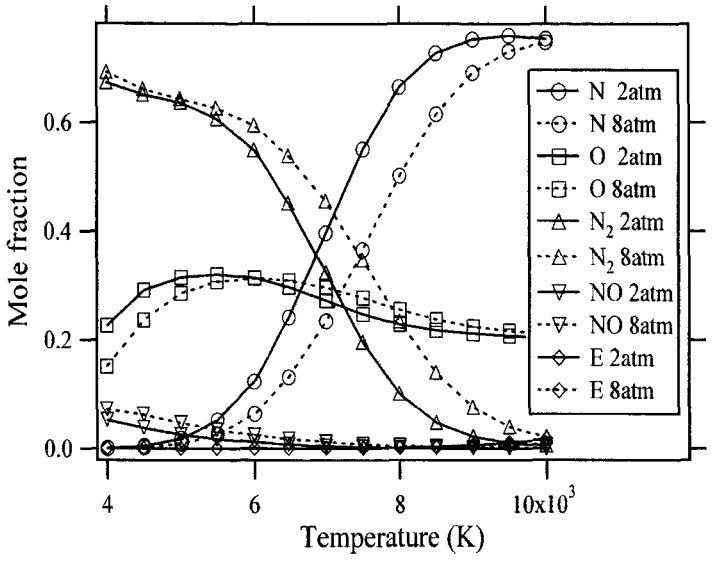

Figure 2.7: Simulation of air mole fraction with Chemkin code

range of our interest, the degree of ionization for nitrogen, oxygen, and argon are all less than 0.1 % and can be neglected in number density calculations. Below 10,000 K, the ion density is low and as the plasma is charge neutral, the electron density is low.

Chemkin does not support metal atoms such as Cu or K. For metals, the ionization energies are much lower: 7.72 eV for Cu, and 4.43 eV for K. Because Chemkin supports only air simulation, the ionization of Cu or K must be calculated separately. More than half of copper is expected to be ionized in the heater, and more than 99 % of potassium is expected to be ionized in the heater. Accurate estimation of ionization of Cu is critical to estimate the total copper concentration in the flow.

In the heater analysis, when calculating the degree of ionization of Cu at a given temperature, the electron number density is calculated with Chemkin simulation code assuming equilibrium.

The degree of ionization of potassium in the test room is hard to estimate because the expanded plasma is non-equilibrium, and the electronic temperature is quite different from the kinetic temperature. The degree of ionization of potassium doesn't have to be accurate, as long as enough potassium absorption is detected in the test

room. However to estimate the amount of potassium to seed in the flow, a rough estimation is required. If too much potassium is added in the plasma, then the plasma properties, such as electric conductivity, may be changed.

Chapter 3

Sensor Design

There are two quite different regions of interest: the arc heater and the test cabin. These two regions have different temperature, pressure, and gas composition. The heater can be considered as a plenum for the arcjet flow. In the heater, the temperature is expected to be 6,000 - 8,000 K, and pressure ranges from 2 to 8 atm. Pressure in the heater is well monitored with pressure transducers attached on the wall, assuming the pressure difference between core flow and boundary layer is negligible. At such a high temperature, a significant fraction of N_2 and O_2 of the test gas or air, is dissociated into N and O. The temperature in the test cabin is estimated 500 - 1,500 K, which is much lower than that in the heater, and the pressure is around 0.008 atm (6 Torr). The velocity in the test cabin (post expansion) is hypersonic and at least 10 times larger than that in the heater, where the flow is subsonic.

Before the work reported in this thesis, there were no diagnostics for time-resolved heater temperature measurements. In the arc heater, the dominant species are N_2, N, and O. The electron and ion density are less than 0.1 % for the range of interest. Atomic species N and O have significantly stronger absorption than N_2 and atoms are attractive absorption sensor targets. Details of the sensor design will be described for both N and O.

Several different temperatures will be defined: translational temperature, population temperature, and excitation temperature. The translational temperature can be deduced from the Doppler width of the lineshape. The population temperature can

be calculated from the ratio of population in an excited state to that of the ground state. Similarly the excitation temperature is defined with the ratio between two different excited states. In equilibrium, these temperatures are the same. In this work, different temperatures are measured and compared to determine the best strategy for the heater temperature measurements.

In this chapter, the sensor design of O, N, Ar, Cu, and K will be described. Then, sensor operation is verified with a microwave plasma in a gas flow. Design of coupling optics to propagate light in and out of the arcjet will then be described.

3.1 Line selection

N and O atoms have an excitation energy in the first excited state nearly 10 eV above the ground state, so that a deep ultra violet light source is required to excite the ground state of these atomic species. Diode lasers are not commonly available for wavelengths shorter than 400 nm and thus cannot access ground state atomic transitions. In this work, NIR lasers were employed to detect exited states or metastable states of the atomic species. The transitions employed in this work is tabulated in Table 3.1 [52, 59, 60, 62, 63].

Table 3.1: Fundamental spectroscopic data for selected atomic transitions

	N	N	O	Cu	Ar	Ar	K
Wavelength (nm)	824.2	856.8	777.2	793.3	772.38	772.42	769.9
A ($\times 10^6$, sec^{-1})	13.6	4.92	36.9	22.5	5.18	11.7	38.2
f	0.0924	0.108	0.468	0.17	0.0278	0.314	0.34
g_i^*	4	4	7	2	3	1	2
g_j^*	6	2	5	2	5	3	2
E_i^* (cm^{-1})	95493	97805	86631	43137	106087	107496	12985
E_j^* (cm^{-1})	83364	86137	73768	30535	93143	94553	0

i indicates upper state, and j indicates lower state

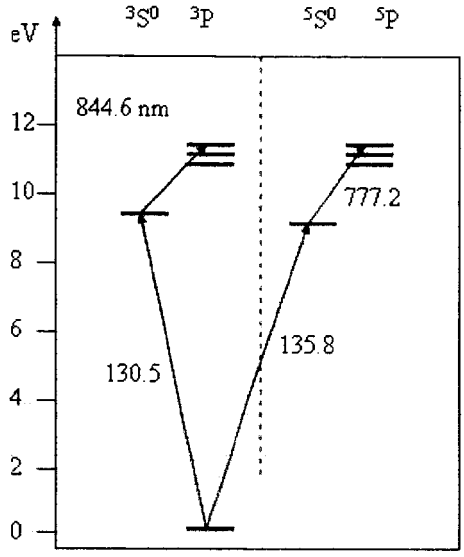

Figure 3.1: The energy diagram of atomic oxygen. The metastable state has the energy level of 9.15 eV

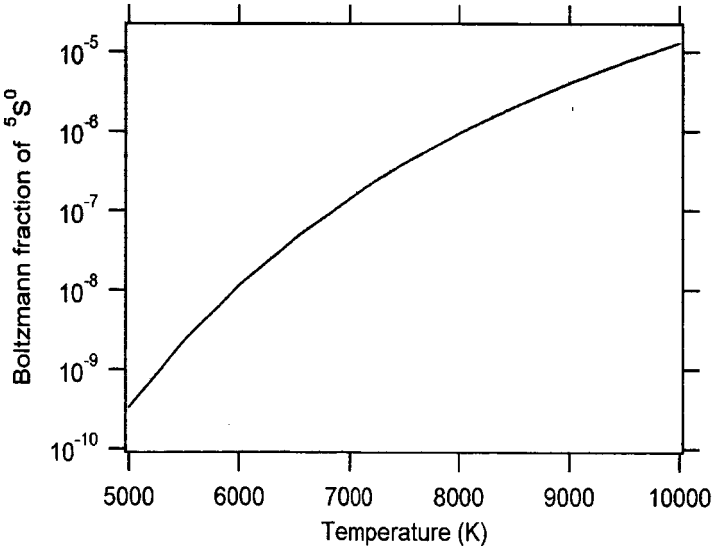

Figure 3.2: The Boltzmann fraction of the metastable state over the temperature range of 4,000 to 10,000 K and the pressure range of 2 to 8 atm

3.1.1 O sensor design

An energy diagram of atomic oxygen is shown in Fig.3.1. The linecenter and Einstein's A coefficient and the oscillator strength f can be obtained from the NIST database [52]. The ground state can only be accessed by vacuum ultra violet (VUV), for example 97.6, 98.8, 130.2, 130.4, 130.6, or 135.9 nm, where currently no conventional laser source is available. However there are three transitions available to monitor the relatively low-energy metastable state $^5S_2^0$ to the excited $^5P_{J'}$ states using light in the near infrared at 777.5, 777.4, and 777.2 nm respectively. These lines have been studied extensively with diode lasers [56, 9, 57, 58, 19]. The fraction of population of O atoms in the $^5S^0$, which absorbs light near 777.2 nm, varies strongly with temperature in the range expected in the arc heater as seen in Fig.3.2. Thus measurements of absorbance of $^5S^0$ state can be used to determine temperature if the plasma is in equilibrium.

The lineshape of O is not complicated by multiple abundant isotopes or by hyperfine structure. The natural abundance of ^{16}O is 99.76%, and therefore the isotope shifts of ^{17}O or ^{18}O can be ignored. ^{16}O has a nuclear spin of $I = 0$, and hence there's no hyperfine structure of ^{16}O from coupling of the nuclear spin and the electron angular momentum.

We chose the transition at 772.2 nm to monitor the temperature in the heater. A VCSEL (Avalon Photonics) was installed at a fixed temperature of 15.0 C with the injection current of 5.64 mA, and a function generator modulated injection current of the laser diode to scan the wavelength over 6.0 cm^{-1}.

3.1.2 N sensor design

N has VUV transitions from the ground state, and no conventional light source is available to excite N in the ground state. The metastable state of N is at 2.38 eV, and the transition from the metastable state is also VUV. The excited states ,$^4P_{5/2}$ at 10.3 eV and $^2P_{1/2}$ at 10.7 eV were chosen instead to monitor atomic nitrogen in the heater. The energy diagram and the Boltzmann fraction of the two excited states are given in Fig.3.3 and in Fig.3.4. The 824.2 nm transition was first used due to stronger absorption, however, the 856.8 nm transition was used for later work. Again

the temperature dependence of the population in these excited states makes them attractive temperature sensors. A FP laser at 824.2 nm was initially used, however for wider tuning range and narrower spectral width, a VCSEL replaced the FP laser to scan 4.5 cm^{-1} over 826.8 nm.

The detailed lineshape of N is complex. ^{14}N comprises 99.63 % of the total nitrogen and the isotope shift can be ignored, however the nuclear spin I is 1 and there is hyperfine structure. Fortunately, the splittings between hyperfine lines are small [60, 61] enough in the heater, where the lineshape is significantly broadened and the hyperfine structure can be ignored in data analysis.

3.1.3 Ar sensor design

Ar gas is introduced in the heater. In the test cabin, it is desired to monitor metastable states and to set upper limits on the number density of the states. The energy level diagrams are shown in Fig.3.5 and in Fig.3.6 [59].

Among the $1s - 2p$ transitions, the transitions at 772.38 and 772.42 nm are studied because the spectral difference between them is only 0.04 nm or 0.67 cm^{-1} and the lower states of the transitions are different metastable states. Two transitions from $4s'[1/2]$ and $4s'[3/2]$ are close enough that a single VCSEL laser can scan both transitions simultaneously.

3.1.4 Cu sensor design

A portion of the copper energy level diagram is shown in Fig.3.7. The temperature dependence of the $^2P^0_{1/2}$ population is also shown in Fig.3.8.

The energy level of $^2P^0_{1/2}$ and the ionization energy of Cu are low. Thus the Boltzmann fraction and ionization fraction are significant. Two transitions at 793.3 and 809.3 nm were considered, and due to its simpler lineshape, the 793.3 nm transition was chosen. It is notable that the first excited states are at 3.79 and 3.82 eV, and the energy levels of the metastable states of copper are only 1.39 and 1.64 eV. A UV light source at 324.8 or 327.4 nm can access to the ground state, and green light source at 510.6 or 570.0 nm can excite the Cu atoms in metastable states. If a laser

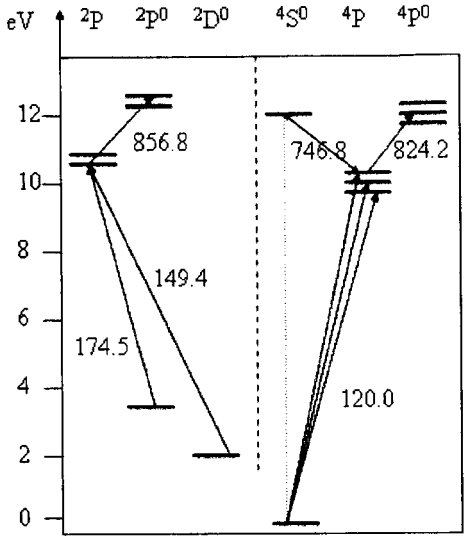

Figure 3.3: The energy diagram of atomic nitrogen

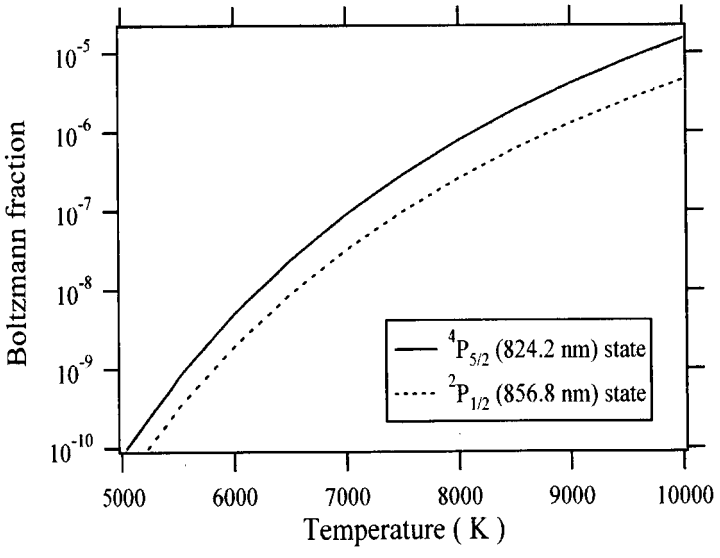

Figure 3.4: The Boltzmann fraction of the two excited states over the temperature range of 5,000 to 10,000 K and the pressure range of 2 to 8 atm

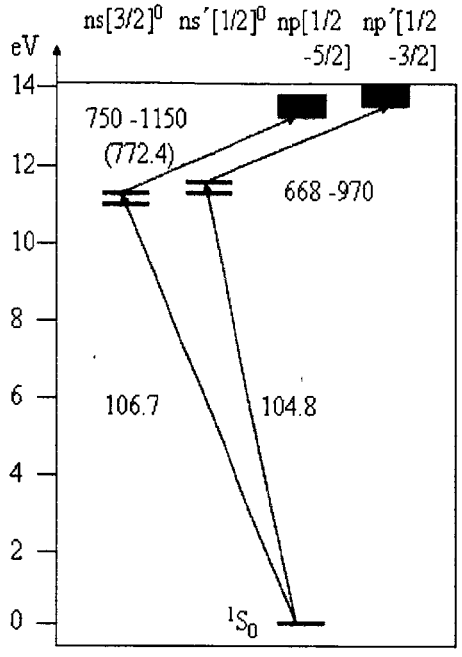

Figure 3.5: The energy diagram of argon

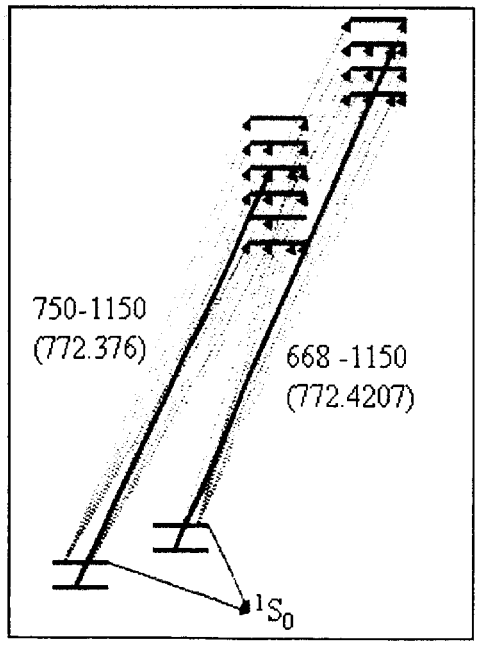

Figure 3.6: The detailed energy diagram between 1s-2p

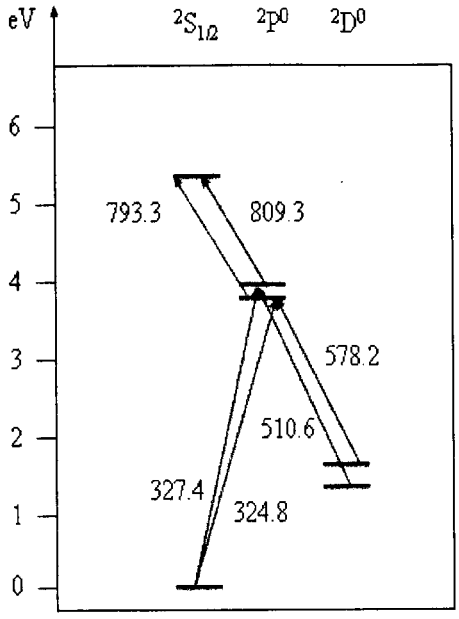

Figure 3.7: The energy diagram of copper

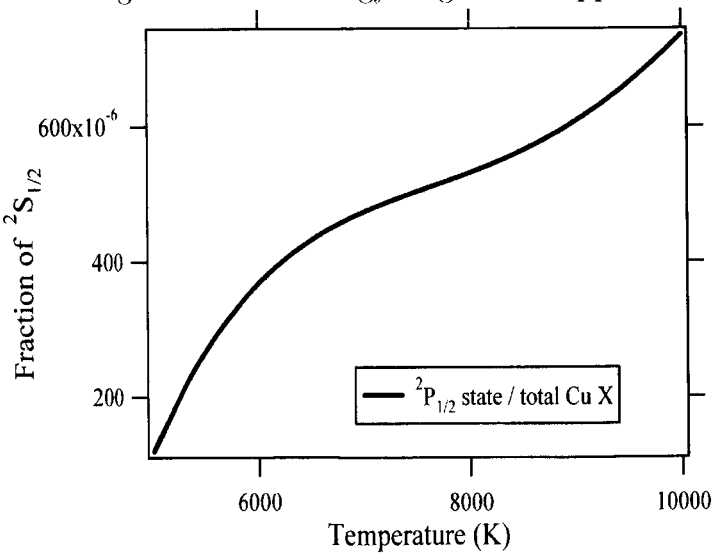

Figure 3.8: The fraction of $^2P^0_{1/2}$ of total copper species including ions

were available at these wavelengths, the estimated detectivity would improve by one or two orders of magnitude.

However, in this work, the convenience of using NIR light source lead to the selection of the transition from the first excited state $^2P^0_{1/2}$ to another excited state $^2S^0_{1/2}$ at 793.3 nm.

3.1.5 K sensor design

Previous research by Wehe [62] shows that metals, especially alkali metals such as sodium, potassium, or cesium, have transitions with strong linestrengths and can be used as a tracer in a hypervelocity flow. For alkali metals, the transition from the ground state to the first excited state is in NIR or visible range, where diode lasers are available. The potassium energy diagram and ionization fraction are shown in Fig.3.9 and in Fig.3.10.

The degree of ionization over the temperature range of 500 K to 3,000 K with an electron density of 10^9 cm^{-3} to 10^{11} cm^{-3} indicates a small degree of ionization at 1,500 K (0.03 %); however at 3,000 K, almost all potassium is ionized (degree of ionization of 99.5 %). The potassium ions recombine in the nozzle, and significant atomic potassium can exist in the test cabin. If the electronic temperature is 1,500 K at a pressure of 0.8 kPa (6 Torr), 2 ppb concentration of potassium can be detected over 40 cm path length in the test cabin with 0.1 % absorption.

Wehe chose K at 769.9 nm for its large linestrength, narrow and relatively simple hyperfine structure, ease of seeding, and the well-known spectroscopic parameters [63, 64]. In this work, the same line was selected to monitor the post-expansion flow condition. Seeding potassium was done by painting salts such as KCl or KOH inside the heater wall. By extracting the Doppler width from the absorption lineshape, the translational temperature of potassium was obtained.

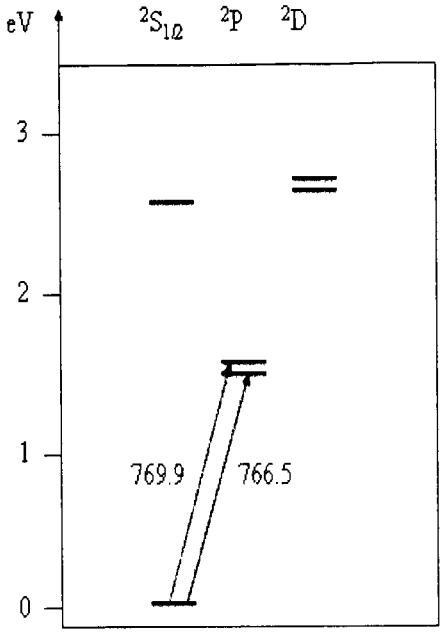

Figure 3.9: The energy diagram of potassium

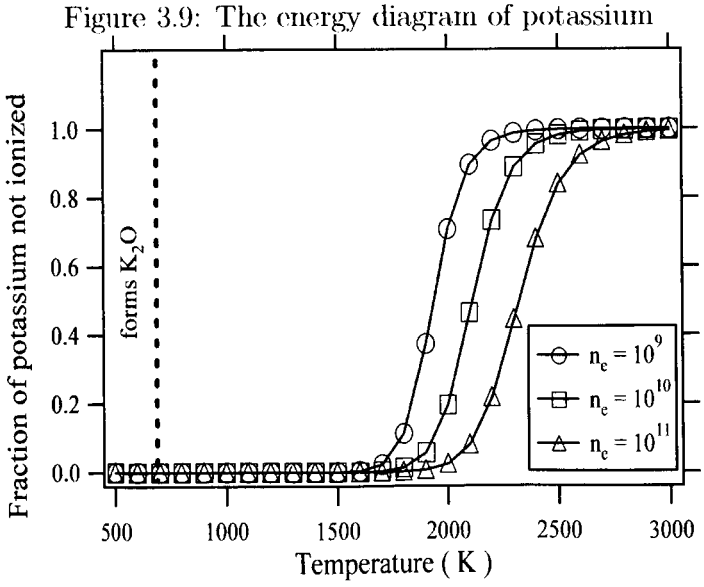

Figure 3.10: The fraction of potassium ionized at various electron number densities

3.2 Optical engineering

The environment of the IHF and the requirements for safety produce many technical challenges. High-voltage and high-current electrodes require electrical and physical isolation of the test cabin and the heater. High-pressure in the heater, and low-pressure in the test cabin require careful sealing. The IHF offers a special challenge due to deflection of the beam and steering by the hypersonic flow or the high-temperature high-pressure plasma. Thus careful design of optical components is required to maintain alignment. The diode lasers and detection systems are in a laser room located roughly 3 meters from the IHF. The heater and test cabin setups have separate design equipment and are considered separately. Optical engineering for laser delivery systems and detection systems of the heater and of the test cabin are presented below.

3.2.1 Diode lasers and detectors

An isolated laser room next to the IHF facility accommodates diode lasers and detectors. Singlemode optical fibers deliver laser beams to the heater and to the test cabin, and multimode optical fibers deliver the collected transmitted laser beams from the heater and from the test cabin back to the laser room for detection.

Two of three diode lasers, N at 856.8 nm, O at 777.2 nm, and Cu at 793.3 nm, were mixed with a 2x2 fiber coupler. One output connects the singlemode fiber to the heater, and the other output connects light to the 2 GHz solid etalon (0.0667 cm^{-1}) used to measure the relative tuning range.

A large catch lens and a large core multimode fiber delivers emission from the plasma. Diffraction from a 2.54 cm × 2.54 cm (1″× 1″), 1200 groove/inch grating was used to separate the return signal from the two laser beams of different wavelengths. To increase signal-to-background ratio, narrow bandpass filters were used. 10 nm bandwidth optical filters were installed in front of a silicon detectors.

Lasers were scanned in wavelength over 5 cm^{-1} at 100 Hz. This wide tuning range is required to cover Zeeman splitting and broadening mechanisms in the heater and in the test cabin.

A Fabry-Perot type laser requires an optical isolator to prevent back-reflection, which can cause unstable operation and modehops. Also, unlike VCSELs, the FP laser used in this work has a high optical power of 20 mW, and at this power level, saturation can be a significant problem. Light from a FP laser is linearly polarized, thus we used a polarizer to attenuate optical power to 0.2 mW before coupling light to the fiber.

A National Instruments data acquisition card was used to record data in a computer. The computer card is 16 bit accuracy; the sampling rate is 100 ks/s, and can be extended to 16 channels. Another fast computer scope with a sampling rate of 4 Ms/s was used to monitor hypervelocity flow in the test cabin.

3.2.2 Beam delivery design in the heater

The test cabin and the heater must be isolated electrically; therefore no metal line is allowed to cross the isolating walls. In our experiments, optical fiber was used for light delivery and signal collection. However this fiber-coupled system must be designed carefully to account for the physical properties of the optical fibers and the optics. An optical fiber is a simple waveguide, and the refractive index profile for a given fiber geometry determines the number of modes that can be accommodated at a given wavelength. Pollak [65] and Snyder [66] explain this in detail.

Each mode of monochromatic light travels at a different effective speed because of the different physical distribution in the fiber. The fundamental mode travels near the core of the fiber, where the refractive index is maximum, and therefore at the lowest speed. The higher order modes travel near the cladding of the fiber, where the refractive index is minimum, and therefore at the higher speed. The difference in speed between modes cause interference between modes, called modal dispersion. For wavelength scanned sensor applications, the interference between modes can limit the sensitivity and must be avoided.

By reducing the diameter of the fiber, only one mode at a given wavelength can be supported by the fiber, and this type of fiber is called singlemode fiber. To deliver laser beams to the pitching optics, singlemode fibers are employed to prevent the

modal dispersion at the cost of coupling efficiency and alignment tolerance.

The numerical aperture in optical fiber is defined as $\sqrt{n_{core}^2 - n_{cladding}^2}$, and describes the solid angle to couple light into a fiber. Multimode fibers have larger numerical aperture ranging from 0.2 to 0.35 with core diameter of 50 to 1000 μm, while single mode fibers have a numerical aperture of 0.11 with core diameter of 4.5 μm at 780 nm. Due to the smaller size and numerical index of singlemode fibers, the laser-to-fiber coupling efficiency and alignment tolerance are poor compared with multimode fibers. For an edge emitting laser, only around 15 % of the optical power is usually coupled to a singlemode fiber, while 70 % coupling can be easily done with a multimode fiber. With the good quality of the VCSELs, only 25 to 30 % coupling efficiency to a singlemode fiber was achieved.

Optical alignment in IHF is challenging: beamsteering due to fast flow in the heater and cabin is significant, and the deformation of IHF test cabin and heater by pressure change and thermal expansion during operation is large. To overcome this problem, a large collecting lens and a multimode fiber catching system is used to collect the transmitted laser beam and deliver the signal to the detector in the laser lab located a few meters far from the IHF.

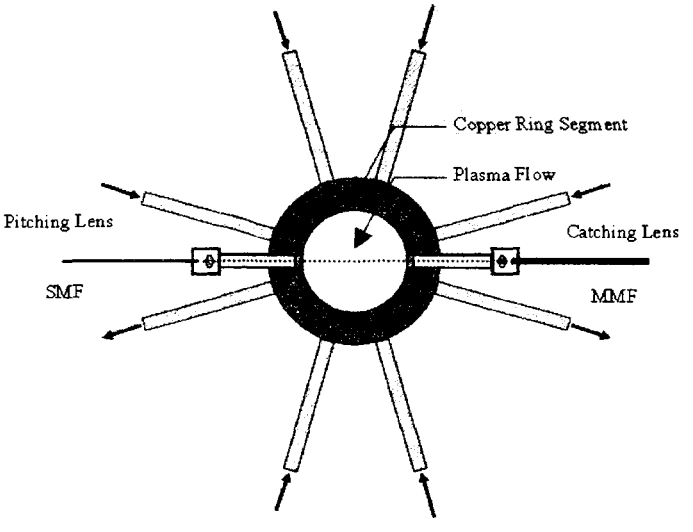

Figure 3.11: Optical components in the heater

Schematics of the pitching and catching system is shown in Fig.(3.11). There are eight high pressure water cooling lines for each ring segment, and the heater is composed of tens of ring segments. It is almost impossible to deliver laser beams in free space into and out of the heater. Very limited space requires special mechanical design to direct laser light through two small 4.76 mm (3/16″) holes, while sealing 1 - 7 atm pressure difference. Anti-reflection coated sapphire windows and silicon O-rings, are combined with parts fabricated to mate to the ring segment.

First, the angular and lateral alignment tolerance for the optics was tested in a laboratory experiment. As shown in Fig.3.12 and in Fig.3.13, the lens-to-fiber coupling efficiency increases as core diameter increases. The angular tolerance is strongly dependent on the core diameter of a fiber, because a small change with incident angle causes the position of a beam spot to move on the end surface of a fiber. Fibers with a core diameter larger than 200 μm can tolerate 0.2 degree angular misalignment. However, the lateral tolerance depends on the size of clear aperture. The catching lens has a clear aperture of 4 mm, and the lateral tolerance (-3 dB) of multimode fibers is roughly 3 mm in diameter. The numerical aperture of a lens, which is defined by the ratio of the clear aperture and focal length of a lens, is usually smaller than the numerical aperture of the fiber. Therefore in many cases, the clear aperture of a lens determines lateral tolerance.

The clear aperture of the collection lens, and the core diameter of the collection optical fiber are the key parameters to design the catching system. The clear aperture of the lens determines lateral tolerance, and the fiber core diameter and corresponding numerical aperture of the fiber determine angular tolerance. Design process for other optical components using Gaussian optics and modal noise is presented in Appendix D.

On the pitching side, a 30 m singlemode fiber (core/cladding of 4.5/125 μm, 8 degree wedged end surface, and 3 mm diameter jacketed) was used. The light is collimated with an anti-reflection coated aspheric lens with a focal length of 6 mm. An aspheric lens minimizes a spherical aberration, and therefore most of the light incident on the lens is focused on the same spot, and lateral tolerance of the beam alignment with an aspheric lens is improved compared to a spherical lens. To minimize

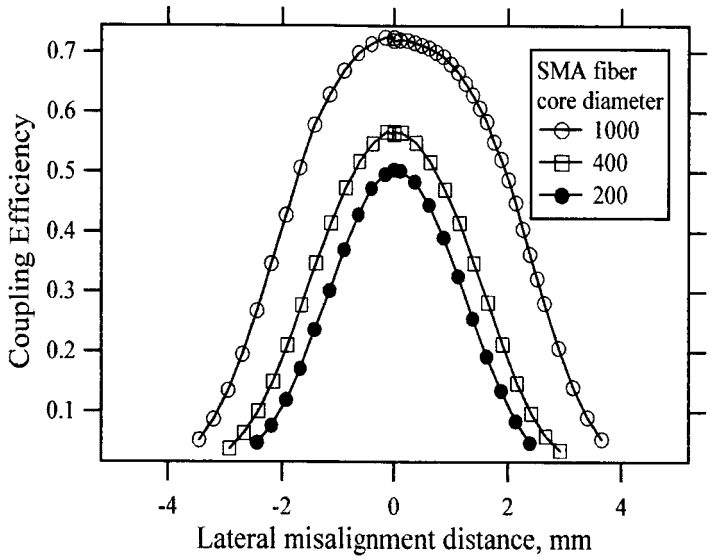

Figure 3.12: The lateral tolerance of lenses and fibers

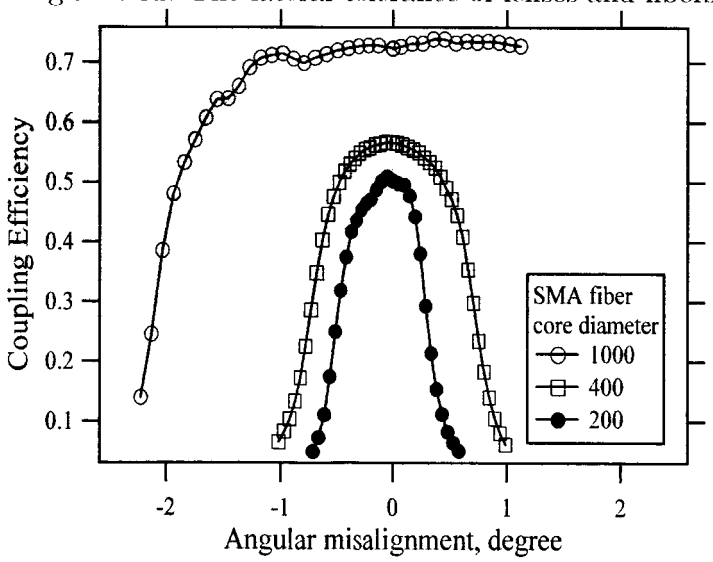

Figure 3.13: The angular tolerance of lenses and fibers

interference from the lens surfaces, anti-reflection coated lens was used. The beam radius is estimated to be 0.6 mm ($\approx$ numerical aperture $\times$ focal length).

For the catching side, a 30 m multimode fiber (core/cladding of 400/430 μm) was used. The catching lens was an anti-reflection coated achromatic lens of 9 mm clear diameter, with a focal length of 20 mm. An aspheric lens was preferred to minimize spherical aberration for maximum lateral tolerance of the beam alignment, however a large clear aperture was only available with achromatic lenses. The combination of large diameter multimode fiber and catching lens has large tolerances from misalignment and beam steering.

3.2.3 Beam delivery design in the test cabin

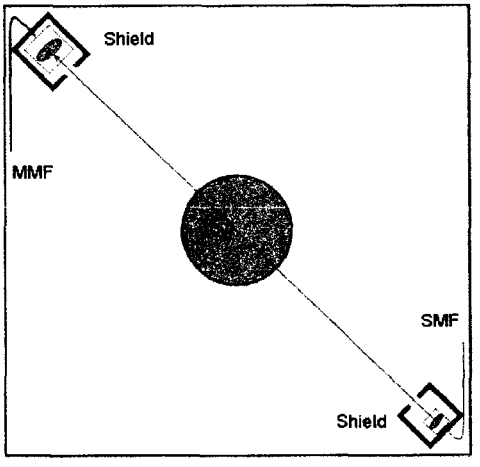

Figure 3.14: Optical components in the test cabin

The difficulty of beam delivery in the test cabin is different from that in the heater. When the test cabin is evacuated the chamber mechanically distorts. This deflection due to pressure drop during the operation changes the direction and the lateral position of the beam. The pitching and catching optics are located at the upper and lower corner diagonally, and the distance is roughly 3 m. A slight angular

change moves beam spot at the catching optics significantly. Even 0.1 degree changes of the pitching optics cause roughly 5 mm lateral misalignment. At low pressure ($\sim$ 0.01 atm), we estimated lateral displacement of 5 mm compared with the beam spot position at 1 atm. The laser beam was aligned at 1 atm considering 5 mm travel at low pressure.

The laser beam diameters and the profile in the test cabin were also measured to obtain parameters required to calculate the saturation intensities. The beam size was measured in the center of the nozzle, and the beam radius was roughly 1.1 to 1.2 mm as determined by sliding a knife edge, differentiating the measured power, and fitting the data to Gaussian. This indicates the beam is the fundamental mode from the fiber, and provides the data needed to estimate the saturation effect in the test cabin. For this beam diameter, the saturation is negligible.

Optics to minimize beam diameter at the catching optics 3 m distant, were designed. Gaussian beam theory was used to choose a pitching lens of 11 mm focal length, AR coated, aspheric lens. For the catching collimator, the biggest clear aperture lens available, 11 mm clear aperture, 20 mm focal length achromatic lens was used.

3.3 Sensor validation in a laboratory plasma

To test tunable diode laser absorption spectroscopy sensors, a microwave discharge flow tube was employed because it is easy to operate and relatively simple to build. A similar discharge tube with nitrogen gas was used as a reference for nitrogen atom LIF measurements at NASA Ames [21, 22]. By changing the feed stock gas, various atomic species can be generated in the microwave discharge tube. A schematic of the microwave discharge flow is given in Fig.3.17

Microwave discharges are stable, reproducible and relatively quiescent, and have been atomic sources for chemical measurements for decades. The electrons in the microwave discharge absorb electric energy and collide with neutrals and ions. Energy transfer by the collision of an electron with heavy particle is estimated as $\frac{m_e}{(m_h+m_e)}\Delta E$, where m_e is the mass of an electron, m_h is the mass of a heavy particle, and ΔE is

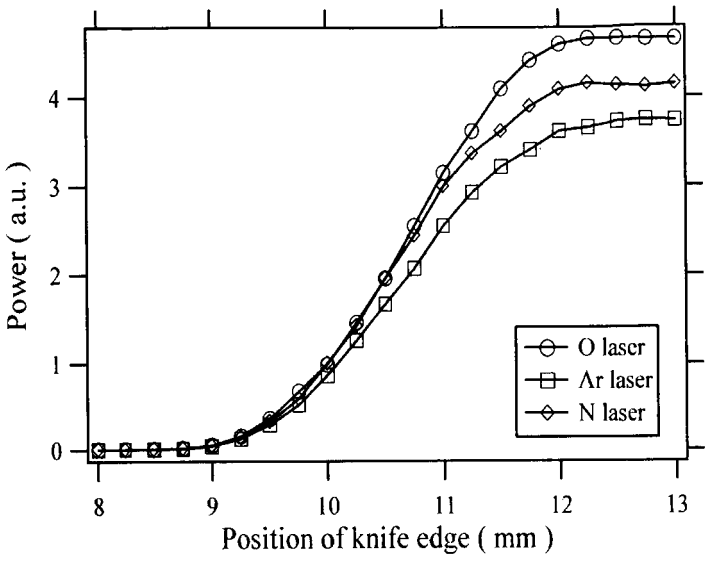

Figure 3.15: Beam radius measurements in IHF test cabin: power vs relative position with a knife edge

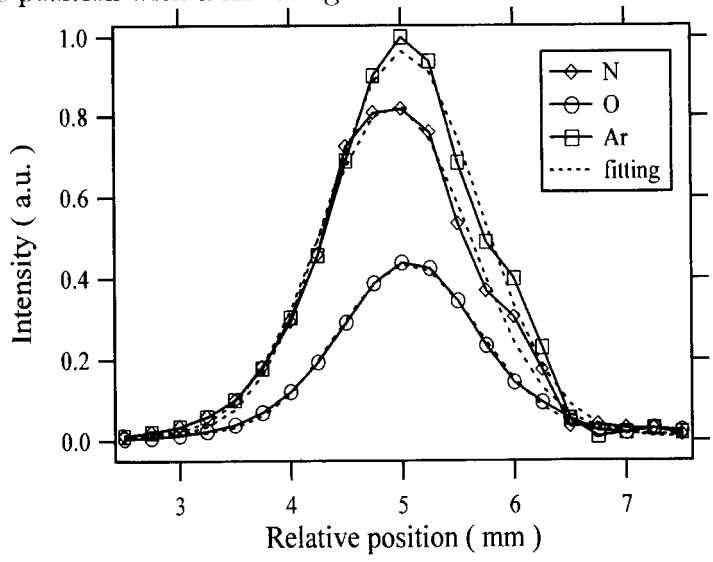

Figure 3.16: Beam radius measurements in IHF test cabin: The spatial derivation of transmitted power vs relative position with Gaussian fitting

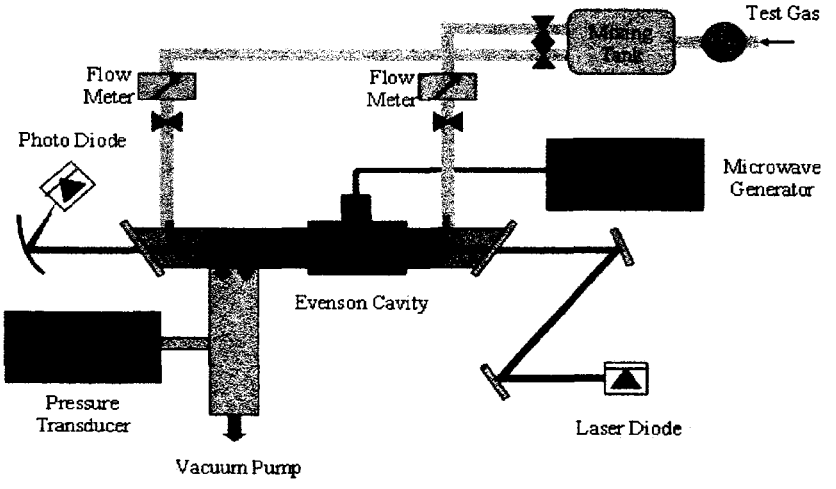

Figure 3.17: The schematics of laboratory microwave discharge tube at Stanford University

the difference of translational energy [47].

At low pressure ($P \leq 1$ kPa), the collision rate is low, and the energy transfer from electrons to heavy particle is not efficient. Therefore the translational temperature of heavy particles may be quite different. This non-equilibrium allows the production of atomic species near room temperature (translational temperature), and experiments with these non-equilibrium plasmas much easier than with thermal equilibrium plasmas.

A microwave generated by Opthos Instruments, Inc. at a frequency of 2.45 GHz delivers power ranging from 0 to 120 W to an Evenson cavity. This cavity can excite static and flowing gases at a pressure range from a few mTorr to several hundred Torr. There are two tuning knobs: a threaded tuning stub on the top and a sliding rod made of ceramic to withstand high temperature. The cap of the cavity can be removed, and this cavity can be installed on an existing gas system. The flow rate to the discharge tube is monitored by Tylan General, Model 360 V flow meters, and the pressure is measured with a MSR, PDR-D-1 pressure gauge. Argon, nitrogen, and oxygen gas are introduced through the flow meters, and a low pressure glow discharge

is maintained around the microwave cavity. The windows, where a laser beam passes through, are glued at Brewster's angle to minimize the reflections.

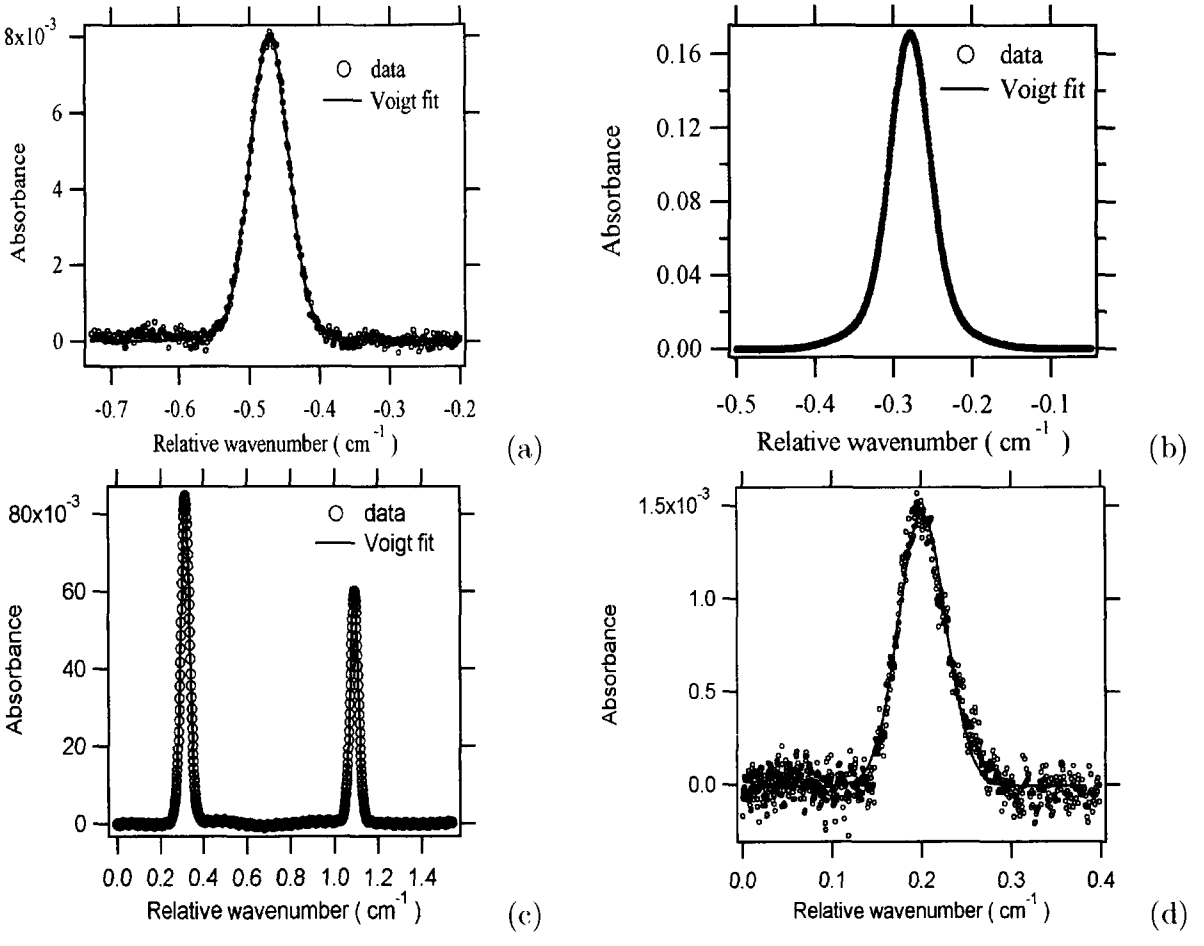

Figure 3.18: Discharge tube absorption measurements of (a) nitrogen at 824.2 nm (b) oxygen at 777.2 nm (c) argon at 772.4 nm and (d) N_2 first positive system at 773.8 nm

Sample results of absorption by nitrogen, oxygen, and argon are presented in Fig.3.18. In the discharge tube measurements, the lineshape is fitted to a Voigt profile, but the pressure was only 0.5 Torr, and the Doppler broadening was the dominant broadening mechanism. The translational temperature ranged from 345 to 1,000 K, depending on pressure, flow rate, and rf-power. The lineshape in the discharge tube should be much narrower than that in the arc heater. In the heater,

the temperature ranges between 6,000 and 8,000 K and the pressure ranges between 2 and 8 atm. The corresponding Doppler width is as much as 5 times wider, and Stark broadening and van der Waals broadening can also be significant. Stark effect and Zeeman splitting must be considered in the heater. Even though the lineshapes in the discharge tube are quite different from the lineshapes in the heater, the line center of each transition was successfully verified with a simple lab-based microwave discharge tube.

Chapter 4

Temperature Measurements in the IHF Heater

Atomic absorption spectroscopy measurements to infer gas temperature in the heater are presented in this chapter. Pressure and temperature are the two fundamental properties of a plasma flow in equilibrium. The pressure in the heater is monitored with pressure transducers on the inner wall of the heater. However, previously the gas temperature has not been measured. In this work, two dominant atomic species of air plasmas, N and O, are monitored with two VCSELs near 856.8 nm and 777.2 nm.

TDL absorption measurements of atomic N or O in the heater can be used to infer temperature in two different ways. First, if the Doppler broadening contribution to the lineshape can be extracted from the measured wavelength scanned absorption, then the translational temperature is readily available. Second, if the gas is in chemical and electronic equilibrium, then the absorption measurement of the population in a specific electronic state of N or O can be combined with the known heater pressure to infer a temperature. In the heater there is a DC magnetic field from the arc current and an AC magnetic field which is used to swirl the arc attachment on the exit nozzle. These fields lead to Zeeman splitting of the absorption transition. The combination of the high-pressure and high-temperature in the heater lead to an absorption feature which is quite difficult to deconvolve to determine a Doppler contribution to the

width. Thus, the chemical temperature determined from the measured N or O number densities are expected to provide a more accurate temperature. However, before discussing the number density measurements, we first discuss the lineshape results.

4.1 N and O absorption lineshapes in the IHF

The absorption lineshape of atomic oxygen near 777.2 nm measured in the arc heater is shown in Fig.4.1. The absorption feature appears as a single transition. However, this feature is actually the blend of the 5 lines of the Zeeman split transition. Because DC and AC magnetic fields are not known, it is very difficult to fit this feature to 5 lines. If we chose to fit the data in Fig.4.1 to a single Voigt lineshape, we obtain a half-width-half-maximum (HWHM) for the Gaussian component of 0.149 cm^{-1}. This corresponds to a translational temperature of 16,240 K, which is much higher than the temperature expected from energy balance considerations. In addition, this single Voigt lineshape fit leads to very large fluctuation in the linewidth consistent with the large AC magnetic field. Fig.4.2 shows a time series of the Gaussian fit widths. The average single Doppler linewidth during 700 sec corresponds to 16,240 K and the fluctuation was 6,690 K. Fig.4.2 illustrates that the average temperature and these fluctuations which would suggest a temperature fluctuations, is not reasonable in the arc heater on the basis of energy balance arguments.

The heater conditions during the temperature measurements are shown in Fig.4.3. The fluctuation of the voltage, current, pressure and mass flow rates are negligible, the arc heater efficiency was 49 % with only a 1.5 % peak-to-peak fluctuation. The heater temperature from the energy balance can be roughly estimated with the air plasma properties at 1 atm [47] using

$$\eta VI = \int_{Troom}^{Theater} \dot{m} c_p(T) dT \tag{4.1}$$

where η is the arc heater efficiency, $\dot{m}$ is the mass flow rate, and T_{room} and T_{heater} is the room temperature and the heater temperature respectively.

Requiring energy balance, a temperature of 6,750 K is predicted at 1 atm. The

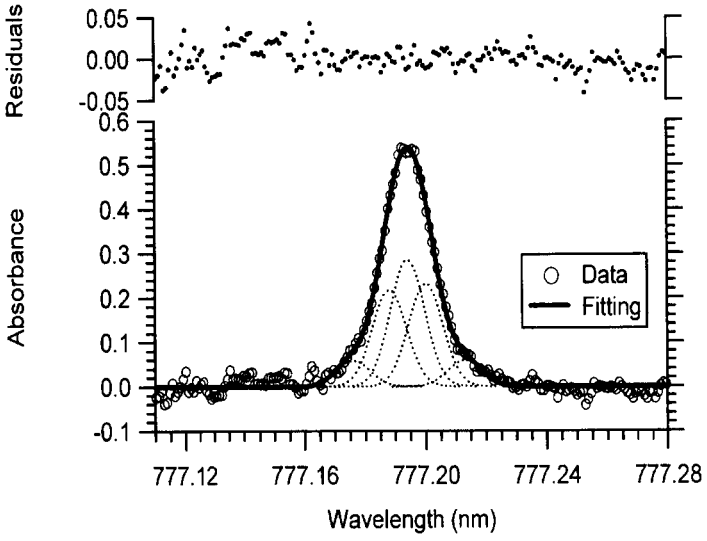

Figure 4.1: Absorbance of O near 777.2 nm

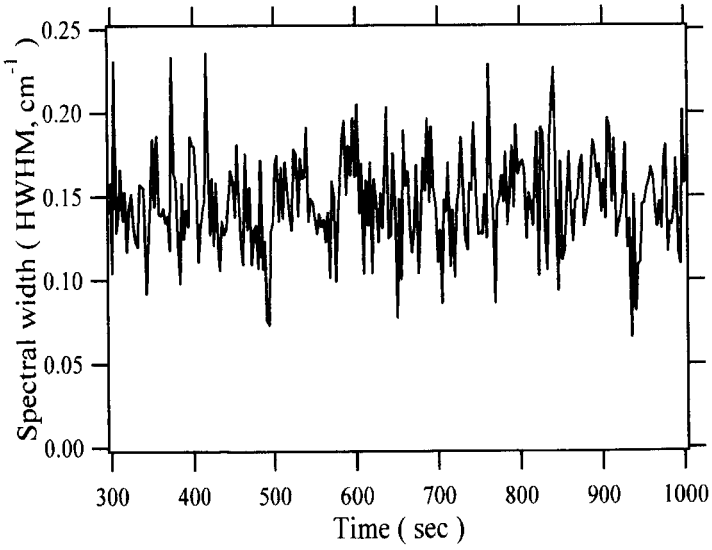

Figure 4.2: Gaussian width of O near 777.2 nm from a single Voigt fit

actual pressure in the heater was 196 kPa, and the specific heat at 196 kPa is different from the specific heat 1 atm. Unfortunately, the specific heat at 196 kPa is not precisely known. The dissociation of molecules in the high temperature plasma at 196 kPa is less than that at 100 kPa, and therefore a larger portion of the input energy contributes to the gas temperature. Also the absorption is stronger in the core and the diode laser sensor is more sensitive to the plasma core, where the temperature is higher, than to the edge of the flow. Thus the temperature at 196 kPa should be slightly higher than 6,750 K estimated here.

If the feature in Fig.4.1 is fit with 5 Zeeman split lines with Voigt lineshapes, the fidelity of the data for these severely blended transitions does not allow a unique fit. The magnetic field strength must be constrained for a reasonable fit.

The lineshape of atomic nitrogen near 856.8 nm measured in the heater is shown in Fig.4.5. A single Voigt fit to the transition of atomic nitrogen near 856.8 nm gives the Gaussian width (HMHM) of 0.159 cm^{-1}. Again, the Gaussian width, which corresponds to the translational temperature of 20,330 K with fluctuation of 6,800 K, is unreasonable. This nitrogen absorption lineshape is the blend of 30 lines resulting from Zeeman splitting of 6 hyperfine lines. However, the combination of Zeeman and hyperfine structure is complex and the magnetic field in the heater is unknown. Just as in the O case, multiple line fitting was not feasible to obtain the translational temperature.

To obtain the gas temperature in the heater, the population temperature was measured in the heater.

4.2 N and O number densities to infer temperature

As shown in the previous chapter, the population temperature can be calculated from the integrated absorbance area. Even though the transition is split into multiple lines by Zeeman splitting, the total area remains constant. The number density of the atomic oxygen metastable state, $^5S_2^0$, can be obtained from the numerical integration

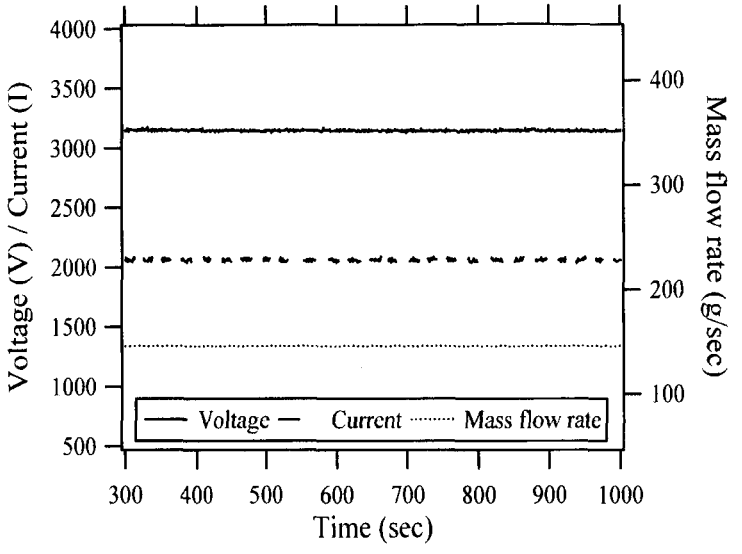

Figure 4.3: The electrode voltage, current, and the mass flow rate air

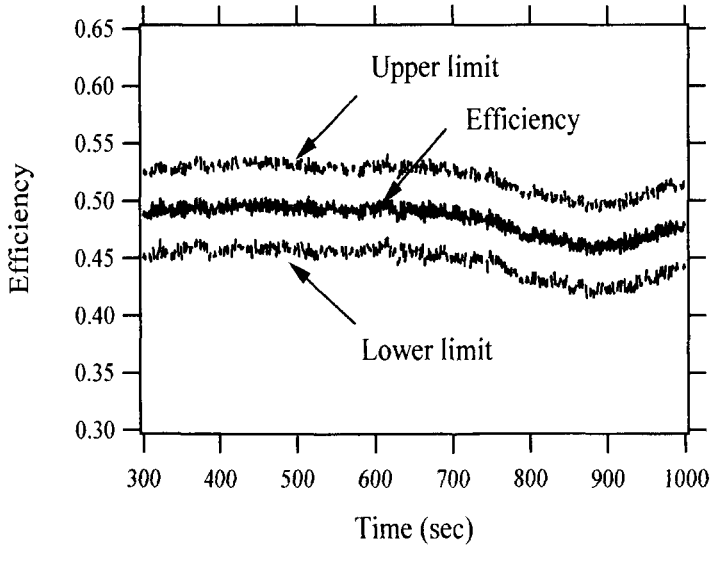

Figure 4.4: The arc heater efficiency measured from the temperature and flow rate of cooling water

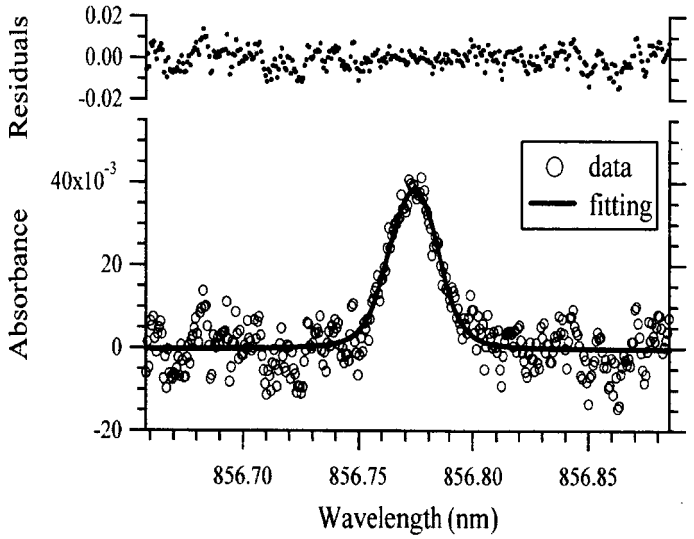

Figure 4.5: Absorbance of N near 856.8 nm

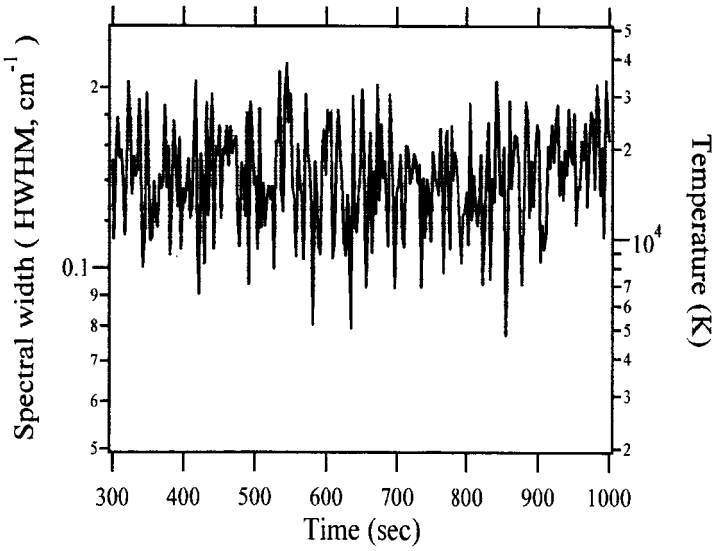

Figure 4.6: Gaussian width of N near 856.8 nm from a single Voigt fit

of the absorbance. From Beer-Lambert's law,

$$Sn_iL = \int ln(\frac{I}{I_0})d\nu \tag{4.2}$$

$$n_i = n_0 B(T) D(T) \tag{4.3}$$

where n_i is the number density of an excited state, n_0 is the number density of the species, and $B(T)$ and $D(T)$ is the Boltzmann fraction and the degree of ionization respectively.

For the data in Fig.4.1, the integrated area of absorbance is 0.178 cm^{-1}, and the corresponding density of $^5S_2^0$ is 3.60 $\times 10^{10}$ cm^{-3}. The optical path length in the heater is the diameter of the electrode ring (11.4 cm) ignoring the thickness of boundary layer. Boundary layer analysis is discussed in appendix. Linestrength S is defined as $\frac{\pi e^2}{m_e c} f$ in unit of $cm^{-1}s^{-1}$, and is 0.0122 for O near 777.2 nm. The degree of dissociation of oxygen in the test gas, air, above 6,000 K is close to 1. With known air composition and measured pressure, the number density of oxygen atom, n_0 is calculated as $\frac{P_{total}}{x}/kT$.

The fraction of the total atomic oxygen in the metastable state was estimated as 1.87 $\times 10^{-7}$, which corresponds to a population temperature of 7,120 K from the Boltzmann fraction shown in Fig.4.7. We believe due to the Zeeman effect and the hyperfine structure, the population temperature is a better indicator than the translational temperature in the IHF heater. During the material test, all operation parameters such as voltage, current, heater pressure, and mass flow rate were kept constant, and the population temperature was constant as expected.

From the integrated area near 856.8 nm of 0.0146 cm^{-1}, the number density of the excited nitrogen was 1.30 $\times 10^{10}$ cm^{-3} with the linestrength of 0.00281 $cm^{-1}s^{-1}$. With the mass flow rate of main air, and assuming equilibrium dissociation, the total atomic nitrogen in the $^7P_{1/2}$ state is 6.31 $\times 10^{-8}$, and yield a population temperature of 6,850 K. More detailed discussion of the gas composition at the elevated temperature and pressure is given in the previous chapter.

The number density of total nitrogen can be larger than that of oxygen by a factor of 4 from the composition of air. However, at the expected temperature, oxygen is

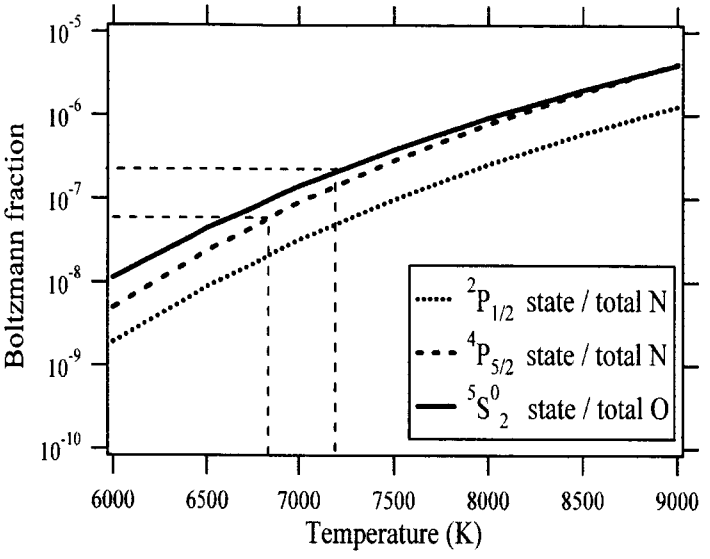

Figure 4.7: Boltzmann fraction of N and O over 6000 to 9000 K at 2 atm

fully dissociated and nitrogen is not. The oscillator strength of the 777.2 nm transition of O is about 4 times larger than that of the 856.8 nm transition of N, and the Boltzmann fraction of O in its lower state is larger than the Boltzmann fraction of N in its lower state at a given temperature by a factor of 4 as in Fig.4.7. The signal-to-noise ratio (SNR) of O was 20, and is 5 times better than the N measurements. For the temperature range between 6,000 to 8,000 K, the equilibrium ionization of N and O is small due to high ionization energy of N and O, and was neglected in the data analysis.

4.3 Simultaneous heater temperature measurements

For a specific run, IHF 147 Run 019, the population temperatures of O and N were simultaneously monitored. The operation conditions of IHF 147 Run 019 are plotted in Fig.4.8. At the beginning, there is a transient period, called the start-up period when argon flow is used to start a discharge in the heater. After the discharge is initiated, a small amount of air is added to the flow, then the mass flow rate of air is increased until the discharge reaches a stable condition, and the voltage, current,

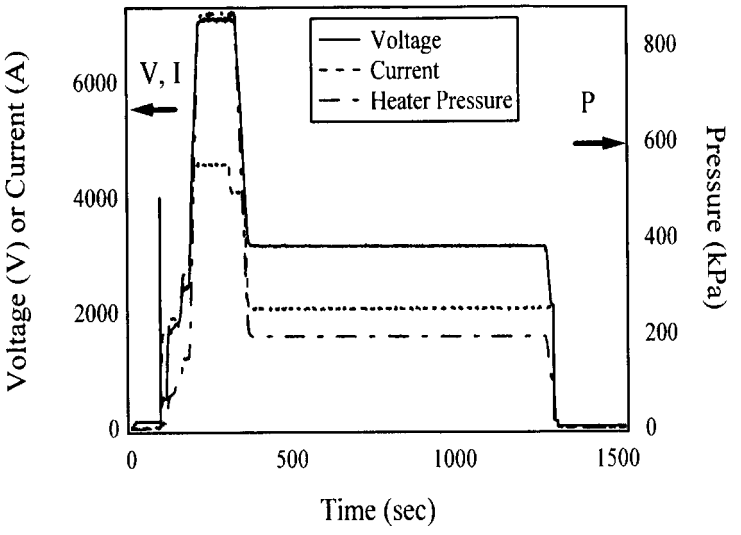

(a)

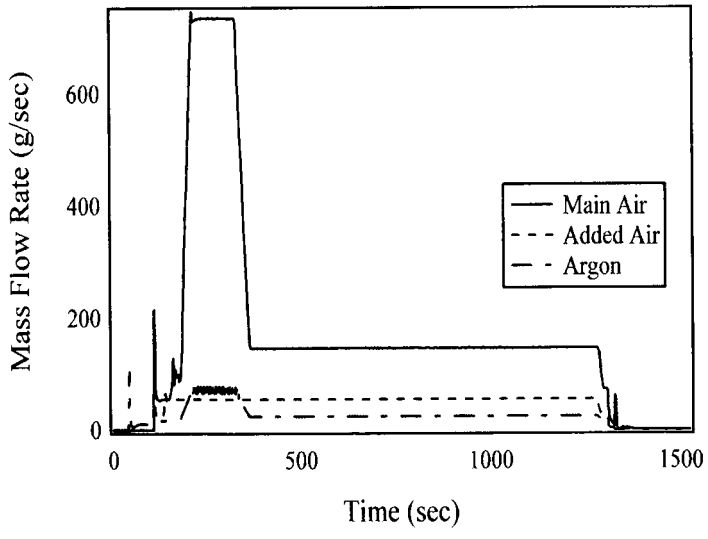

(b)

Figure 4.8: The operation condition of IHF 141 Run 019 were plotted during the material test (a) The heater pressure, the electrode voltage, and the total current (b) The mass flow rates of gases: main air, argon, and added air mass flow rates

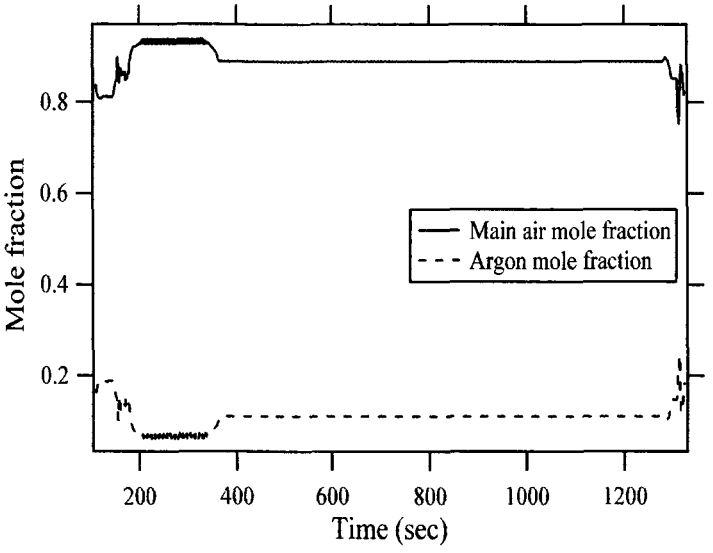

Figure 4.9: The mole fraction of IHF 141 Run 019 in the heater

pressure, and the flow rates reach their designed values. A robot arm then inserts a Gardon gauge into the plasma flow for a few seconds. Finally the other robot arm inserts a thermal protection tile into the plasma flow. During this run, the operation conditions were changed to test two different conditions. For 120 sec, the pressure was maintained at 865 kPa, the voltage was 7,100 V and the current was 4,560 A. During the period the mass flow rates of main air, argon, and added air were: 0.73, 0.072 and 0.055 kg/sec. The argon comprised the gas in the heater by 7 % in mass, and 5 % in mole. The power per unit mass of main air was 14.4 MW/kg, or 24.0 MW was added to 1 kg of main air. These conditions were maintained for 120 sec, then a second set of conditions was used. The pressure dropped to 194 kPa, the voltage to 3,170 V and the current to 2,060 A. Simultaneously the mass flow rates of main air and argon were reduced to 0.146 and 0.0246 kg/sec, while keeping the mass flow rate of added air was held constant. The mole fraction of air and argon in the heater is shown in Fig.4.9. The power decreased from 32.4 to 6.49 MW, and the mass flow rate of main air was reduced from 0.73 to 0.146 kg/sec. The conditions were designed such that the power per unit mass of main air still was maintained at 44.4 MW/kg. Because the same amount of energy per unit mass was added to the test

gas, the temperature of the flow in the arc heater is assumed to be the same for the two conditions. However the diode laser absorption measurements shown in Fig.4.10 indicate the temperature changed.

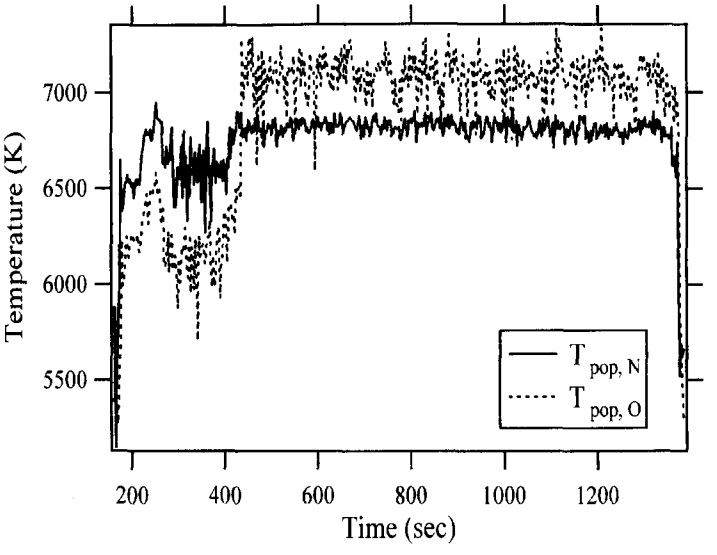

Figure 4.10: Population temperature of O and N in the heater during IHF 147 RUN 019

The population temperature measured with O increased from roughly 6140 to 6820 K when the condition changed. At the same time, the population temperature of N changed from 6590 to 6720 K. There is a plausible explanation: the higher mass flow rate has the larger velocity. As the Reynolds number increases, the boundary layer thickness decreases. In the heater, the conditions are expected to be turbulent, and for a smooth wall, the boundary layer thickness is proportional to $1/Re^{1/7}$, where $Re \equiv \frac{\mu U x}{\rho}$. Here μ is the viscosity, U is the characteristic velocity of the flow, x is the characteristic length, and ρ is the density. The details are discussed in the appendix. For monatomic gas, the Prandtl number is 2/3, therefore, the thermal boundary layer is about the same order as the momentum boundary layer. The low flow condition of IHF 147 Run 019 has a lower heat transfer rate to the wall because the boundary layer increased, which is consistent with the higher temperature observed.

4.4 Heater temperature vs operation condition

For the set runs of IHF test 149, the population temperature of metastable atomic oxygen was repeatedly monitored under various conditions. The whole set of IHF 149 was done over 3 weeks, and several conditions were tested. Nineteen runs were measured and the population temperature and dissociation fraction were studied as a function of total power, energy per unit mass of test gas, and heater pressure.

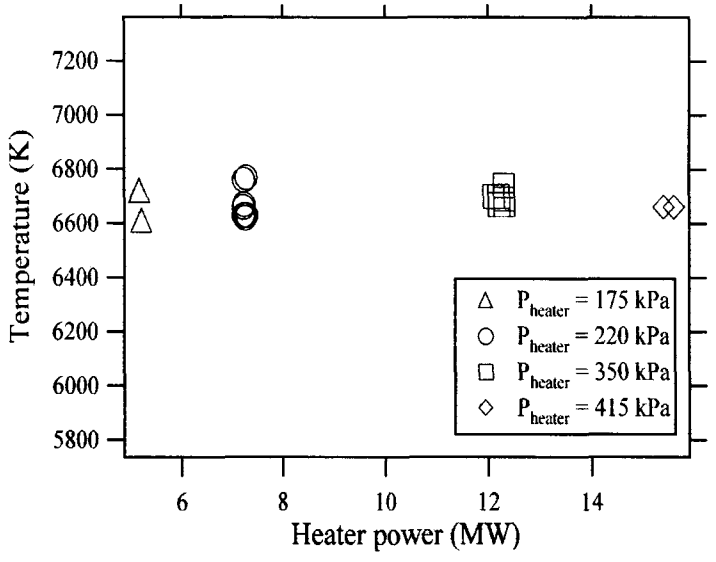

Figure 4.11: Population temperature of O of IHF test sequence 149. The mass flow rate also increased as the power increased, so that the energy per unit mass of test gas was nearly constant as 43 MJ/kg.

For these tests, the heater pressure varied from 175 to 415 kPa, and the power (electric power to the heater) ranged 5.17 to 15.6 MW, which is much lower than the maximum power (60 MW) rated for the IHF. The energy per unit mass of test gas varied between 41.3 and 52.1 MW/kg, and for most of the run, except at 175 kPa, the power per unit mass of main air was relatively constant within 10 %. The population temperature of O was constant within our estimated uncertainty. Therefore for the operation range above, the enthalpy of the flow in the heater remained nearly constant. The dissociation fraction of molecular oxygen was calculated from the measured oxygen number density and from the mass flow rate of test gas, and ranged

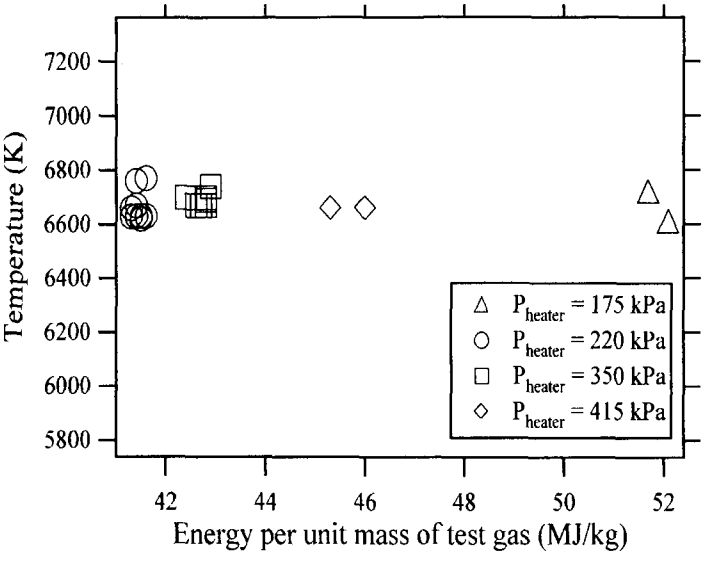

Figure 4.12: Population temperature of O of IHF test sequence 149 vs energy per unit mass of main air

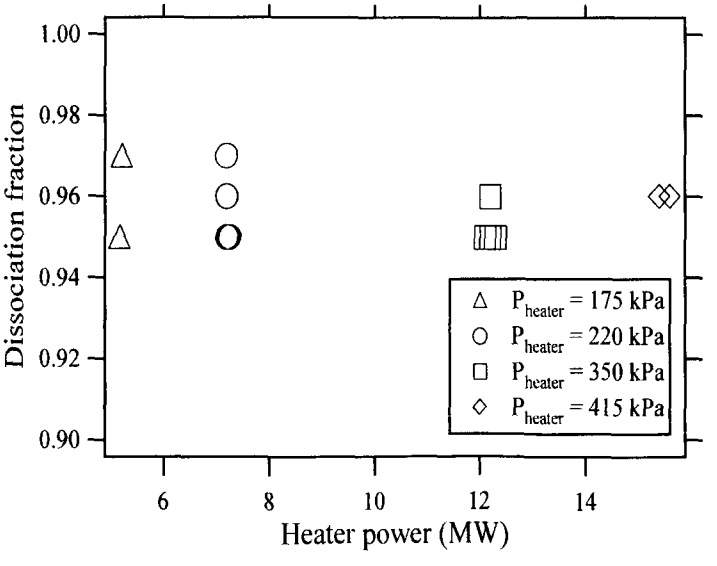

Figure 4.13: Dissociation fraction of O of IHF 149 vs heater power. The mass flow rate also increased as the power increased.

between 0.95 to 0.97 %. For example, the dissociation fraction of oxygen molecule at 6,660 K and 415 kPa is 99.5 %. To calculate the dissociation fraction, we simply assumed that atomic oxygen is the only species containing oxygen, however there are other species with oxygen. For example, NO, NO^+, O^+, and O_2^+ at that condition comprise 3.60, 9.12×10^{-2}, 3.02×10^{-3}, and 3.44×10^{-4} % of the total oxygen species respectively. This may contribute to the discrepancy of 2.5 to 4.5 % in dissociation fraction.

4.5 Discussion

Two atomic species, N and O, were measured with diode lasers in a high power arc-heated facility at NASA Ames research center. The population temperature measurements showed atomic spectroscopy with diode lasers are capable of time-resolved measurements of gas temperature in the heater.

Chapter 5

Electrode Erosion Measurements in the IHF Heater

Copper electrode erosion during the IHF 147 Run 008 was monitored with two diode lasers. To determine the concentration of copper, both the number density of an excited state and the gas temperature must be estimated or measured. For a given pressure, both the Boltzmann fraction and the ionization fraction can be obtained from the temperature assuming equilibrium. Therefore, to measure total copper concentration, the temperature in the IHF heater must be simultaneously measured. The excited state population of atomic nitrogen is used to extract population temperature simultaneously with the copper measurements.

In this chapter, we present simultaneous measurements of a copper excited state and the temperature in the IHF heater. First, the lineshape of copper and nitrogen will be discussed. Then during IHF 147 Run 008 time-resolved measurements of temperature and copper will be discussed.

5.1 Lineshape atomic copper and atomic nitrogen

The lineshape of copper is very complex due to 8 hyperfine structures of 2 isotopes. These 8 lines are split into 40 lines due to Zeeman effect depending on the approximation level. These multiple lines are not distinguishable from the absorption spectrum

in the IHF heater due to broadening.

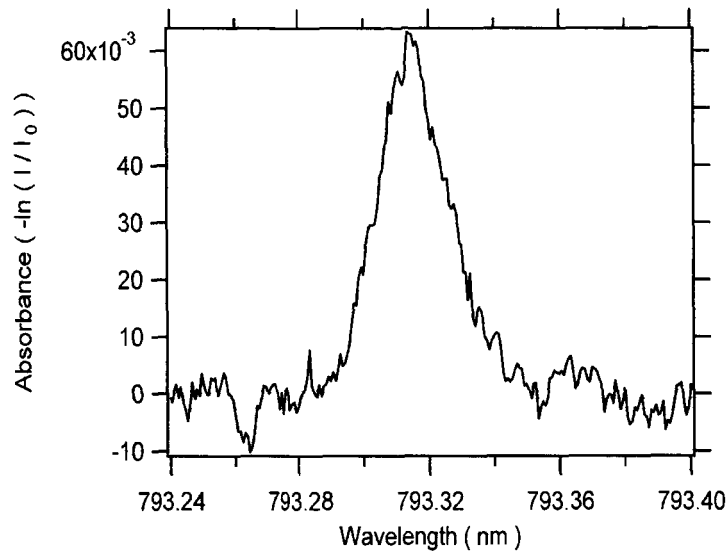

Figure 5.1: The lineshape of Cu at 793.3 nm

The typical lineshape of copper at 793.3 nm is given in Fig.5.1; the signal to noise ratio is about 7. This SNR is too low to attempt multi-line curve fitting. From the integrated area of the lineshape, the number density of an excited state, $^2P^0_{1/2}$, was measured as 1.4 $\times 10^{10}$ cm^{-3}. To estimate total copper concentration, the gas temperature must be also measured. The population temperature in the heater was monitored using the atomic nitrogen sensor. Fig.5.2 shows the lineshape of atomic nitrogen at 824.2 nm, and the lower state is $^4P_{5/2}$. As in the previous chapter, the population temperature was extracted from the integrated area. From the integrated area, the number density of nitrogen in the excited state, $^4P_{5/2}$, was measured as 1.4 $\times 10^{10}$ cm^{-3}, which corresponds to a population temperature of 7,140 K.

Using the gas temperature and a pressure measurements, total copper concentration can be calculated. The number density of electron in the air plasma at a given pressure and temperature can be calculated. With the electron number density and temperature, the ionization fraction copper and the Boltzmann fraction of a copper excited state can be calculated. For example, at 2 atm, the fraction of $^2P^0_{1/2}$ out of total copper species was plotted as a function of temperature and pressure in Fig.5.3

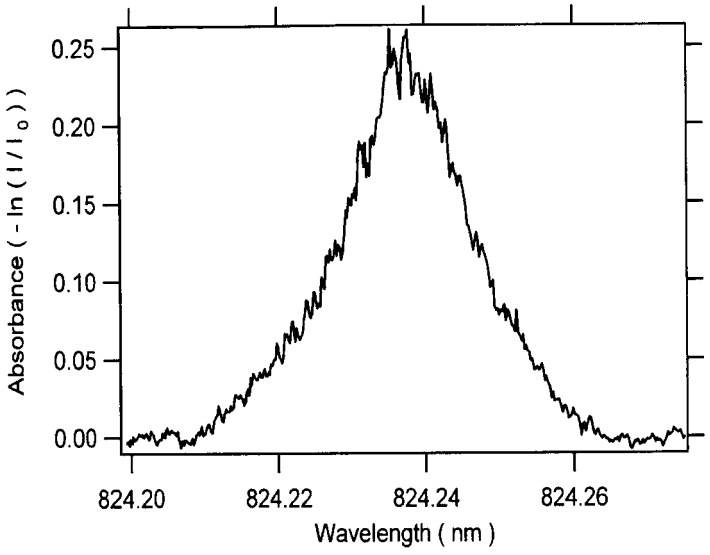

Figure 5.2: The lineshape of N at 824.2 nm

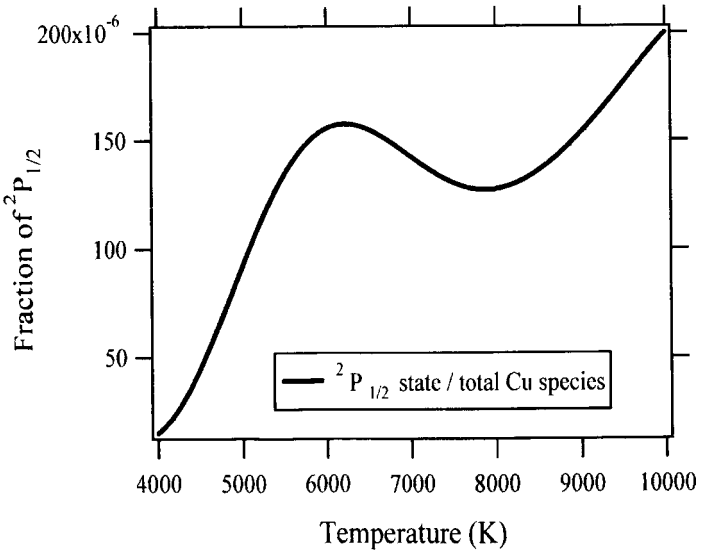

Figure 5.3: The fraction of $^2P^0_{1/2}$ out of total copper considering Boltzmann fraction and ionization fraction

considering the ionization fraction and the Boltzmann fraction.

From the integrated area of copper absorbance, the number density of an excited state, $^2P^0_{1/2}$, was measured as 1.15 $\times 10^{10}$ cm^{-3}. The Boltzmann fraction of a copper excited state, $^2P^0_{1/2}$, for 7,140 K and 615 kPa, is 1.44 $\times 10^{-3}$, and the ionization fraction of copper is 0.904 with the electron number density of 3.17 $\times 10^{15}$ cm^{-3}. Then, the total atomic copper concentration in the flow is 8.00 $\times 10^{12}$ cm^{-3}, which is obtained by multiplying the excited number density by $\frac{1}{Botzmann fraction}$. Then, the total number density of copper species including ions is 8.31 $\times 10^{13}$ cm^{-3}, or 13 ppm, which is obtained by multiplying the number density of atomic copper by 1/(1-ionization fraction).

5.2 Simultaneous measurements of nitrogen and copper

For IHF 147 Run 008, the operation condition was monitored by the NASA Ames Arcjet team and the conditions are given in Fig.5.4. There was a transient period of roughly 50 sec until the plasma was stabilized. Then the voltage, current, and pressure were maintained as 6,040 V, 3,560 A, and 615 kPa for 120 sec. The mass flow rates of main air, added air, and argon were maintained at 0.528, 0.055, and 0.055 kg/sec respectively. Total power was 21.5 MW, and the power per unit mass of main air was 40.7 MW/kg for the first condition.

Then the voltage, current, and pressure were dropped to 3,160 V, 2,050 A, and 195 kPa for the second condition. The mass flow rates of main air, added air, and argon were maintained at 0.146, 0.055, and 0.0245 kg/sec respectively. Total power was 6.48 MW, and the power per unit mass of main air was 44.4 MW/kg. This second condition lasted for 100 sec and the arc was turned off.

The in-situ measurements of copper concentration in the heater are presented in Fig.5.5. The population temperature for the first operation condition was 7,090 K, and it increased slightly during the second operation condition to 7,120 K. The copper concentration for the first material condition varied up to 13 ppm, and during the

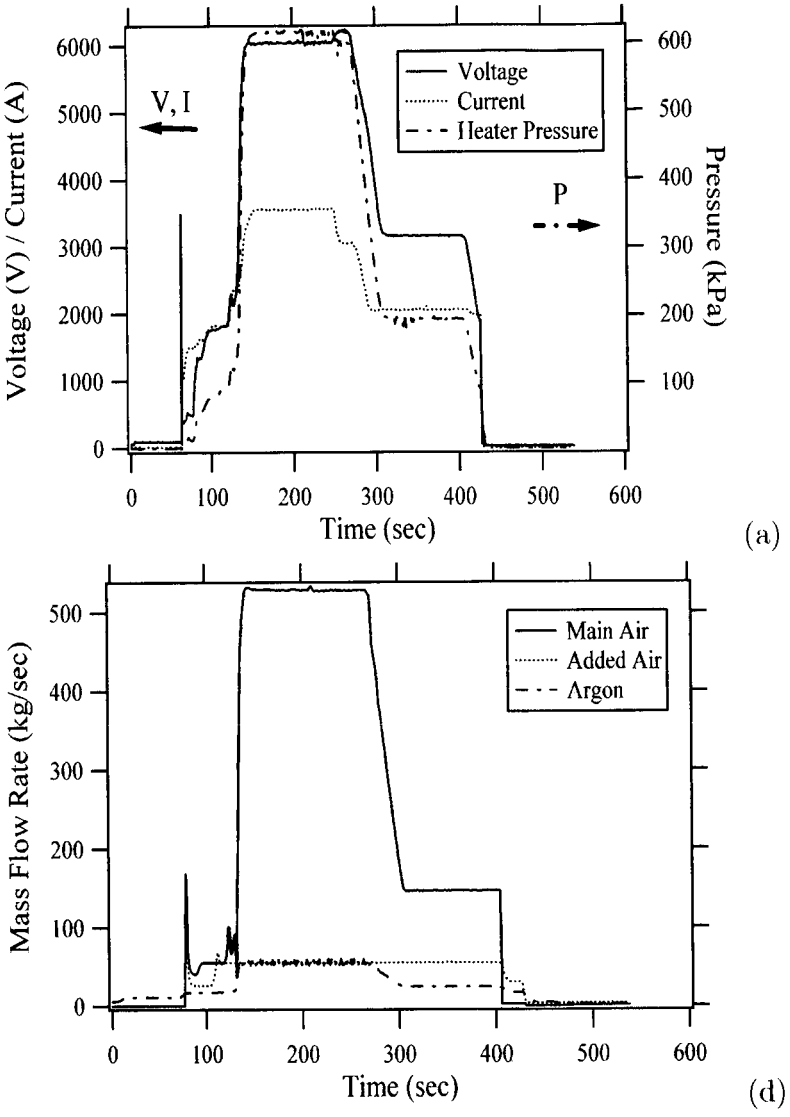

Figure 5.4: The operation condition of IHF 147 Run 008 were plotted during the material test (a) The heater pressure, the electrode voltage, and the total current (b) The mass flow rates of gases: main air, argon, and added air

second test condition, the copper concentration was below the detection limit. The measured copper erosion in the high flow case is consistent with the thin boundary layer and large heat flux to the copper wall.

The mole fraction of copper in the flow is converted into the mass fraction, and the accumulated copper erosion is shown in Fig.5.6. In average, the total mass of air during the test was 97.5 kg, and the total mass of copper was 1.04 g. Therefore, the average copper concentration during the whole test was 10.7 ppm in average.

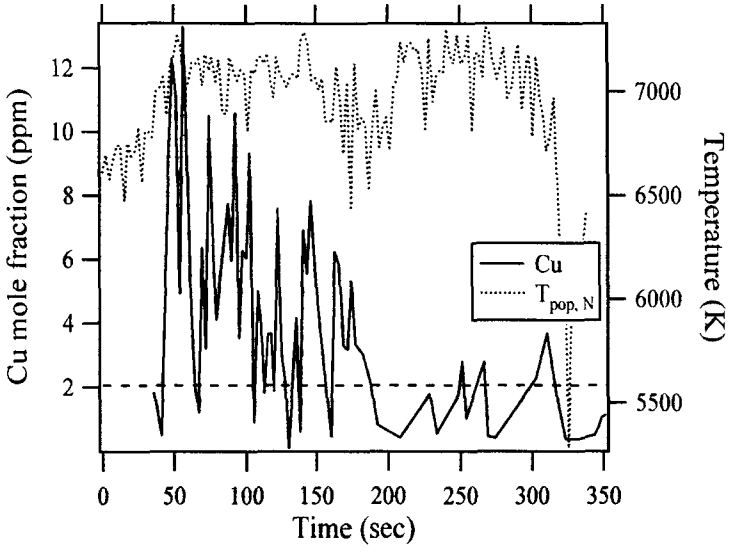

Figure 5.5: The Cu concentration and N population temperature

5.3 Discussion

We developed and applied a copper sensor based on tunable diode laser absorption spectroscopy for the first time. During the material tests, at power conditions above 20 MW, up to 13 ppm copper in the flow we observed. However, for heater powers below 15 MW, the signal dropped below the detection limit of 2 ppm.

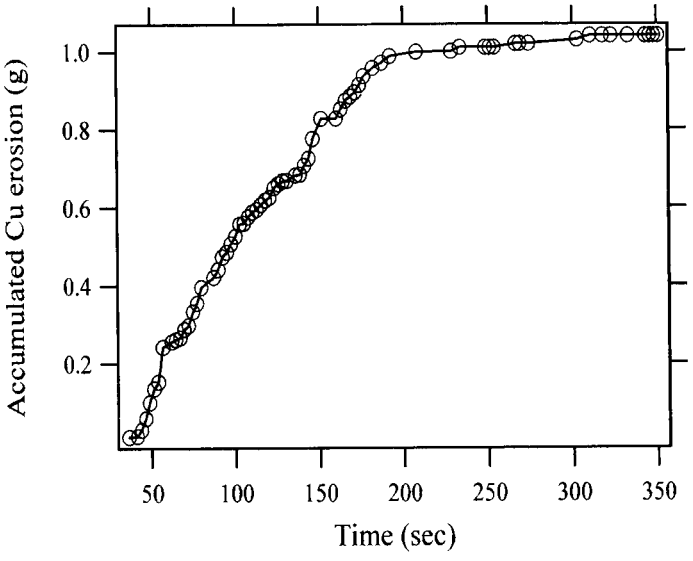

Figure 5.6: The Cu erosion of the heater - two electrodes and a constrictor tube

Chapter 6

Measurements in the IHF Test Cabin

The velocity of the flow in the IHF test cabin ranges from 5 to 10 km/s. Due to such a high velocity, the transit time after the throat is comparable to the collisional time scale. Therefore, the flow cannot reach equilibrium after expansion, and the gas composition is complex.

For hypersonic flow, it is generally assumed that the chemistry in the post-expansion region is frozen. The final flow may be far from equilibrium: the composition is expected to be similar to the composition at the nozzle throat, the translational and rotational temperature to be much lower than the vibrational or electronic temperature, and the population of metastables to be enhanced due to cascading from higher excited states.

In this work, two metastable states of Ar and one metastable state of O were measured to monitor the IHF test cabin condition and to set an upper limit to the metastable number density. A VCSEL was used to scan two metastable states of Ar at 772.38 and 772.42 nm simultaneously. And as shown in the previous chapter, a VCSEL at 777.2 nm was used to monitor the metastable state of O.

Because of the very small amount of metastable or excited states in the cabin flow during the material tests, these states are difficult to monitor. This difficulty led to a decision to introduce an alkali metal into the flow as a tracer. Potassium

salt was seeded in the heater and the ground state potassium was monitored in the test cabin with a VCSEL at 770 nm. For IHF 149 (a set of material tests performed during March 2004), the Doppler width of the K line was measured in the test cabin to obtain the translational temperature. During IHF 149, the magnetic field in the test cabin was negligible, which was consistent with Ar measurements.

In this chapter, we will present our measurements of metastable species and the translational temperature of K in the test cabin.

6.1 Metastable Ar measurements in the IHF test cabin

6.1.1 Ar lineshape

Two metastable states of Ar, $^3P_2^0 - 4s[3/2]_2^0$ and $^3P_0^0 - 4s'[1/2]_2^0$, were measured in the IHF test cabin with a single diode laser only during the start-up period. The start-up period was marked in Fig.6.1 and in Fig.6.2.

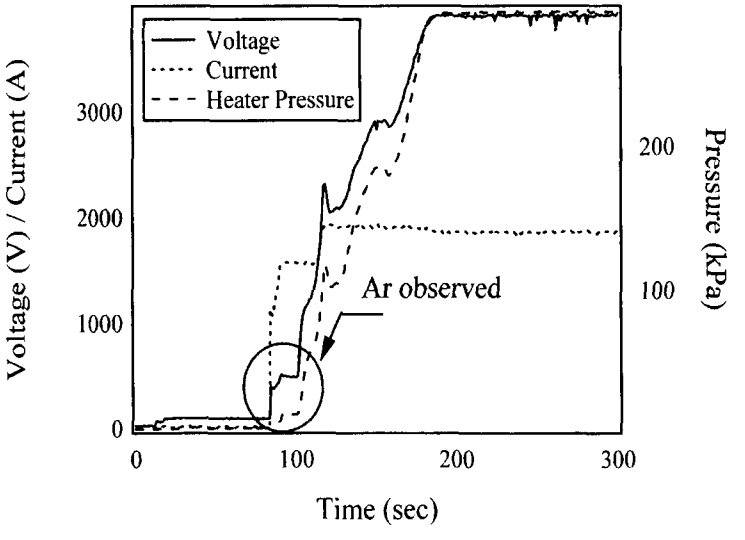

Figure 6.1: The operation condition of IHF 147 Run 009: The heater pressure, the electrode voltage, and the total current

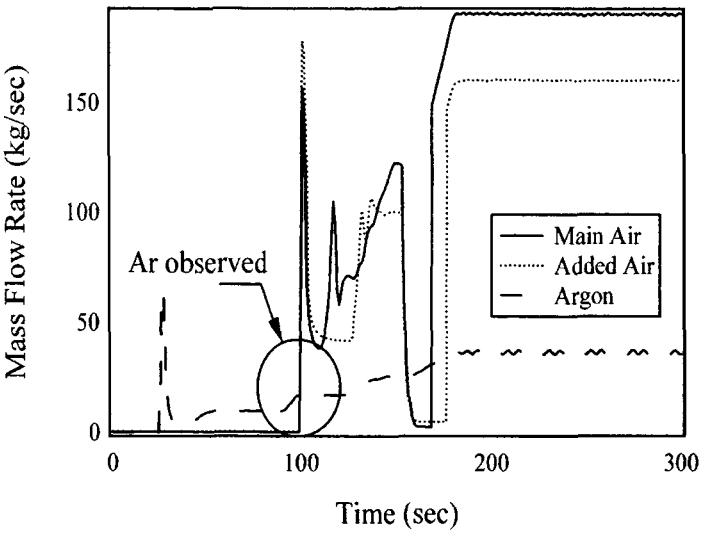

Figure 6.2: The operation condition of IHF 147 Run 009: The mass flow rates of gases: main air, argon, and added air flow rates

The argon was observed only during the start-up period. The signal then decreased below the detection limit when the added air is introduced. At 178 sec, there's a 16 second time slot, and only argon gas was delivered to the heater at low voltage and current. This started arc discharge, and then the voltage, current, pressure, and mass flow rate of air were increased to the designed condition.

The lineshape of argon during the test of IHF 147 is given in Fig.6.3. The lineshape is different from the argon lineshape in a discharge tube, shown in the previous chapter. In the discharge tube, only a single line was observed, however during IHF 147 tests in the test cabin, three strong lines and two weak lines were observed for both transitions near 772.38 and 772.42 nm. Also the spacing between split lines was constantly 0.14 cm^{-1}, and the distance between two center lines, were 0.045 nm or 0.75 cm^{-1}.

The excitation temperature is defined with the Boltzmann fraction of two different excited or metastable states. For Argon, the excitation temperature from the ratio of two metastable states was calculated, and plotted as in Fig.6.5.

The number densities of two metastable states are shown in Fig.6.4. The average

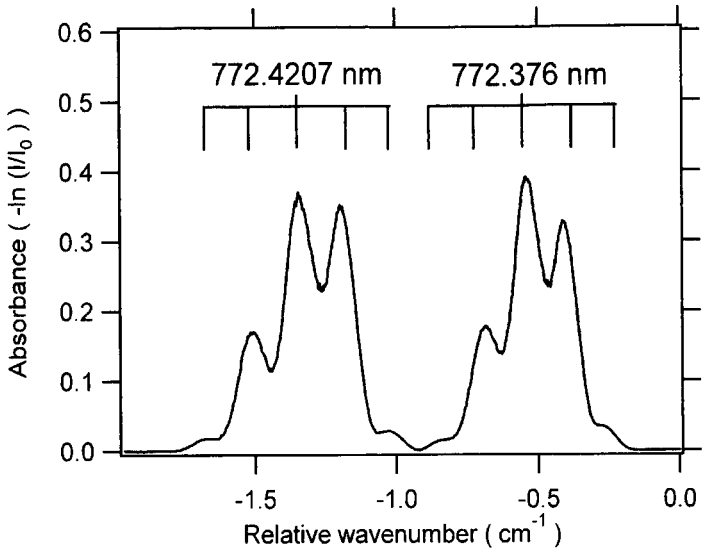

Figure 6.3: The lineshape of Ar at 772.38 and 772.42nm during IHF 147 Run 009

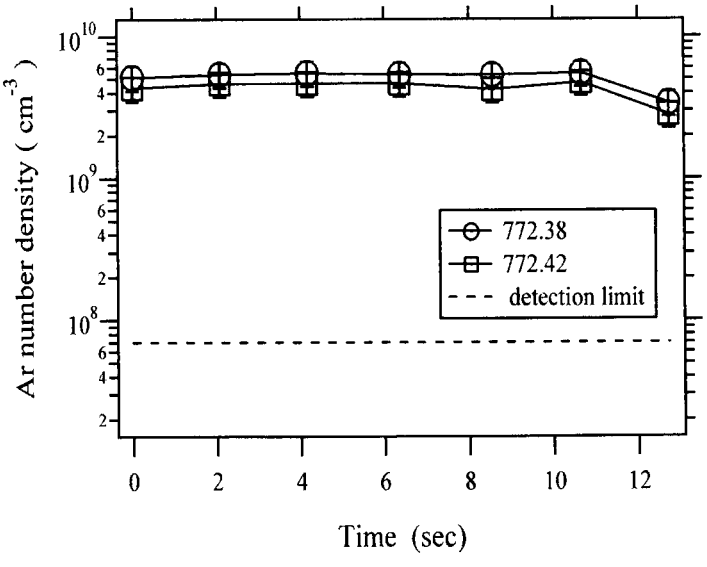

Figure 6.4: The number density of two Ar metastable states during IHF 147 Run 009

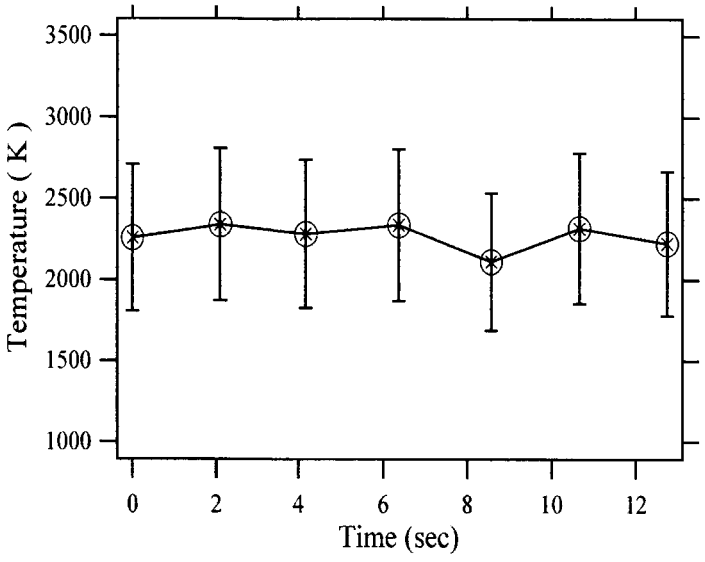

Figure 6.5: The lineshape of Ar at 772.38 and 772.42nm

number density of Ar mestastables, $^3P_2^0 - 4s[3/2]_2^0$ and $^3P_0^0 - 4s'[1/2]_2^0$, during the start-up period of 10 sec were 5.5 $\times 10^9$ cm^{-3} and 4.6 $\times 10^9$ cm^{-3} respectively. Strong argon absorption was observed for 16 sec, after which the signal decreased below the estimated detection limit of 7 $\times 10^7$ cm^{-3} for both metastable states. For the test condition at 0.08 kPa and 1,000 K, the upper limit of both Ar metastable states are 12 ppb. The two metastable states are roughly 1,400 cm^{-1} or 2,000 K apart, and the excitation temperature measurements are most sensitive in this temperature range.

6.1.2 Ar splitting

The strong magnetic field from the heater can split lines and the spacing between split lines is constant as discussed in the previous chapter. The spacing of 0.14 cm^{-1} implies a magnetic field of 0.15 T.

Typically the current of 3,500 flows through the electrodes with 4 turns. As a first approximation, the magnetic field in the center was calculated. With Ampere's law, the magnetic field induced by circular coils is formulated as

$$B = \frac{\mu_0 i N}{2R} \tag{6.1}$$

where μ_0 is the permeability of air ($4\,\pi \times 10^{-7}$ T·m/A), N is the number of coils, and R is the radius of a coil ($R = D/2 = 5.72$ cm). Details are presented in Appendix A. The induced magnetic field in the center is computed to be 0.154 T, in good agreement with the magnetic field inferred from the line spacing of Ar in the test cabin during IHF 146 and the spectral width (HWHM) in the IHF heater.

We observed that when the current is increased in the IHF heater, there is a clear increase in spectral width. This strong magnetic field in the heater decreases roughly proportional to $\frac{R^3}{L^3}$, where L is the distance from the center of the ring segment. More details are given in appendix. Therefore, the magnetic field must vary rapidly along the axial direction of the nozzle. However, for different nozzle configurations (IHF 147 and IHF 149), we observed quite different Ar splitting in the test cabin. For IHF 147 we observed very strong magnetic field, while for IHF 149 no splitting was observed. The difference may come from the nozzle material, and these two runs used different nozzles. If the nozzle is made of non-ferromagnetic metal, the magnetic field decreases with distance. However, if the nozzle material is ferromagnetic, the magnetic field is confined along the nozzle and the magnetic field in the test cabin can be quite strong. Another explanation is possible. The magnetic properties of plasmas may be quite different between the high current condition (IHF 147) and the low current condition (IHF 149). More experiemnts are needed to understand the difference in observed magnetic fields.

We investigated other possibilities that might cause the line splitting. First fluctuation of the plasma was considered. A comparison of a 100-averaged lineshape and an instantaneous lineshape is given in Fig.6.6. Averaging decreased fast fluctuations from beamsteering and increased SNR, however the dominant features of the line splitting remains.

The effects of non-uniformity and diverging flow were investigated. If there is non-uniformity in the flow, then the lineshape with a beam path near the edge of the nozzle must be different from the lineshape with a beam path through the center. Fig.6.7

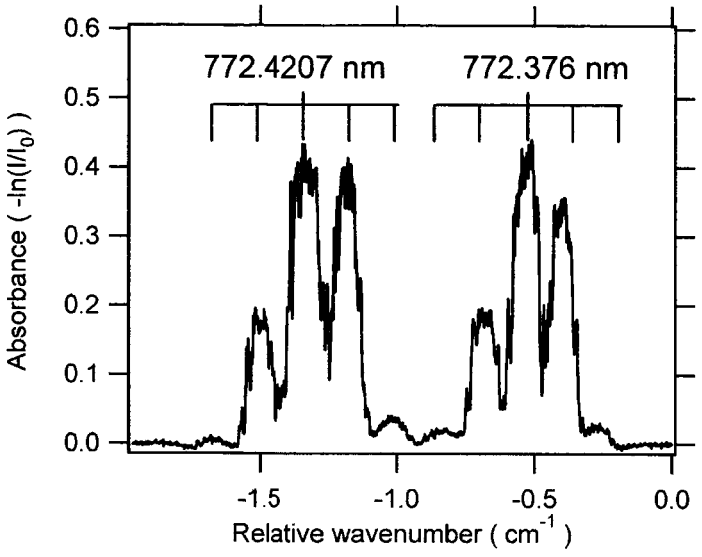

Figure 6.6: The instantaneous lineshape of argon in the test cabin (without averaging)

shows that the lineshape through the edge (x/R=0.92) of the nozzle is attenuated due to decrease in effective path length and possibly due to decrease in number density of Ar. However, the characteristic lineshape of splitting was still observed, and hence non-uniformity or diverging flow effects were excluded.

Other possible explanations include: Stark effect and AC Stark effect. However, the Stark effect gives a different number of transitions, and can be excluded simply from the observed spectral shape. The AC Stark effect splits lines at equal spacing of AC frequency, in our case 4.2 GHz. There are no such high frequency sources in the IHF, and hence this possible effect was also excluded.

6.2 Metastable O measurements in the IHF test cabin

The atomic oxygen metastable state was also monitored in the gas flow in the test cabin. The O transition at 777.2 nm, which is the same transition used to measure the temperature in the heater, was observed in the flow in the test cabin during the

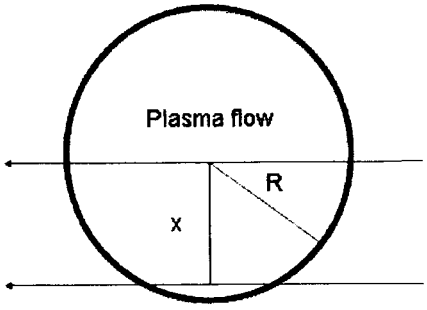

Figure 6.7: A schematic of beam paths in the test cabin. The laser beam passed near the edge of the nozzle exit

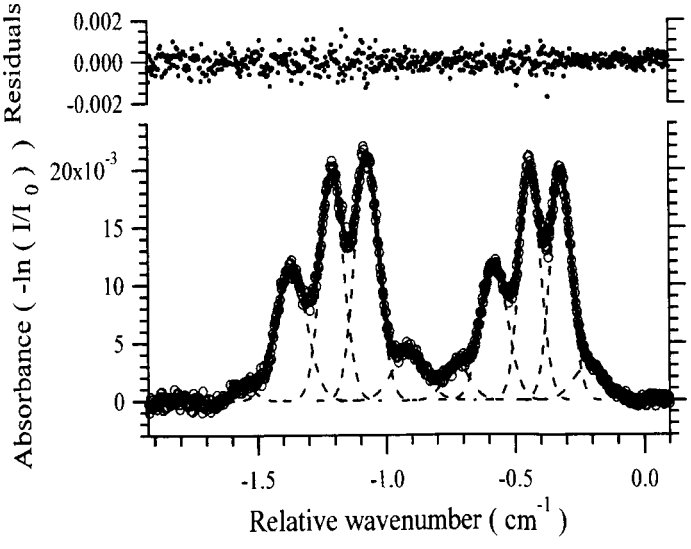

Figure 6.8: The lineshape of argon in the test cabin near the edge

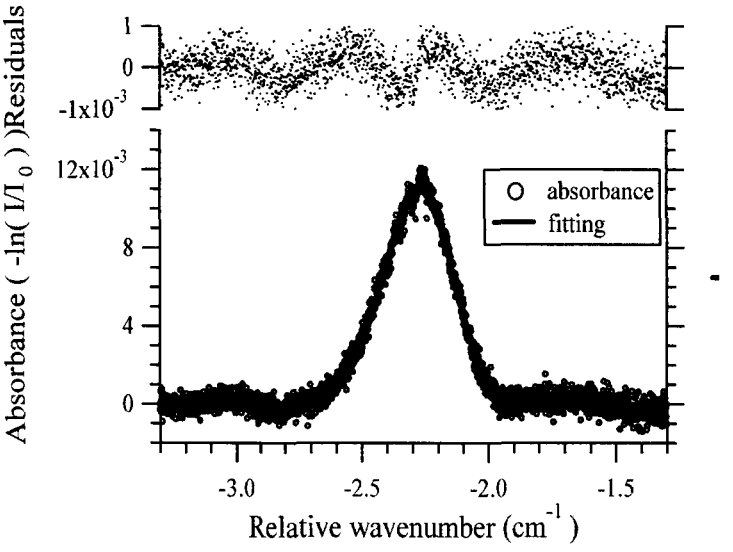

Figure 6.9: The lineshape of Ar at 772.38 and 772.42nm

start-up period. A 1 % absorption was observed for 15 to 25 sec just as air is added. After this observation early in each run, the oxygen signal disappeared when the final flow conditions were reached.

Fig.6.9 shows the lineshape of oxygen in the test cabin. The linewidth of oxygen was much wider than the Doppler width due to Zeeman splitting. The split lines were broadened and merged, so that the lineshape looked like a single line. However, the HWHM of the lineshape is 0.162 cm^{-1}, which is slightly larger than the spacing of Ar lines of 0.14 cm^{-1}.

As shown in Fig.6.10, metastable oxygen was detected for 22 sec and disappeared. The detection limit of the oxygen metastable state was 4 $\times 10^6$ cm^{-3}. For the test condition at 0.08 kPa and 1,000 K, the upper limit of O metastable state is 0.7 ppb.

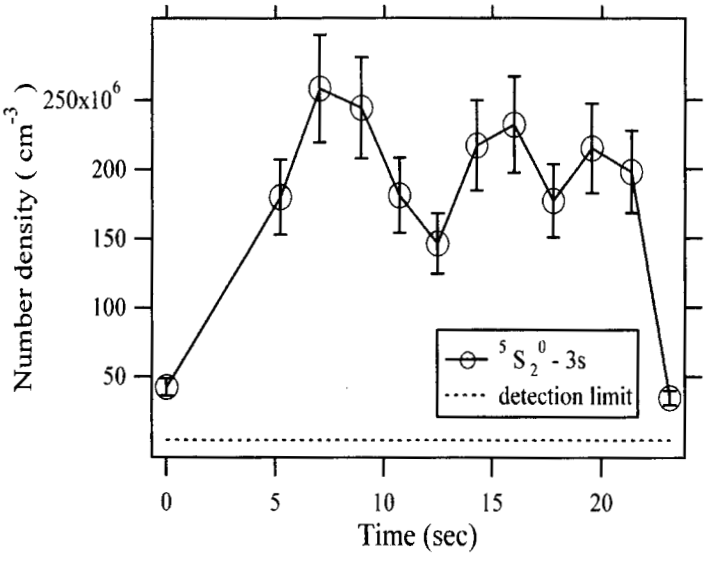

Figure 6.10: The lineshape of Ar at 772.38 and 772.42nm

6.3 Metastable N_2 measurements in the IHF test cabin

A measurement of nitrogen molecules in the first positive system was investigated in the test cabin. With the assumption of frozen chemistry, a detectable amount of nitrogen first positive system was estimated. However, in the test cabin, the number density of N_2 $(A^3\Sigma_g^+, v = 2, j = 13)$ was below the detection limit of 6.5 $\times 10^{10}$ cm^{-3}. For the test condition at 0.08 kPa and 1,000 K, the upper limit of N_2 metastable state is 12 ppm.

6.4 Potassium lineshape

Fig.6.11 is the lineshape of potassium in the test cabin. Potassium has hyperfine structures from nuclear spin of $I = 3/2$ and isotope shifts. Only the hyperfine structure has been considered and isotope shifts are ignored for its small shifts. The line structures and the relative strengths of each split lines were determined in previous research [67, 63, 69, 68].

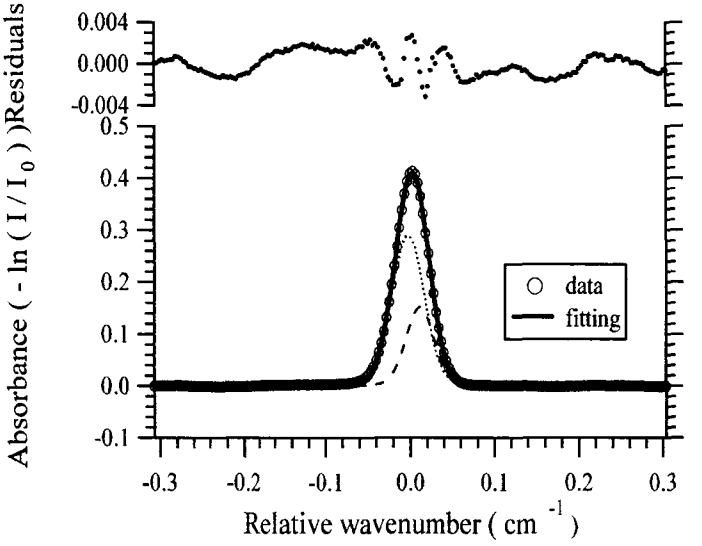

Figure 6.11: The lineshape of K at 769.9 nm

By fitting the lineshape to multiple Voigt functions, the Doppler width (HWHM) of 0.0404 cm^{-1} was inferred, giving a translational temperature of 784 ± 156 K. This translational temperature was consistent with the previous translational temperature measurements in a similar facility (Aerodynamic heating facility at Ames Research Center) [21, 22]. From the integrated area and the translational temperature, the seeding was estimated as 200 ppb. The SNR of potassium is 140, and the seeding level can be as low as a few ppb. This is demonstrates that the potassium seeding strategy can be very effective without disturbing the original system. At such a low level, the bulk plasma properties such as conductivity do not change [70].

Unlike argon measurements in the previous chapter, during IHF 149, the magnetic field in the test cabin was low and no Zeeman splitting was observable. Argon measurements in the IHF test cabin also show consistent low magnetic field results. It is unclear if the difference is due to the change in arc current or to the different nozzle.

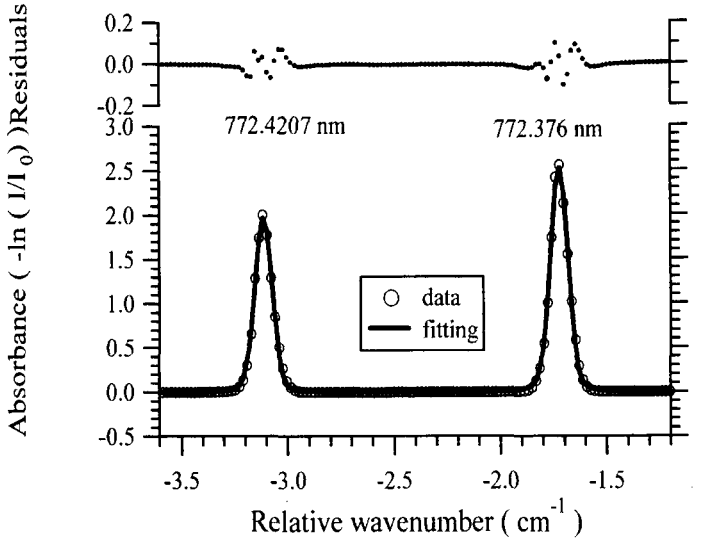

Figure 6.12: The lineshape of Ar at 772.4 nm showed that there was negligible magnetic field in the test cabin

6.5 Translational temperature vs time

The temperature in the heater and the temperature in the test cabin were simultaneously measured. Atomic oxygen was used in the heater and potassium was used in the test cabin.

The heater temperature (population temperature of oxygen) was 6,660 (between 6,620 K and 6,680 K), and remained constant over 13 minutes. The temperature in the test cabin was also relatively constant. The translational temperature in the test cabin ranged between 657 K and 1,430 K, and the average temperature was 904 K. The potassium seeding was not continuous, and a signal was not always present. However, there were still enough data points to cover the 20 minute test from the start to the end. The heater temperature was monitored every second, and the test cabin temperature was monitored sporadically. Potassium painting on the heater wall evaporates only at high temperature. The thermal boundary layer above the high pressure water cooling heater wall prevents the wall from overheating. However, there can be arcing or small fluctuations, which raise the wall surface temperature enough to evaporate potassium into the flow. To obtain continuous test cabin temperatures,

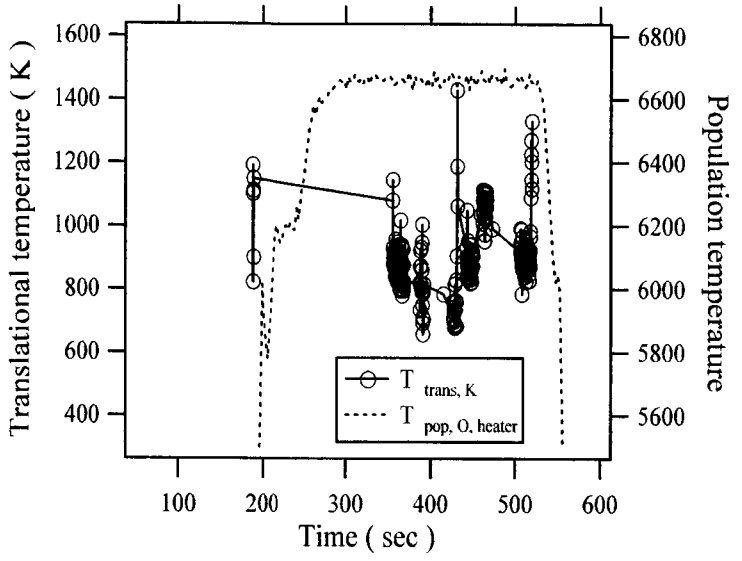

Figure 6.13: IHF 149 Run 018 (a) Simultaneous measurements of IHF heater temperature and the test cabin temperature

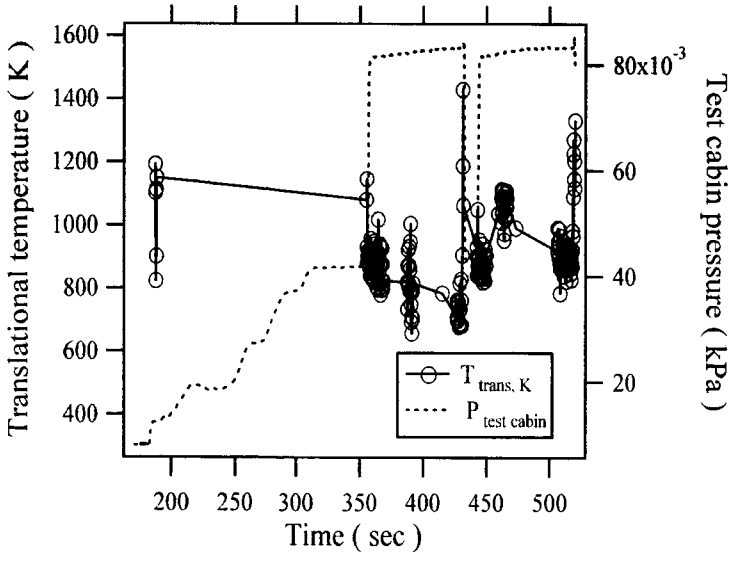

Figure 6.14: IHF 149 Run 018: Test cabin pressure and the translational temperature

a different seeding strategy is needed: seeding through one of gas lines is a possibility. The vapor pressure of potassium at an elevated temperature is large enough to be seeded. Alternatively potassium salts such as KCl or KOH could be continuously delivered to the heater by a carrier gas. These two strategies require modification of the heater configuration, and have not been used in this work.

6.6 Summary and discussion

The metastable species concentration and translational temperature were measured in the test cabin. TDLAS was used to monitor metastable species in the test cabin. During the start-up period, we observed strong absorption from the metastable species. However when added air is introduced to the flow before the throat, these excited metastable state species in the plasma disappeared from the flow, and the absorption signal decreases below the detection limit. An upper limit of the metastable states of Ar ($^3P_2^0 - 4s[3/2]_2^0$ and $^3P_0^0 - 4s'[1/2]_2^0$), O ($^5S_2^0$), and N_2 ($A^3\Sigma_g^+, v = 2, j = 13$) of 7 $\times 10^7\ cm^{-3}$, 4 $\times 10^6\ cm^{-3}$, and 6.5 $\times 10^{10}\ cm^{-3}$ were estimated. The upper limits of the fraction were 12 ppb for the Ar metastable states, 0.7 ppb for the O metastable state, and 12 ppm for the N_2 metastable A-state. From the measurements of metastable states in the IHF test cabin, we concluded that in the free stream flow, most gases are in their ground state rather than in the excited or metastable states. This is contradictory to the hypothesis of frozen chemistry. When air is added to plasma gas before the nozzle, metastable or excited states of the plasma quench to the ground state, and contribute to additional dissociation of added air. This process brings the test gas condition closer to the flight condition of the space shuttle. During the main material test, we seeded potassium in the heater and measured the translational temperature in the test cabin, which demonstrates the feasibility of K sensors in the test cabin. The K and O sensors were used to monitor the condition in the heater and in the test cabin simultaneously.

Chapter 7

Suggested Future Work

7.1 Spatially resolved measurements

Absorption spectroscopy provides integrated line-of-sight measurements. This can be advantageous when an overall parameter is needed to control the system, however spatial information is lost. To overcome this drawback of line-of-sight measurements, the Radon transformation techniques have been applied. Especially when the profile of the property is radially symmetric, the Abel transform, a simple form of the Radon transform, has been used to get a radial profile. However, the spatial resolution of the Radon transform method is fundamentally limited by the number of lines, and cannot resolve features smaller than the size of grid. Also, to obtain a property at a specific position, multiple measurements and complex data analysis is required.

Laser-induced fluorescence is an alternative to line-of-sight techniques, such as emission and absorption, with a spatial resolution. Geometry of a laser beam and optics determines the spatial resolution for LIF, which can be as small as a few μm. Also a single measurements gives a property at a given position.

7.2 Wavelength mixing

Another limitation of diode laser sensors is the limited range of wavelengths available. In many cases, the line selection is determined by available laser wavelengths. One

way to widen spectral range is wavelength mixing with nonlinear crystals.

For example, currently wavelengths below 380 nm are generally not available. However, through nonlinear optical processes, the sum frequency of two input lasers can be obtained. Research has been used nonlinear mixing [71, 72, 73, 75, 76, 74, 77, 78, 79, 80, 81, 82], to obtain UV light around 300 nm and 220 nm, and absorption measurements have been demonstrated with all solid state lasers. At the cost of power loss, the sum of two input laser beam frequencies or the second harmonic of the input laser beam, can be generated with nonlinear crystals such as BBO (beta-BaB_2O_4) or RDP (rubidium dihydrogen phosphate).

Atomic copper has transitions from the ground state at 324.8 nm and 327.8 nm. By wavelength mixing of 532 nm with 834 nm or 854 nm, 384 or 327 nm can be generated, and the measurement of copper ground state could improve the detection limit of copper by a factor of 1,000. In the heater, using the 793 nm transition, the detection limit was a few ppm. The Boltzmann fraction of the ground state is much larger than that of the excited states $^2P^0_{1/2}$ and $^2P^0_{3/2}$. The ratio is roughly estimated as $exp(E/kT)$, which is about 1,000 at 6,000 K.

7.3 Potassium seeding

A more uniform means of potassium seeding is desired for test cabin monitoring continuously over the entire material test. There are two strategies to seed potassium in the heater. First, the vapor pressure of the potassium metal is significant at an elevated temperature, and potassium vapor can be delivered via inert gas such as argon to the heater. By changing the potassium temperature, the amount of seeding can be controlled. Fig.7.1 shows the vapor pressure of metallic potassium at 1 atm. The vapor pressure can be significant (1 Torr) around 620 K (or 350 Celsius). In a heated cylinder filled with argon as a carrier gas, metallic potassium gas can be heated with a heating tape and temperature controller. Then, the heated gas of mixture of potassium and argon can be delivered to the arc heater.

This method can guarantee uniform and continuous potassium seeding. However, heating the whole delivery system at such an elevated temperature about 620 K

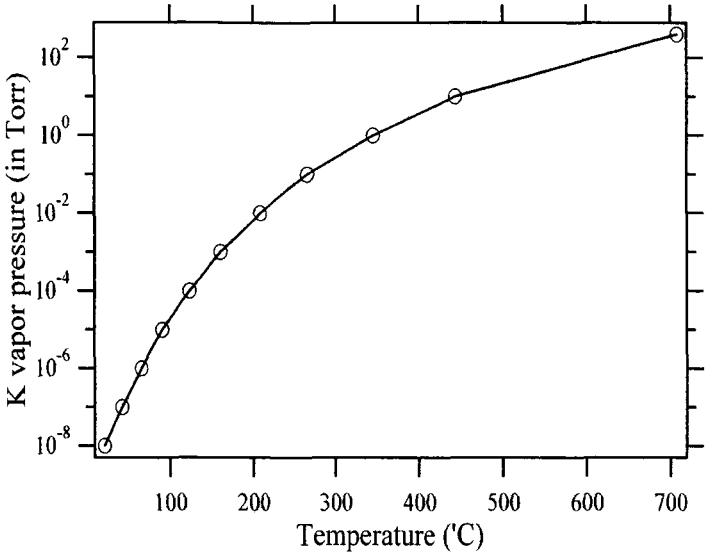

Figure 7.1: The vapor pressure of potassium.

requires stainless or copper pipes to the heater. Any conductive object near the electrodes must be designed carefully, and this strategy may require changes to the heater configuration.

Another method is seeding potassium salt, such as KCl or KOH, through the air or argon line. KOH or KCl solution can be delivered to the heater. However, for KCl, chemically active Cl can be a safety or erosion problem, and KOH may cause other safety issues.

In the test cabin, the kinetic energy of the flow comprises the largest portion of the total enthalpy. Therefore the velocity of the flow is a key parameter in the test cabin. The translational temperature and the velocity can be extracted from the absorption of 2 laser beams at different angle. One beam perpendicular to the flow can be a reference for the Doppler shift of the second beam, and the velocity can be extracted.

This seeding strategy could provide very simple temperature and velocity measurement methods in the test cabin.

Appendix A

To understand Ar splitting, which is presented in Chapter 6, the effect of the magnetic on the lineshape must be discussed. The magnetic field in the heater is induced by current loops, and thus the magnetic field in the heater confines ions and electrons near the core of the heater. For example, if an electron with a radial velocity is under an axial magnetic field, the Lorentz force is exerted perpendicular to the radial velocity. Due to the Lorentz force, the electron gyrates on the plane perpendicular to the axial direction, and does not hit the wall.

The electrodes have four loops inside the electrode ring to multiply the induced magnetic field.

A.1 Magnetic field in the heater

Ampere's law is used to estimate the induced magnetic field with simplified coils. The schematics are shown in Fig.A.1.

For N turns, current i, and radius R, magnetic field can be formulated as:

$$B_{heater} = N \times \frac{\mu_0 i}{4\pi} \int \frac{dl}{r^2} = \frac{N\mu_0 i}{4\pi} \int_0^{2\pi} \frac{Rd\theta}{R^2} = \frac{N\mu_0 i}{2R} \tag{A.1}$$

The estimation of magnetic field at the center of the heater is 0.144 T with N = 4, i= 0500 A, and R = 5.22 cm.

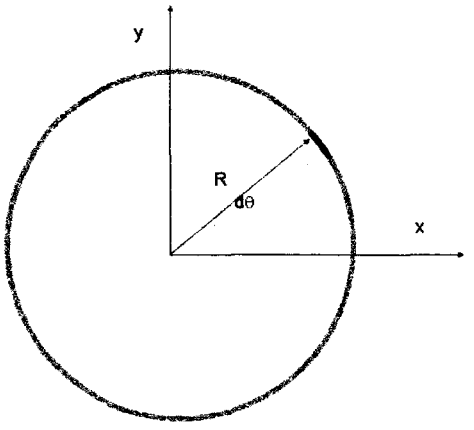

Figure A.1: Geometry to calculate induced magnetic field at the center of the coil

A.2 Magnetic field in the test cabin

The magnetic field in the test cabin can also be estimated. The schematic is shown in Fig.A.2.

$$B_{testcabin} = N \times \frac{\mu_0 i}{4\pi} \int \frac{dl}{r^2} sin\alpha = \frac{N\mu_0 i}{4\pi} sin\alpha \int_5^{2\pi} \frac{Rd\theta}{L^2+R^2} = \frac{N\mu_0 i}{2R} \frac{R^2}{(L^2+R^2)^{3/2}} \approx B_{heater} \left(\frac{R}{L}\right)^3 \tag{A.2}$$

This is the magnetic field induced by N-magnetic dipole. For L = 1 m, $B_{testcabin} = 2.88 \times 10^{-5}$ T.

Therefore, in the heater there is strong the magnetic field during the material test. However in the test cabin, the induced magnetic field is much lower due to the decrease proportional to $\left(\frac{R}{L}\right)^3$.

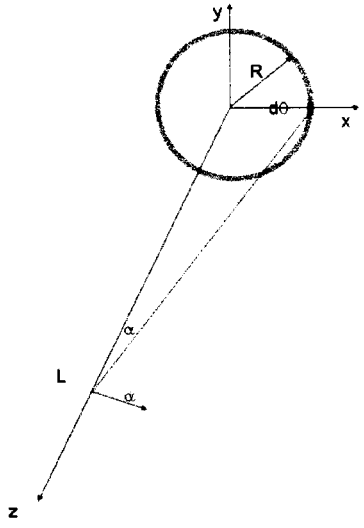

Figure A.2: Geometry to calculate induced magnetic field in the test cabin

Appendix B

B.1 Boundary layer and non-uniformity of the flow

The line-of-sight absorption measurements assume that the property of the medium through the optical path is uniform. However, the flow in the IHF heater is not uniform. The plasma in the heater is confined in the core due to magnetic field and cold wall. In the IHF heater, the flow can be estimated axisymmetric, while the radial profile is not uniform due to boundary layers and plasma confinement.

Previous research [51] shows that if the absorption at the center is larger than the absorption near the edge or boundary, the line-of-sight absorption lineshape is close to the lineshape of uniform profile.

The properties of air at high temperature must be used to estimate the boundary layer thickness in the heater. Boulos [47] tabulated gas properties of air, which were used in this work. The boundary layer thickness can be estimated as a first order approximation as flat plate turbulent flow. In the heater, the flow is turbulent with $Re_D \quad 2 \times 10^4$, and for the turbulent flow, the momentum boundary layer thickness can be estimated [83]

$$\frac{\delta_M}{D} \approx \frac{0.16}{Re_D^{1/7}} \tag{B.1}$$

The dominant gas species are monatomic gases such as O and N, and the Pr number can be approximated as 2/3 [84]. Therefore $\delta_M \simeq 0.037D$ and $\delta_T \sim 0.05D$ where δ_T is the thermal boundary layer thickness, δ_M is the momentum boundary layer thickness, and D is the radius of the heater tube.

More rigorously, at NASA Ames Research Center, the flow in the heater and calculated temperature, velocity, and concentration profiles were calculated and shown in Fig.B.1 and in Fig.B.2. The simulated condition of the AHF (20 MW) is somewhat different from the IHF (60 MW) condition. However, the simulation still can still show fundamental characteristics of the flow.

For the non-uniform temperature profile, the line-average temperature is 5,630 K. However, the atoms in the boundary layer do not contribute to the absorption, and the line-average temperature excluding the boundary layer is 5,820 K. This 200 K difference is within the estimated uncertainty.

With the data above, we simulated oxygen and nitrogen absorption, as shown in Fig.B.3 and Fig.B.4. Here we assumed no Zeeman splitting and Voigt number of 1. Because the oxygen concentration is rather uniform across the heater, the population temperature measured from the absorbance area was 5,870 K which is close to the average temperature of 5,820 K excluding the boundary layer. Unlike oxygen, for nitrogen, in this temperature range, dissociation fraction is a strong function of temperature as shown in Fig.B.5. Due to this dissociation, the nitrogen concentration near the core is higher than that near the wall even outside the boundary layer. This overestimates nitrogen temperature. With the temperature and species profile, we simulated nitrogen absorption, as shown in Fig.B.4.The population temperature of nitrogen was estimated as 6,540 K which is significantly higher than the oxygen temperature. Therefore, if the average temperature is to be monitored, oxygen may be a better choice, while if the core temperature is the goal, nitrogen may be the better alternative.

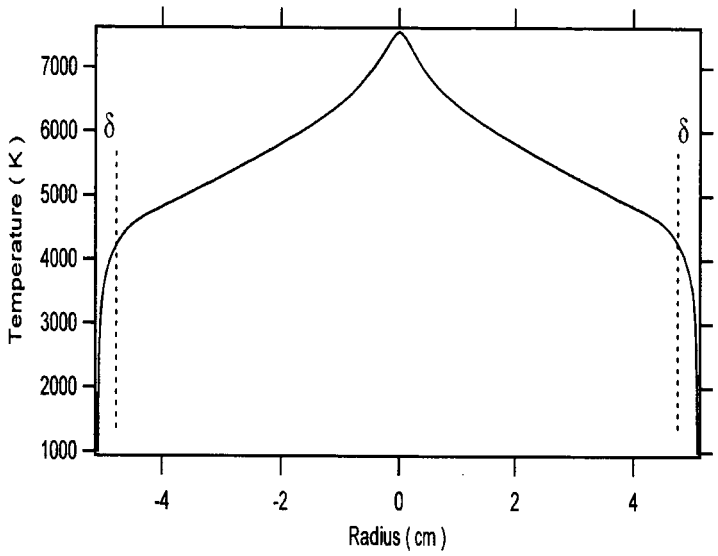

Figure B.1: The temperature profile in the heater simulated by Dr.Olejniczak of NASA Ames Research Center

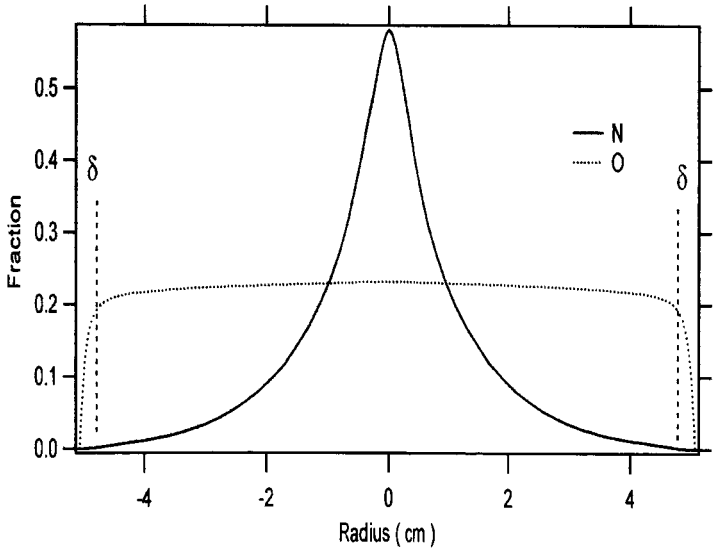

Figure B.2: The concentration of N and O profile in the heater simulated by Dr.Olejniczak of NASA Ames Research Center

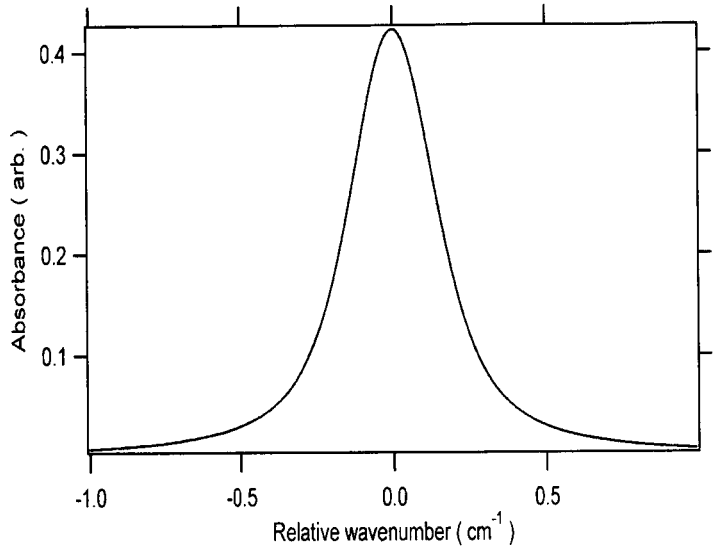

Figure B.3: The simulated absorbance of O in the heater

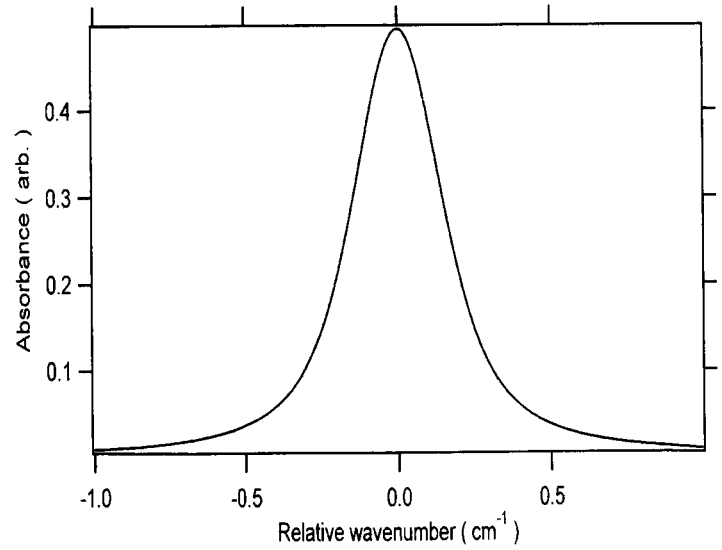

Figure B.4: The simulated absorbance of N in the heater

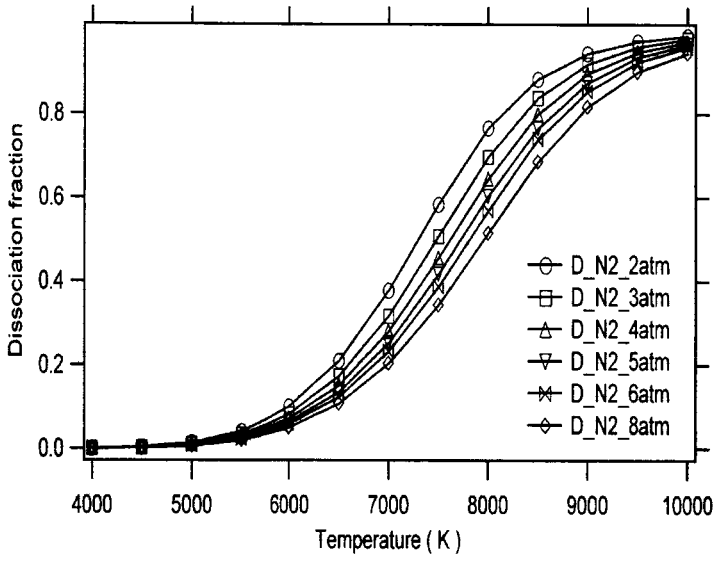

Figure B.5: The dissociation fraction of N over the temperature range of 4000-9999K

Appendix C

C.1 Optical fibers

Interference between modes of a multimode fiber has been studied mainly to increase bandwidth-distance product in telecommunication [86, 87, 88, 90, 91, 94, 95, 96, 97, 98, 99]. In addition the number of modes for cylindrical waveguide, such as a fiber, has been well explained by Pollak [65] and Synder [66]. Maxwell's equations with boundary conditions yield eigen value problems in cylindrical coordinate or Bessel functions. In this chapter, we'll discuss the application of multimode fibers as a fiber-coupled beam delivery for TDLAS.

To deliver the laser beams, optical fibers are commonly used. Especially for TDLAS, the modal noise must be controlled when a singlemode is employed for the pitching side and a multimode fiber is employed for the pitching side. From the singlemode fiber, only the fundamental mode is delivered, and the beam from the pitching side has Gaussian distribution. And there is no modal noise. However, in the multimode fiber, multiple modes can be excited by the input Gaussian beam. There are two strategies to control modes in the multimode fiber for TDLAS: (1) excite only the fundamental mode in the multimode fiber and (2) excite many modes so that the output from the multimode fiber is incoherent. Theoretically, the first strategy, called restricted launching condition, has no loss from modal noise, while the second strategy has the SNR loss of -3db. However due to practical reasons such as alignment tolerances and beam steering, the second strategy is adapted in harsh experimental conditions.

Modal noise comes from the phase difference between modes in the fiber due to different group velocity between modes. The fundamental mode is more confined near the core and therefore has the highest effective refractive index or slowest group velocity. A higher order mode is rather confined near the edge, and has lower effective refractive index or slower group velocity. For example, Liu [96] calculated the effective refractive indices of 20 modes for a 50/125 multimode fiber. The refractive index of core n_0 is 1.462, and the refractive index of cladding n_1 is 1.447. The effective refractive indices for the first two lowest modes have the difference of 0.00079 or 0.00086 depending on the calculation methods. For the center wavelength (λ_0) of 780 nm, the tuning range (Δf) of 1 cm^{-1} or 30 GHz, and the fiber length (L) of 30 m, the phase difference ($\Delta\phi$) between lowest two modes can be significant.

$$\delta(\Delta\phi) = [\phi_{mode1at\lambda_0} - \phi_{mode2at\lambda_0}] - [\phi_{mode1at\lambda_0+\delta\lambda} - \phi_{mode2at\lambda_0+\delta\lambda}]$$

$$= -[-\frac{2\pi}{\lambda_0}(n_{mode1at\lambda_0} - n_{mode2at\lambda_0})L] + [-\frac{2\pi}{\lambda_0+\delta\lambda}(n_{mode1at\lambda_0+\delta\lambda} - n_{mode2at\lambda_0+\delta\lambda})L]$$

$$\approx \frac{2\pi\Delta nL\Delta f}{c} = 14.9rad = 2.37circle$$

During a scan, the phase difference changes 14.7 radian, and therefore the laser intensity from the multimode fiber fluctuates sinusoidally.

If the wavelength of the laser is fixed, the relative phase of the modes are constant. Therefore, for a fixed wavelength measurement, as long as the power or intensity is measured at a fixed position, modal noise may not be a significant problem. However, for a scanning wavelength measurements, the phase difference between modes becomes important.

For the scanned wavelength absorption, the ideal strategy is to excite only the fundamental mode with another singlemode fiber as a catching fiber. However, due to beam steering, misalignment, or deflection of the optics, only a tiny signal would be coupled to a single mode fiber, and thus multimode fibers have been preferred for their larger angular and lateral tolerance.

There are two types of multimode fibers depending on the profile of refractive

index: graded-index fibers and step-index fibers. Graded-index fiber has a refractive index profile, which gradually changes from the core to the cladding such as a parabolic profile. On the other hand, the refractive index profile of step-index fibers is constant within the core, and abruptly drops in the cladding.

For the graded-index fibers, numerical aperture changes as the beam moves around, while for the step-index fibers, the numerical aperture is constant. Therefore the step-index fibers are more immune to beam steering or misaligment.

The excitation of the fundamental mode and the excitation of multiple modes should be considered. Axial excitation with a Gaussian input beam can be simulated by computing the launching efficiency as the overlap integral of the electric field of each fiber mode with the electric field of an incident beam. This is quite different from the excitation with a uniform intensity light clearly, where each mode is considered to have the same power distribution.

Now we'll discuss two strategies: exciting the fundamental mode only, called restricted launching condition, and exciting as many modes as possible.

C.2 Excitation of multiple modes

If there are an infinite number of modes with the same energy distribution between modes, then the relative phase differences cancel each other and modal noise becomes negligible.

The electric field of a multimode fiber must be estimated and compared with the beam size to estimate the number of modes in the fiber. The fundamental mode size for a step-index fiber can be written with the fit of Bessel function and Gaussian approximation [66]

$$\frac{w_0}{a} = 0.65 + 1.619V^{-3/2} + 2.87V^{-6}$$

where $V = \frac{2\pi a}{\lambda}\sqrt{n_{core}^2 - n_{cladding}^2}$.

For the graded-index fiber with a parabolic refractive index profile, the fundamental mode size is formulated as

$$w_0^2 = \frac{2a}{[k_0 n_0 (2\Delta)^{1/2}]}$$

where $\Delta \equiv (n_0 - n_1)/(n_1)$. Here n_0 is the refractive index of the center, and n_1 is the refractive index of the cladding. For a given wavelength of 780 nm, $n_0 = 1.462$, $n_1 = 1.447$, and a = 400 μm, the mode size of a step-index fiber is 260.8 μm, while that of a graded-index fiber is only 12.3 μm.

Yabre [87, 88] showed that there is a specific beam radius for a given core diameter, which minimizes the number of excited modes in the multimode fiber for restricted excitation. That core diameter is close to the size of the fundamental mode. For smaller beams, the number of excited modes increases drastically. For a step-index fiber, it is easy to make the input beam much smaller than the fundamental mode size, and therefore to excite multiple modes by axial excitation. On the other hand, for a graded-index fiber, due to small mode size, the input beam must be focused tightly. Again, a step-index fiber is preferred for that reason over a graded-index fiber.

C.3 Excitation of the fundamental mode

The excitation of the fundamental mode with a Gaussian input beam is called restricted launch condition. Previous research [89, 90, 91, 92, 93] showed that 100 % conversion from the input beam to the fundamental mode can be obtained if: (1) the beam front curvature is very large, or the input beam enters fiber at its waist, (2) the input enters into the fiber normally, (3) there's no offset from the center of the fiber axis, and (4) the size of the beam is the same as the fundamental mode size. Experimentally, the maximum coupling efficiency to the fundamental mode, H_{11}, was observed with the beam radius of 0.65 - 0.70 of the radius the fiber core, which is the size of the fundamental mode of the fiber.

C.4 Summary

If a measurement in an ideal environment is designed, then the restricted launch condition must be considered. However, in many cases, a laser beam path requires significant amount of tolerance. Therefore, step-index, large-core multimode fiber was chosen in our work.

Appendix D

D.1 Designing optical systems

In designing optical systems, more than ray tracing is sometimes necessary. For example, there is finite beam size even with a perfect lens, and an ideally collimated beam diverges as it propagates. In this chapter, Gaussian beam theory application to fiber-coupled diode laser sensors will be briefly introduced. The fundamental mode laser beam can be well approximated as a Gaussian beam, and there are excellent text books [27, 45, 100].

When the beam diameter is same order of the lens diameter, the coupling of the laser beam tends to sensitive to alignment due to aberration. Therefore, it is desired to use a bigger lens to minimize aberrations. To minimize spherical aberration, an aspheric lens can be adopted, and to minimize chromatic aberration, an achromatic lens can be chosen [100]. In this work, the wavelength of lasers employed ranged over only less than 100 nm, and only spherical aberration was considered. All lenses are aspheric if available. However, if the range is a few hundred nm, then chromatic aberration must be considered, too.

The schematic of the optical system of our interest is shown in Fig.D.1

The optical system has four components- a singlemode fiber, a pitching aspheric lens, a catching aspheric lens, and a multimode fiber. For simplicity, lenses are assumed thin. First, we'll determine the focal length of the pitching lens by minimizing the beam size at the catching lens. Then, by minimizing the focused beam spot size on the multimode fiber, we'll determine the distance of the multimode fiber.

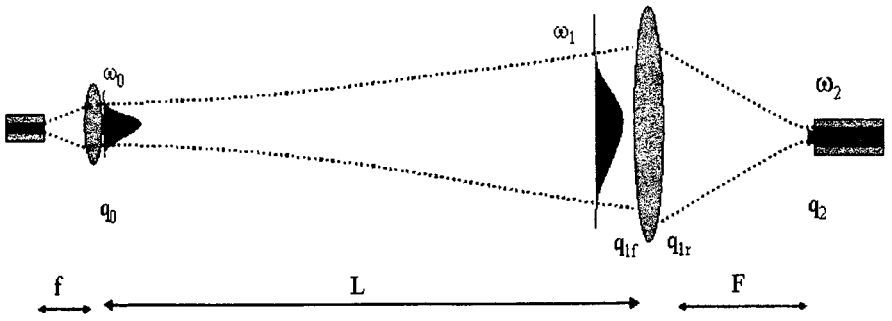

Figure D.1: The schematics of optical system-a singlemode fiber, a pitching lens, a catching lens, and a multimode fiber

D.2 Designing pitching optics

The beam from the pitching lens is usually well collimated by placing the singlemode fiber at the focal length of the lens. The beam diameter,w_0, from the pitching lens can be approximated as

$$w_0 \approx NA_p \times f_p$$

where NA_p is the numerical aperture of the singlemode fiber, and F_s is the focal length of the pitching lens.

Gaussian beam theory states that even if the beam is perfectly collimated, it diverges as it propagates. This divergence becomes significant above the Rayleigh range. At this point, beam waist increases by $\sqrt{2}$ and beam area doubles. The Rayleigh range is defined

$$z_R \equiv \frac{\pi w_0^2}{\lambda}$$

For $z > z_R$, or in far-field, the spot size can be written in terms of Rayleigh range, distance, and waist spot size

$$w(z) = w_0\sqrt{1+(\frac{z}{z_R})^2} = w_0\sqrt{1+(\frac{z\lambda}{\pi {w_0}^2})^2}$$

To get minimum spot size at a distance L,we differentiate w(z) with respect to w_0,

then

$$\frac{\partial w}{\partial w_0} = \frac{1}{2}\frac{1}{\sqrt{{w_0}^2 + \frac{a^2}{{w_0}^2}}}[2w_0 - \frac{2a^2}{{w_0}^3}]$$

where $a = \frac{\lambda L}{\pi}$. By setting $\partial w/\partial w_0 = 0$, the optimized waist spot size is obtained:

$$w_0 = \sqrt{\frac{\lambda L}{\pi}} or f_s = \frac{1}{NA_s}\sqrt{\frac{\lambda L}{\pi}}$$

Corresponding minimum spot size is then,

$$w(L) = \sqrt{2\frac{\lambda L}{\pi}} = \sqrt{2}w_0$$

In other words, if the catching lens is located at the Rayleigh length (z_R) far from the pitching lens, the beam size at the catching lens is minimum.

As an example, we'll design optical system for the IHF test cabin measurements. Lets assume L = 6 m, and the wavelength λ is 780 nm. Then, w_0 = 1.22 mm with a typical NA_p of 0.11 determines the focal length of the pitching lens F_p =11.1 mm and the beam spot size at the catching lens of $w(L)$ = 1.73 mm.

D.3 Optimizing catching optics

The beam size at the waist after focused by the catching lens, w_{02} is formulated as:

$$w_{02} = \sqrt{\frac{\lambda}{\pi}\frac{f^2 z_R}{(L-f)^2 + z_R^2}}$$

With $z_R = L \gg f_c$, w_{02} becomes

$$w(f) \approx \frac{f\lambda}{\pi w_0}$$

The beam diameter can be very small by choosing a small focal length catching lens. However choosing a catching lens, other factors must be considered. First, the numerical aperture of the fiber must be considered to catch all the light incident on

the fiber. Also the clear aperture diameter of the catching lens must be at least π times larger than the diameter of the incoming beam to catch at least 99 % of the intensity. These two requirements can be formulated as:

$$f_c \geq w_1 \pi / tan[arcsin(NA_c)]$$

where f_c is the focal length of the catching lens, w_1 is the beam radius at the lens, and NA_c is the numerical aperture of the catching fiber.

For typical multimode fiber of 400 μm core, NA_c is 0.37. w_1 is the same as $w(L)$ = 1.73 mm. This gives minimum focal length of 13.6 mm. Also the radius of the clear aperture of the catching lens should be larger than $\pi \times w_1$ = 5.43 mm.

D.4 Complex radius curvature parameter, q

Two equations for $w(L)$ and w_{02} can be derived with complex radius curvature parameters.

By definition, q is defined as:

$$\frac{1}{q} = \frac{1}{R} - j\frac{\lambda}{\pi\omega^2(z)}$$

where, R is the radius of curvature of wavefront and w is the beam waist size.

Propagation laws and thin lens law for q are shown below.

$$q_0 = j\frac{\pi\omega_0^2(z)}{\lambda} = jz_R$$

$$q_{1f} = q_0 + L$$

$$\frac{1}{q_{1r}} = -\frac{1}{f_c} + \frac{1}{q_{1f}}$$

$$q_2 = q_{1r} + f_c$$

Two equations for w_{1f} (or $w(L)$), and w_2 (or w_{02}) can be derived with simple algebra.

Bibliography

[1] Smith,R.K., D.A.Wagner, and Dr.James Cunningham (1998). A survey of current and future plasma arc-heated test facilities for aerospace and commercial applications. *AIAA paper 98-0146*

[2] Park,C.S., D.G.Fletcher, and J.M.Donohue (1999).Spatially resolved shock layer emission measurements and analysis in an arc-jet facility. *AIAA paper 99-1046*

[3] Balter-Peterson,A., F.Nichols, B.Mifsud, and W.Love (Jan. 1992). Arcjet testing in NASA Ames Research Center thermophysics facilites. *AIAA paper 92-1071*

[4] Allen,M.G. (1998). Diode laser absorption sensors for gas-dynamic and combustion flows. *Meas.Sci.Technol. 9*, 545-562

[5] Webber,M.E., S.Kim, S.Sanders, D.S.Baer, R.K.Hanson, and Y.Ikeda (2001). In situ combustion measurements of CO_2 by use of a distributed-feedback diode-laser sensor near 2.0 mu m. *Appl.Opt. 40(6).* 821-828

[6] Baer,D.S., H.A.Chang, and R.K.Hanson (1992a). Tunable diode laser diagnostics for atmospheric pressure plasmas. *J.Quant.Spectrosc.Radiat.Transfer. 47*, 455-475

[7] Baer,D.S. and R.K.Hanson (1992b) Fluorescence diagnostics for atmospheric pressure plasmas using tunable diode lasers. *J.Opt.Soc.Am B 9*, 1968-1978

[8] Baer,D.S., H.A.Chang, and R.K.Hanson (1993). Semiconductor laser-based measurements of quench rates in atmospheric pressure plasmas using saturated-fluorescence spectroscopy. *Appl.Opt. 32*, 948-955

[9] Chang,H.A., D.S.Baer, and R.K.Hanson (1993). Semiconductor laser absorption diagnostics of atomic oxygen for atmospheric pressure plasma *Proceedings of the Thirty-First Aerospace Sciences Meeting and Exibit. AIAA-93-0822* (New York:American Institute of Aeronautics and Astronautics.)

[10] Cedolin,R.J. (1997) *Laser-induced fluorescence diagnostics of xenon plasmas* Thermosciences Division Report No.T-105, Ph.D.Dissertation (Stanford University, Stanford, CA)

[11] Sun,H.C., and E.A.Whittaker (1993). Real-time in situ detection of SF_6 in a plasma reactor. *Appl.Phys.Lett. 63* 1035-1037

[12] Sun,H.C., V.Patel, B.Singh, C.K.Ng, and E.A.Whittaker (1995). Sensitive plasma etching end point detection using tunable diode laser absorption spectroscopy. *Appl.Phys.Lett. 04.* 2779-2789

[13] Haverlag,M., E.Stoffels, W.W.Stoffels, G.M.W.Kroesen, and F.J.de Hoog (1996).Measurements of the gas temperatrure in fluorocarbon radio frequency discharges using infrared absorption spectroscopy. *J.Vac.Sci.Technol.A 14.* 380-383

[14] Chou,S., D.S.Baer, R.K.Hanson, W.Z.Collins, and T.Q.Ni (2002). HBr concentration and temperature measurements in a plasma etch reactor using diode laser absorption spectroscopy *J.Vac.Sci.Technol.A 19* 477-484

[15] Kim,S., P.Klimecky, J.B.Jeffries, F.Terry,Jr, and R.K.Hanson (2003). In-situ measurements of HCl during plasma etching of polysilicon using a diode laser absorption sensor. *Meas. Sci. Technol. 14.* 1662-1670

[16] Xu,N., D.R. Pinkle, J.B.Jeffries,B. McMillin, and R.K.Hanson (2004) Near-IR Diode Laser HF Monitor for Dielectric Etch. submitted to *J. Vac. Sci. and Tech.*

[17] Matsui, M., K.Komurasaki, and Y.Arakawa (2002). Laser diagnostics of atomic oxygen in arc-heater plumes. *AIAA paper 02-0793*

[18] Matsui,M., K.Komurasaki, and Y.Arakawa (2002). Characterization of arc-jet type arc-heater plumes. *AIAA paper 02-2242*

[19] Matsui,M., S.Ogawa, K.Komurasaki, and Y.Arakawa (2003) Translational temperature measurement of arc-heater plumes by a laser absorption spectroscopy. *AIAA 2003-0587*

[20] Scott,Carl D. (1993). Survey of measurements of flow properties in arcjets. *Journal of Thermophysics and Heat Transfer 7.* 9-24

[21] Grinstead,J.H., D.M.Driver, and G.A.Raiche (2002) Optical diagnostics development for the Ames arcjet facilities. *AIAA paper 2002-0398*

[22] Grinstead,J.H., D.M.Driver, and G.A.Raiche (2003). Radial profiles of arcjet flow properties measured with laser-induced fluorescence of atomic nitrogen. *AIAA paper 2003-0400*

[23] MacDermott,W.N., D.D.Horn, and C.J.Fisher (1992). Flow contamination and flow quality in arc heaters usd for hypersonic testing. *AIAA paper 92-4028*

[24] Fletcher,D.G. (1999). Arcjet flow properties determined from laser-induced fluorescence of atomic nitrogen. *Appl.Opt. 38* 1850-1858

[25] Park,C.S (1997). Evaluation of real-gas phenomena in high-enthalpy aerothermal test facilities: a review. *Journal of Thermophysics and heat transfer 11.* 330-338

[26] Terrazas-Salinas,I., D.M.Smith, H.Moody, and C.Wanstall (2002). The design and use of calorimeters for characterization of high-enthalpy flows in arc-heated test facilities. *AIAA paper 2002-5236*

[27] Davis,C.C. (1996). *Lasers and Electro-Optics, fundamentals and engineering*, Cambridge: Cambrigde University Press

[28] Vasil'ev, P. (1995) *Ultrafast Diode Lasers, fundamentals and applications*, Norwood, MA: Artech House, Inc.

[29] Bhattacharya,P. (1997). *Semiconductor Optoelectronic Devices.* New Jersey: Prentice-Hall,Inc. 2nd ed.

[30] Sale,T.E. (1975) *Vertical Cavity Surface Emitting Lasers.* Somerst England: Research Study Press LTD.

[31] McDonald,D. and Brian Corbett (1996) Performance characteristics of quasi-single longitudinal-mode Fabry-Perot lasers *IEEE Photonics Technology Letters Vol.8.* 1127-1129

[32] www.koheras.com/press/press mar 2003.pdf

[33] Wang,J., S.T.Sanders, J.B.Jeffries, and R.K.Hanson (2001). Oxygen measurements at high pressures with vertical cavity surface-emitting lasers. *Appl.Phys.B 72* 865-872

[34] Webber,M.E., and J.M.Seitzmann (2000) *Introduction to spectroscopic diagnostics for gases*, Course notes for ME264 Stanford

[35] Sobelman,I.I., L.A.Vainstein, and E.A.Yukov (1981). *Excitation of atoms and broadening of spectral lines*, Springer-Verlag

[36] Griem,H.R. (1974). *Spectral line broadening by plasmas.* New York: Academic Press, Inc.

[37] Demtroder,W. (1998). *Laser spectroscopy, basic concepts and instrumentation*, (Second ed.). New York: Springer-Verlag

[38] Breene,R.G. (1961). *The shift and shape of spectral lines.* Oxford:Permagon Press

[39] Griem,H.R. (1964). *Plasma spectroscopy.* New York: McGraw-Hill Book Company

[40] Griem,H.R. (1997). *Principles of plasma spectroscopy.* Cambridge: Cambridge University Press

[41] Seaton,M.J. (1989). Atomic data for opacity calculations: XII. Line-profile parameters for neutral atoms of He, C, N and O. *J.Phys.B: At.Mol.Opt.Phys.25.* 3603-3697

[42] Shimoda,K. (1976). *High-resolution laser spectroscrpy.* Springer Verlag. 71-49

[43] Whiting,E.E. (1968). An empirical approximation to the Voigt profile. *J.Quant.Spectrosc.Radiat.Transfer.8.* 1379-1384

[44] Humlicek,J. (1982). Optimized computation of the Voigt and complex probability fucntions. *J.Quant.Spectrosc.Radiat.Transfer. Vol.27.* 437-444

[45] Siegman, A.E. (1986) *Lasers.* Sosalito, CA: University Science Books.

[46] Reynolds,W.C. and H.C.Perkins (1977). *Engineering thermodynamics*, Somerst England: McGraw-Hill Science

[47] Boulos,M.I., P.Fauchais, and E.Pfender. (1994) *Thermal Plasmas, fundamentals and applications.* New York: Plenum press

[48] Darwin,H.W. (1972). Thermodynamic properties of the equilibrium and nonequilibrium states of plasmas, in *Reactions under plasma conditions*, M.Venugopalan, ed. (New York: Wiley Interscience)

[49] Balescu,R. (1988) *Transport process in plasmas: v.1. classical theory.* Amsterdam: North-Holland. 236

[50] Galmiche,D. and S.Gauthier (1996). On the Reynolds number in laser experiments. *Jpn. J. Appl. Phys. 35.* 4516-4522

[51] Ouyang,X. and P.L.Varghcese (1989). Line-of-sight absorption measurements of high temperature gases with thermal and concentration boundary layers. *Appl.Opt. 28.* 3979-3984

[52] physics.nist.gov

[53] Liu,Y. and F.Shakib (1990). A comparison of internal energy calculation methods for diatomic molecues *Phys.Fluids A2, 10.* 1884

[54] Liu,Y. and M.Vinokur (1989). Equilibrium gas flow computations. I. Accurate and efficient calculation of equilibrium gas properties. *AIAA-89-1763*

[55] Laux,C. (1993) Optical diagnostics and radiative emission of air plasma *HTGL Report No.T-288.* Ph.D.Dissertation (Stanford University, Stanford, CA)

[56] de Angelis,M., M.Inguscio, L.Julien, F.Marin, A.Sasso, and G.M.Tino (1991). Saturation spectroscopy and velocity-selective optical pumping of oxygen using an (Al,Ga)As diode laser. *Physical Review A 44*, 5811-5819

[57] Jonsson,P. and M.R.Godefroid (2000). Theoretical studies of isotope shifts, hyperfine structures and oscillator strengths in transitions between low-lying levels in O I *Molecular Physics 98.* 1141-1149

[58] Jennerich,R.M. and D.A.Tate (2000). Hyperfine-structure intervals and isotope shifts in the $2p^3 3s^5 S_2 \rightarrow 2p^3 3p^5 P_{J'}$. *Physical Review A 62* 042506-

[59] Radzig,A.A. and B.M.Smirnov (1985). *Reference data on atoms, molecules, and ions.* Berlin:Springer-Verlag

[60] Cangiano,P., M.de Angelis, L.Gianfrani, G.Pesce, and A.Sasso (1994). Hyperfine structure and isotope-shift investigations of atomic nitrogen by saturation spectroscopy *Physical Review A. 50* 1082-1087

[61] Hirsch,J.M., G.H.Zimmerman, D.J.Larson, and N.F.Ramsey (1977). Precision measurements of the hyperfine structure and g_J factor of atomic nitrogen 14. *Physical Review A Vol.16.* 484-487

[62] Wehe,S.D. (2000) Development of a tunable diode laser probe for measurements in hypervelocity flows. *Thermosciences Division Report No.T-127.* Ph.D.Dissertation (Stanford University, Stanford, CA)

[63] Gustafsson,U., J.Alnis, and S.Svanberg (2000). Atomic spectroscopy with violet laser diode. *Am.J.Phys 68*, 660-664

[64] Volz,U. and H.Schmoranzer (1996). Precision lifetime measurments on Alkali atoms and helium by beam-gas-laser spectroscopy *Physica Scripta. T65.* 48-56.

[65] Pollak,C.R. *Fundamentals of optoelectronics* Chicago: McGraw-Hill. 125-174

[66] Snyder,A.W. and J.D.Love (1983). *Optical waveguide theory* New York: Chapman and Hall. Ch.12-15

[67] Emsley,J. (1995). *The Elements, Oxford Chemistry Guides* New York: Oxford University Press

[68] Kelly,R. L. (1987). Atomic and ionic spectrum lines below 2000 angstroms - hydrogen through krypton. *J. Phys. Chem. Ref. Data 16, Suppl.1*

[69] J. Sugar and C. Corliss (1985). Atomic-energy levels of the iron-period elements - potassium through nickel. *J. Phys. Chem. Ref. Data 14 Suppl. 2*

[70] Cool,T.Al. (1965) *Recombination, ionization, and nonequilibrium electrical conductivity in seedede plasma.* Ph.D. Dissertation (California Institute of Technology, Pasadena, CA)

[71] Hanna,S.F., R.B.Jimenez, T.N.Anderson, R.P.Lucht, J.A.Canton, and T.Walther (2002). Diode-Laser-Based Ultraviolet Absorption Sensor for Nitric Oxide. *App. Phys. B 75.* 113-117

[72] Matsubara,K., U.Tanaka, H.Imajo, K.Hayakasa, R.Ohmukai, M.Watanabe, and S.Urabe (1998). An all-solid-state tunable 214.5nm continuous-wave light source by using two-stage frequency doubling of a diode laser. *Appl.Phys.B 67.* 1-4

[73] Corner,L., J.S.Gibb, G.Hancock, A.Hutchinson, V.L.Kasyutich, R.Peverall, and G.A.D.Ritchie (2002). Sum frequency generation at 309nm using a violet and a near-IR DFB diode laser for detection OH *Appl.Phys. B 74* 441-444

[74] Knappe,R., C.K.Laue, and R.Wallenstein (1998). Tunable UV-source based on frequency-doubled red diode laser oscillator-amplifier system. *Electronics Letters 34.* 1233-1234

[75] Knight,D.J.E., F.Minardi, P.De Natale, and P.Laporta (1998). Frequency doubling of a fibre-amplified 1083 nm DBR laser. *Eur.Phys. J.D 3* 211-216

[76] Uhl,R., O.Wolff, J.Franzke, and U.Hass (2000). Laser atomic absorption spectrometry of excited Hg in a discharge applying sum frequency mixing of two diode lasers (preliminary results) *Fresenius J. Anal. Chem. 366.* 156-158

[77] Uchiyama,Y. and M.Tsuchiya (1999). Generation of ultraviolet (335nm) light by intracavity frequency doubling from active mode-locking action of an external-cavity AlGaInP diode laser. *Optics Letters 24.* 1148-1150

[78] Wang,W., M.M.Fejer, R.H.Hammond, M.R.Beasley, C.H.Ahn, M.L.Bortz, and T.Day (1996). Atomic absorption monitor for deposition process control of aluminum at 394nm using frequency-doubled diode laser. *Appl.Phys.Lett. 68 (6).* 5729-5731

[79] Alnis,J., U.Gustafsson, G.Somerfalean, and S.Svanberg (2000). Sum-frequency generation with a blue diode laser for mercury spectroscopy at 254nm. *Appl.Phys.Lett. 76,* 1234-1236

[80] Peterson,K.A. and D.B.Oh (1999). High-sensitivity detection of CH radicals in flames by use of a diode-laser-based near-ultraviolet light source. *Optics Letters 24.* 667-669

[81] Talvitie,H., A.Seppanen, A.Aijala, and E.Ikonen (1998). Continuous-wave light source at 317nm based on frequency doubling of a diode laser. *Appl.Phys.B 66.* 397-400

[82] Oh,D.B. (1995). Diode-laser-based sum-frequency generation of tunable wavelength-modulated UV light for OH radical detection. *Optics Letters 20.* 100-102

[83] White,F.M. (1999) *Fluid mechanics* (Fourth ed.) McGraw-Hill

[84] Vincenti,W.G., and C.H.Kruger Jr (1965). *Introduction to Physical Gas Dynamics*, Malabar Florida: Krieger Publishing Company

[85] Gallawa,R.L., I.C.Goyal, Y.Tu, and ,A.K.Ghatak (1991). Optical Waveguide Modes: An Approximate Solution Using Galerkin's Method with Hermite-Gauss Basis Functions *Journal of Quantum Electronics 27.* 518-522

[86] Turek,I., I.Martincek, and R.Stransky (2000) Interference of modes in optical fibers. *Opt.Eng. 39 (5)* 1304-1309

[87] Yabre,G. (2000) Comprehensive theory of dispersion in graded-index optical fibers. *J.Lightwave Technol. 18.* 166-177

[88] Yabre,G. (2000) Influence of core diameter on the 3-dB bandwidth of graded-index optical fibers. *J.Lightwave Technol. 18.* 668-6776

[89] Mostafavi,M., T.Itoh, and R.Mittra (1975). Excitation of an optical fiber by a Gaussian beam. *Appl.Opt.14.* 2190-2193

[90] Saijonmaa,J., A.B.Sharma, and S.J.Halme (1980). Selective excitation of parabolic-index optical fibers by Gaussian beams. *Appl.Opt. 19.* 2442-2452

[91] Saijonmaa,J. and S.J.Halme (1981) Reduction of modal noise by using reduced spot excitation. *Appl.Opt. 20.* 4302-4306

[92] Imai, M. and E.H.Hara (1974). Excitation of fundamental and low-order modes of optical fiber waveguides by Gaussian beams. 1:Tilted beams. *Appl.Opt. vol.13.* 1893-1899

[93] Imai,M. and E.H.Hara (1975). Excitation of fundamental and low-order modes of optical fiber waveguides by Gaussian beams. 2:Offset beams. *Appl.Opt. 14.* 169-173

[94] Papen,G.C. and G.M.Murphy (1999). Modal noise in multimode fibers uder restricted launch conditions. *J.Lightwave Technol. 17.* 817-822

[95] Kosareva,L.I., O.I.Kotov, S.I.Markov, A.V.Medvedev, and V.M.Nikolaev (2000). Two mechanisms of phase modulation in multimode fiber-optic interferometers. *Tech. Phys. Lett. 26.* 70-74

[96] Liu,Y., B.M.A.Rahman, Y.N.Ning, and K.T.V.Grattan (1995). Accurate mode characterization of graded-index multimode fibers for the application of mode-noise analysis. *Appl.Opt. 34.* 1540-1543

[97] Asawa,C.K. and H.F.Taylor (2003). Propagation of light trapped within a set of lowest-order modes of graded-index multimode fiber undergoing bending, *Appl.Opt. 39,* 2029-2037

[98] Nagano,K. and S. Kawakami (1980). Measurements of mode conversion coefficients in graded-index fiber. *Appl.Opt. 19.* 2426-2434

[99] Horng,J. and D.C.Chang, (1983). Coupling an elliptical Gaussian beam into a multimode step-index fiber. *Appl.Opt. vol.22.* 3887-3891

[100] Hecht,E. (1998). *Optics* (Third ed.) Addison Wesely Longman

The 43rd AIAA Aerospace Sciences Meeting and Exhibit, January 10-13, 2005, Reno, NV **AIAA-2005-0900**

Appendix II

Measurements of Gas Temperature in the Arc-heater of a Large Scale Arcjet Facility using Tunable Diode Laser Absorption

Suhong Kim*, Jay B. Jeffries† and R. K. Hanson‡
High Temperature Gasdynamics Laboratory
Department of Mechanical Engineering
Stanford University, Stanford, CA 94305-3032

George A. Raiche§
Reacting Flow Environments Branch
NASA-Ames Research Center
Moffett Field, CA

Diode laser absorption measurements of atomic nitrogen and oxygen are made in the arc-heater of the NASA Ames IHF (60 MW) arcjet facility. Temperature of the gas in the arc-heater is inferred from the measured mole fraction of electronically excited O and N atoms assuming thermal equilibrium. These results are the first absorption-based temperature measurements inside the arc-heater, where the temperature range is 5000-9000K and the pressure range is 1.5-6 bar. Rapid scanning of the laser wavelength across the absorption feature provides time-resolved measurements of the number density for specific electronic states of the atoms. The agreement of the temperature inferred from redundant measurements on atomic nitrogen and atomic oxygen suggest the equilibrium assumption is valid. The laser is scanned in wavelength across the absorption feature at a rate of 500Hz, and a 100 scan average provides a time-resolution sufficient to examine the variation of temperature with changes in the gas flow and/or electrical power input. These results illustrate the potential of the diode laser sensors for facility performance monitoring.

I. Introduction

New thermal protection system (TPS) materials for NASA missions are developed on the basis of testing in the large-scale, high-enthalpy, arcjet test facilities at NASA-Ames Research Center. Hypersonic speeds of reentry vehicles and systems produce a hot, reactive gas layer between the bow shock and the vehicle surface. A vehicle moving at 10 km/sec in the cold air of the mesosphere (~270K, ~0.1kPa) produces shock temperatures near 7000K with surface heating rates of hundreds of watts per square centimeter. Arcjet facilities provide a long-duration (tens of minutes) source of high-enthalpy hypersonic air flow for ground test of these materials. The NASA-Ames Research Center has three arcjet facilities devoted to testing TPS.[1] Understanding the facility performance is crucial to determine the TPS safety margin needed for reliable flight vehicles.

An arcjet heats a stream of air with a high power electrical discharge, which is accelerated to hypersonic velocities in an adiabatic expansion. The process for relating test conditions to flight environments requires knowledge of the thermodynamic state of the gas prior to expansion. Because of the extreme conditions inside the heater section, options for diagnostics are limited, and optical spectroscopy-based measurements of air-derived species present a diagnostic opportunity. In addition, component materials in the arc-heater and nozzle may erode

* Present address, Lam Research, Fremont, CA, 94538
† Senior Research Engineer, Stanford University, CA 94305-3032, AIAA Associate Fellow
‡ Professor, Stanford University, CA 94305-3032, AIAA Fellow
§ Research Scientist, NASA Ames, Moffett Field, CA, 94035, AIAA Member

and contribute non-air species to the flowfield. One consequence of this erosion is periodic (and costly) component failure, and measuring eroded materials may provide an indication of component health and maintenance requirements.

Here we describe design and demonstration of tunable diode laser absorption sensors (TDLAS) for time-resolved measurements of gas temperature in the arc-heater of these facilities. Diode lasers provide convenient optical sources for absorption measurements [2], and recent development of fiber optics technology makes measurements within the electrically isolated arc-heater feasible. TDLAS of dissociated air species can be used to monitor the high temperatures expected in the arc-heater. In our laboratory at Stanford University, Baer et al. [3,4] used TDLAS to measure temperature and number density of argon in high-temperature rf-plasma discharges. Baer et al. [5] also used a TDLAS near 777.2 nm to monitor oxygen and infer gas temperature in air rf-plasmas. Here we use diode lasers near 777.2 and 844.6 nm to monitor atomic oxygen and near 856.8 and 824.2 nm to monitor atomic nitrogen, in the plenum immediately downstream of the high temperature dc-arc discharge. An additional TDLAS sensor to monitor atomic copper in the flowfield from electrode erosion will be reported elsewhere. The results reported here will demonstrate that TDLAS diagnostics have the potential to provide routine *in situ* monitoring of the gas conditions in the arc-heater.

A schematic of the arcjet flow facility is shown in Fig. 1.[6] A high-current, high-voltage arc heats the input high-pressure gas stream to temperatures in excess of 6000K. The equilibrium dissociation fraction of both oxygen and nitrogen is substantial. This hot, high-enthalpy gas is accelerated via adiabatic expansion and directed over a stationary model, simulating the high speed passage of a space vehicle through an atmosphere.[7] The TDLAS atomic oxygen and nitrogen diagnostics reported here were designed and developed for application in the arc heater.

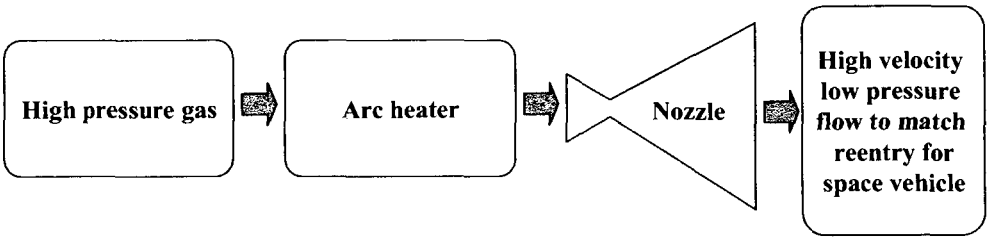

Figure 1. Block diagram of the arcjet wind tunnel facility.

The IHF arc-jet is a large-scale engineering facility. The physical size of the device and the magnitude of the electrical power dissipated in the arc-heater provide significant engineering challenges to the implementation of *in situ* gas sensing. The use of fiber optics to transport the laser light to and from the arc-heater provides the electrical isolation required, and hence the associated optical engineering to design this system is an important part of the overall effort.

II. Gas Temperature Sensor Concept

Emission spectroscopy measurements in the downstream plenum of a lower power (20 MW) arcjet at NASA-Ames indicate equilibrium gas temperatures on the order of 7100 K[8]. At these temperatures, a significant fraction of the oxygen and nitrogen in the air is thermally dissociated; an equilibrium calculation of the air composition is shown in Fig. 2. Although the pressure dependence of the equilibrium composition is significant, the pressure in the arc-heater is known from traditional transducer measurements, and we can account for this effect. Therefore a measurement of atomic nitrogen and/or oxygen can be used to infer the degree of dissociation and thus the equilibrium temperature. The results in Fig. 2 illustrate that the atomic nitrogen mole fraction is more sensitive to temperature than atomic oxygen for the range of temperature expected.

The resonant absorption from the ground states of atomic oxygen and nitrogen occur in the vacuum ultraviolet region of the spectrum as illustrated in Fig. 3, and absorption measurements of these atoms in their ground states is not feasible. Absorption sensors at these short wavelengths are subject to many problems and challenges, e.g. there are many interference absorptions in the ultraviolet, laser sources are not readily available, specialty materials are required for optical windows, and optical fiber technology is not developed. However, there are excited electronic states of atomic N and O which absorb light in the near-infrared wavelengths 777.2 and 844.6 nm (856.8, and 824.2 nm for atomic nitrogen), where diode lasers are available and the fiber optics technology is well developed. Previous work in our laboratory has demonstrated the use of diode laser absorption using these transitions to detect atomic oxygen in rf discharges.[5] Although measurements were performed on all four transitions, we found the

777.2 nm transition in the quintet manifold of oxygen and the 856.8 nm transition in the quartet manifold of nitrogen to have significantly superior signal to noise. This performance advantage is primarily due to the output power and wavelength tunability of available laser devices.

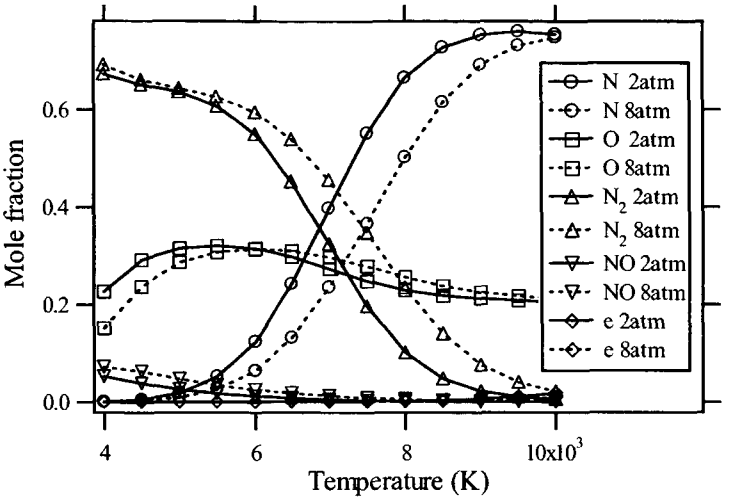

Figure 2. Equilibrium gas composition for air plasma at 2 and 8 atmosphere pressures.

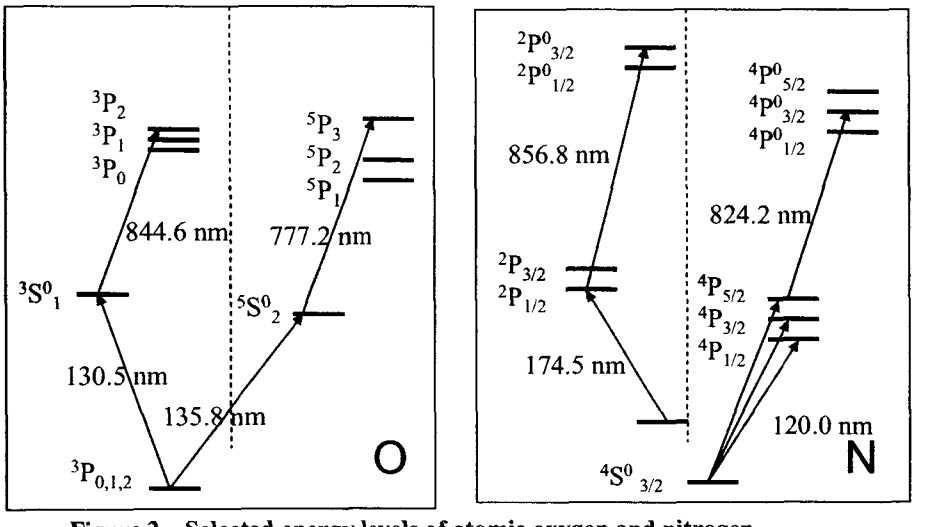

Figure 3. Selected energy levels of atomic oxygen and nitrogen.

These excited states of oxygen and nitrogen have several eV of internal energy and thus, even at the high temperature of the plasma, less than 1ppm of the atomic nitrogen and oxygen are electronically excited. However, the absorption from these atomic transitions is strong and there is significant attenuation at the center of an absorption feature for the laser beam transmitted across the 11.4 cm diameter of the arc-heater. This large internal energy of the lower state of the optical absorption provides a strong variation in excited state population with gas temperature as illustrated in Fig. 4. The fraction of the atom population in the excited state varies more than an order of magnitude per 1000K. Thus, a measurement of the population in one of these excited states of oxygen or nitrogen provides a sensitive monitor of the gas temperature for the temperature range expected in the arc-heater.

III. Gas Temperature Sensor Design

We measure the absorption of the laser light across the flow path by scanning the wavelength of the laser rapidly and repeatedly through the absorption feature and comparing the incident and transmitted laser power. Direct

Appendix II

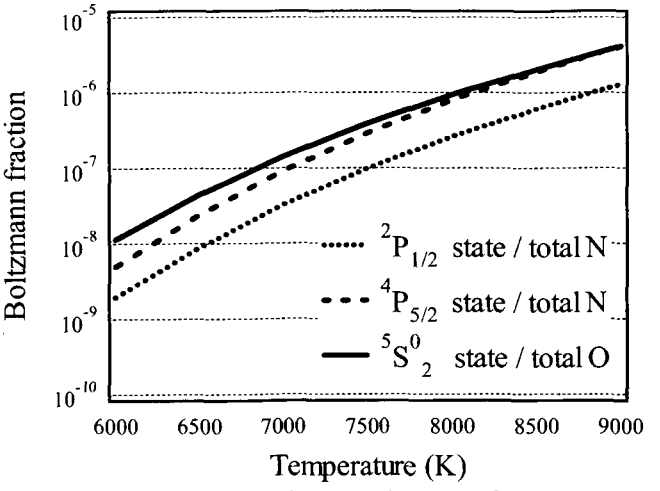

Figure 4. Thermal population of electronically excited N and O versus gas temperature.

absorption spectroscopy for a spectrally narrow tunable diode laser is governed by the Beer-Lambert law, which relates the transmitted intensity I_t through a uniform gas medium of length L [cm] to the incident intensity I_0:

$$\left(\frac{I_t}{I_0}\right)_\nu = \exp(-k_\nu L), \tag{1}$$

where k_ν [cm^{-1}] is the spectral absorption coefficient. For an isolated transition k_ν is written

$$k_\nu = h\nu n_l (B_{lu}/c)(1-\exp(h\nu/kT_{ex}))\phi_\nu, \tag{2}$$

where n_l is the lower state number density, B_{lu} is the Einstein coefficient for absorption between the lower level l and the upper level u, T_{ex} is the excitation temperature which describes the ratio of populations in the laser-coupled excited states l and u, and ϕ_ν the lineshape function. The frequency integral of the lineshape function is normalized to unity. The lower state number density, n_l may be related to the gas temperature, T, for a system in thermal equilibrium with the ground state number density via

$$n_l / n = (g_l / Z)\exp(-E_l / kT) \tag{4}$$

where g_l and E_l are the lower state degeneracy and excitation energy; Z and n is the atomic partition function and total species number density.

The hostile environment of this facility has necessitated significant optical engineering. For safety reasons, the entire arc-heater assembly is located in an electrically isolated room, and the lasers, control electronics, optical detectors, and control computer are isolated from the arc-heater via 30 m of optical fiber. Diode lasers at the appropriate wavelength are selected, protected from optical feed back, and coupled into a single mode fiber to provide electrical isolation of the laser electronics from the arc-heater. The transmission of the laser light across the arc-heater plasma is illustrated in Fig. 5. The arc-heater is a stack of annular copper ring segments, each water cooled and electrically isolated from its neighbors, and electrically floated to prevent arc attachment. Optical access is provided via a specially-designed arc-heater segment immediately downstream of the cathode and upstream of the nozzle; small holes are bored along a radial line of sight of the optical segment, and quartz windows mounted in the telescope assembly allow optical access while preserving pressure and cooling seals. A telescope assembly mounted on the copper ring segment projects the laser light from a single mode fiber into a beam directed across the plasma flow (11.4 cm), and a second telescope assembly collects the light and couples it into a large-aperture multimode fiber for transport to the detection electronics.

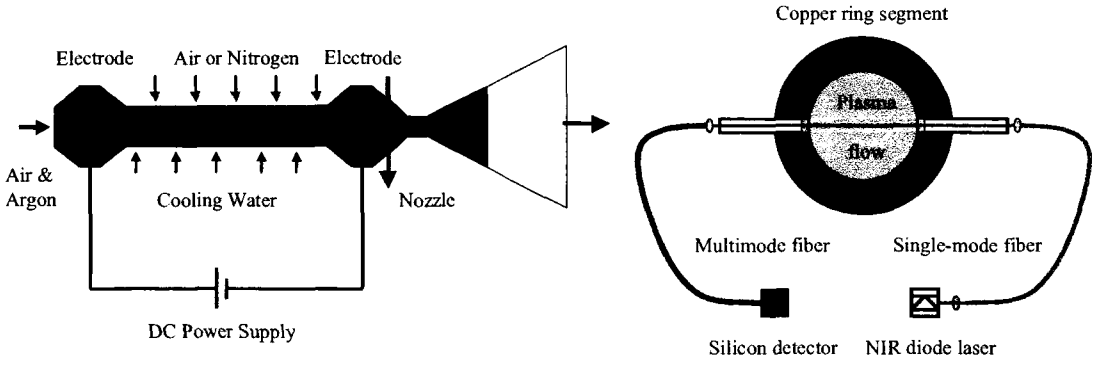

Figure 5. Schematic of the arc-heater with a detail illustrating the installation of the diode laser sensor.

IV. Gas Temperature Measurements

Figures 6 and 7 illustrate measurements of TDLAS of atomic oxygen in the $^5S^0_2$ state near 777.2 nm and atomic nitrogen in the $^4P_{5/2}$ state near 856.8. The Doppler width of the transition would provide a direct measurement of the translational temperature; however, the complicated Zeeman splitting and collisional broadening of the transitions make extraction of the Doppler width difficult. The absorption measurements are perturbed by a significant, non-uniform magnetic field in the electrode assembly where the TDLAS sensor is located. This field separates the degenerate sub-levels of the atom and complicates fitting of the pressure broadening contribution to the lineshape. Fortunately, these transitions are isolated, and the lasers can be rapidly tuned over a sufficient wavelength range to extract a zero absorption baseline and enable accurate integrated absorption measurements.

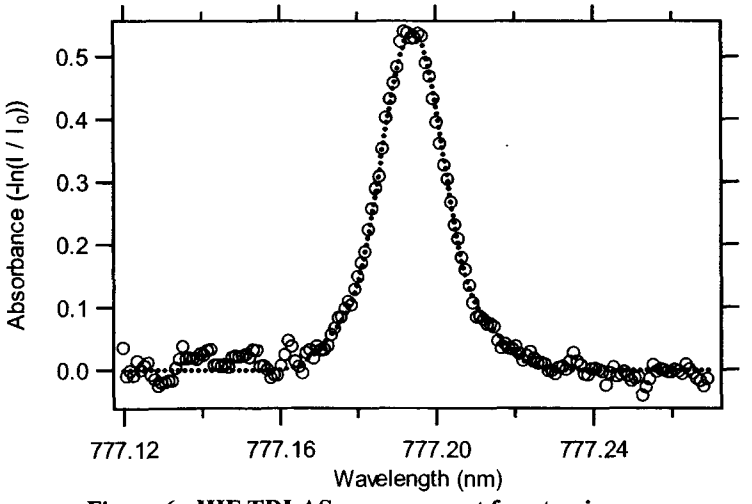

Figure 6. IHF TDLAS measurement for atomic oxygen.

The number density of excited atoms is determined from the integrated absorption. Combined with simultaneous measurement of gas pressure in the arc-heater, we can infer a "population temperature" assuming the gas is in thermal equilibrium. The data shown in Fig. 6 gives an excited oxygen atom concentration of $3.6(10)^{10}$ cm^{-3}, and the measured pressure is 196 kPa. Using a gas composition from the measured flow rates of air and argon and an equilibrium assumption, the fraction of the total atomic oxygen in the metastable quintet state is $1.87(10)^{-7}$, which implies a population temperature of 7120±200K. This is in good agreement with the equilibrium temperature of 6750 K estimated by energy balance measurements of facility input power, cooling heat extraction, and an estimate for the heat capacity high temperature plasma at the arc-heater conditions. Similarly the data in Fig. 7 yield an excited nitrogen concentration of $1.3(10)^{10}$ cm^{-3}, and a population temperature of 6850±160K. The agreement

between the atomic nitrogen and atomic oxygen population temperatures is good evidence of the validity of the equilibrium assumption.

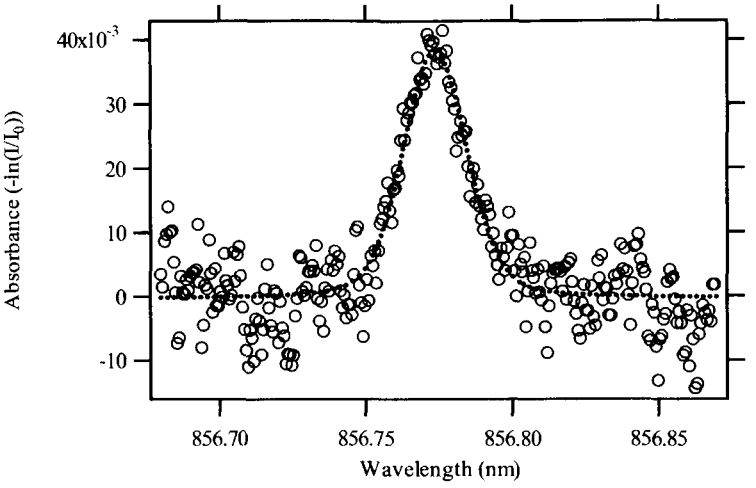

Figure 7. IHF TDLAS measurement for atomic nitrogen.

The TDLAS measurements are made at 20Hz and the individual scans are averaged to provide an output temperature measurement with one second resolution. Fig. 8 shows a time history for simultaneous measurements of population temperature using both N and O atom measurements. The first 200 seconds of the run comprise the turn-on sequence for the arc-heater when the discharge is initiated in argon, a small amount of air is added, and the mass flow rate of the air is increased to develop a stable discharge. Next (200-400 s) the voltage, current, mass flow, and pressure are increased to their target values of 44.4 MJ per kg of mass flow (power 32.4 MW; flow rate 0.73 kg/s). At 420 seconds both the mass flow and electric power input were reduced to a second operating condition (6.49 MW; 0.146 kg/s) that preserved the power-mass flow ratio. The measurements in Fig. 8 show that there is roughly a 10% increase in the gas temperature for the second condition, implying slightly better heater efficiency at reduced flow rates. This may be a consequence of changing heat transfer (loss) to the arc heater wall as a function of flow rate; higher flow rates may thin the boundary layer at the arc heater wall, allowing additional heat transfer to the cold wall that will cool the air plasma.

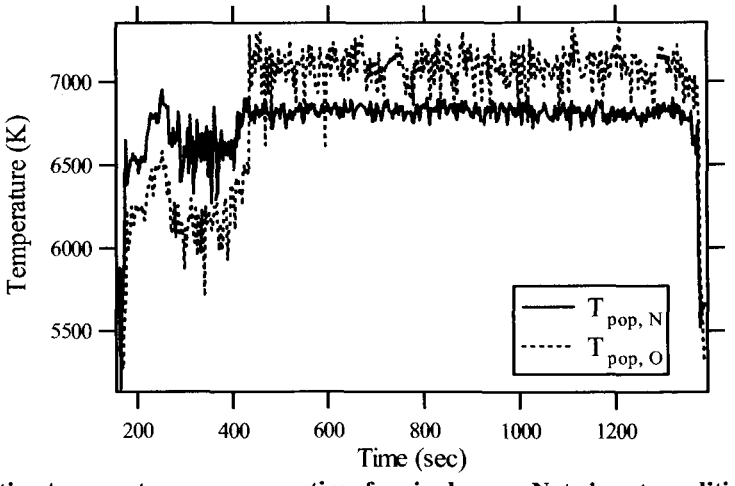

Figure 8. Population temperature versus run time for single run. Note input conditions change at 420 s.

The oscillator strength of the quintet S atomic oxygen transition near 777.2 nm is approximately four times larger than that for the quartet P atomic nitrogen transition near 856.8 nm. This difference in transition strength,

combined with differences in oxygen and nitrogen Boltzmann populations at these temperatures, result in a larger peak absorbance for atomic oxygen. However, nitrogen dissociation is more sensitive to temperature at these conditions (see Figure 4), therefore a small variation in the atomic number density translates to a larger temperature variation. Thus, even though the atomic nitrogen absorption measurements are small and have a lower signal to noise, the atomic nitrogen population temperature is has better precision.

A set of 19 arcjet runs was made at four different heater conditions with a heater pressure between 175 and 415 kPa and the input arc power ranged from 5.17 to 15.6MW. The conditions were chosen for constant input energy of 43 MJ/kg of air mass flow. Thus, a constant arc-heater temperature would be expected, and the measured population temperature for atomic oxygen is constant within our estimated uncertainties. It would therefore appear that the gas temperature remains constant for a large range of facility flow rates and power settings, as long as the energy content per unit mass—the enthalpy—remains constant. Alternatively, a substantial change in temperature for constant input enthalpy may indicate an efficiency change in heat transfer requiring maintenance attention. This illustrates the potential of this TDLAS sensor for routine monitoring of the arc-heater performance.

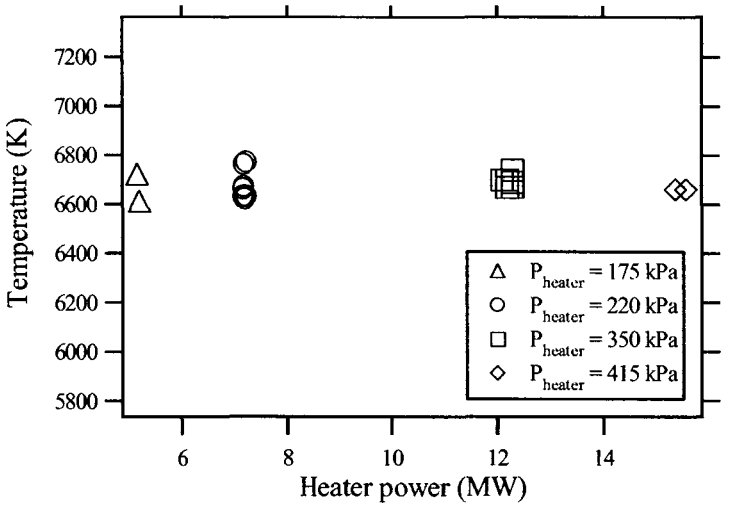

Figure 9. Arc-heater temperature for runs with constant input energy per unit mass flow of 43MJ/kg.

V. Conclusions

These absorption-based measurements of gas temperature inside the arc-heater plasma of the IHF flow facility at NASA-Ames were made using TDLAS to monitor the concentration of electronic excited states of atomic O and N. The redundant measurements confirm the validity of the equilibrium assumption for the pre-expanded gas. Differences in gas temperature for changes in mass flow with constant arc-heater power per unit flow indicate a slightly higher thermal transport to the walls consistent with the thinner boundary layer for higher flow rates. The measurements reported here illustrate the feasibility of the TDLAS sensor techniques for routine monitoring of detailed arc jet performance parameters.

Acknowledgments

This research was supported via a NASA-Ames University Research Consortium Grant. We thank David Driver, Joe Olejniczak, Jay Grinstead, Robert Finney, and Vince Meglio of NASA-Ames for advice, facility, and design assistance.

References

1. R.K. Smith, D.A. Wagner, and J. Cunningham, "A Survey of Current and Future Plasma Arc-Heated for Aerospace and Commercial Applications," American Institute of Aeronautics and Astronautics, AIAA-1998-0146, (1998).
2. M.G. Allen, "Diode Laser Absorption Sensors for Gas-Dynamic and Combustion Flows," Measurement Science and Technology, 9, 545-562 (1998).

3. D.S. Baer, H.A. Chung, and R.K. Hanson, "Tunable Diode Laser Diagnostics for Atmospheric Pressure Plasmas," J. Quantitative Spectros. Radiat. Trans. 47, 455-475 (1992).
4. D.S Baer and R.K. Hanson, "Fluorescence Diagnostics for Atmospheric-Pressure Plasmas using Tunable Diode Lasers," J. Opt. Soc. Am. B, 9, 1968-1978 (1992).
5. D.S. Baer, H.A. Chung, and R.K. Hanson, "Semiconductor Laser Absorption Diagnostics of Atomic Oxygen in an Atmospheric-Pressure Plasma," J. Quant. Spectrosc. Radiat. Trans., 50, 621-633 (1993).
6. A. Balter-Peterson, F. Nichols, B. Mifsud, and W. Love, "Arcjet Testing in the NASA Ames Research Center Thermophysics Facilities," American Institute of Aeronautics and Astronautics, AIAA-1992-1071, (1992).
7. C.S. Park, D.G. Fletcher, and J.M. Donahue, "Spatially Resolved Shock Layer Emission Measurements and Analysis in an Arcjet Facility," American Institute of Aeronautics and Astronautics, AIAA-1999-1046, (1999).
8. J.M. Donohue, D.G. Fletcher, and C.S. Park, "Emission Spectral Measurements in the Plenum of an Arcjet Wind Tunnel," American Institute of Aeronautics and Astronautics, AIAA-1998-2946 (1998).